PRODUCTION OF THE $\psi(3100)$ IN 400 GEV PROTON - IRON INTERACTIONS

Thesis by

Eric Jonathan Siskind

In Partial Fulfillment of the Requirements

for the Degree of

Doctor of Philosophy

California Institute of Technology

Pasadena, California

1979

(Submitted March 27, 1979)

"Those whom the gods wish to destroy,

They first make mad."

Aeschylus

"Those whom the gods wish to destroy,

They first give particle physics Ph.D.'s"

Anonymous

"On the other hand, perhaps not."

E. Siskind

Quod Erat Demonstrandum!

ACKNOWLEDGEMENTS

Financial support for this thesis experiment was provided at Caltech and Fermilab by the United States Department of Energy (earlier the Energy Research and Development Adminstration) and at Stanford by the National Science Foundation. Personal financial support of my graduate student tenure was provided by the DoE, by an NSF graduate fellowship, and by Millikan and Feynman fellowships from Caltech. Additional support during my developing physics career included four years and two summers of special programs from the NSF, plus scholarships from the New York State Board of Regents and the van Raalte Corporation (through the National Merit Scholarship Corporation).

Technical support for the experiment was provided by the shops of both Caltech and Stanford/SLAC group G, as well as practically every section of Fermilab. In this latter group, because of the high level of cooperation shown to me personally, I would especially like to thank members of the hardware groups of both the Research Services Division and the Computer Department, as well as the Operations Group of the Neutrino Department.

The overall direction of my research was set by my adviser, Barry Barish, who deserves special thanks for his relaxed style of doing physics, his ability to perceive the identities of the crucial points in both the construction and analysis of this experiment, and his tolerance for the winner of a special competition for mulishness and pigheadedness. Both he and the other members of the experimental collaboration: Fritz Bartlett, Arie Bodek, Wyatt Brown, and Mike Shaevitz of Caltech, and Alain Diamant-Berger, Pat Dishaw, Martin Faessler, John

Liu, Frank Merritt, and Stan Wojcicki of Stanford, have my appreciation for their ability to dispense both encouragement and constructive criticism in properly timed and sized dosages.

The progression of my training as a physicist has been directed and encouraged along the way by a number of people, among them B. Jenkins, L. Motz, L. Love, A. Aimette, D. Cassel, D. H. White, D. Hartill, and F. Sciulli.

The study of physics being an occupation of human beings, the task of keeping me out of the laboratory, off the streets, and in the bars (only figuratively, of course) has fallen to numerous friends, among them: R. Boynton, M. Delwiche, and L. Lavery at Cornell, J. Bobbitt, D. Curtis, T. Droege, A. Dzierba, H. E. Fisk, R. Gustafson, T. Lahey, D. Ritchie, L. Stutte, and A. Tollestrup at Fermilab, and A. Barnes, M. Bartelt, C. and J. Bromberg, C. Carlson, C. and R. Gomez, D. and L. Koop, W. Kropac, E. and G. Mills, F. Nagy, E. Newman, J. Rohlf, L. Sartain, J. Siegel, S. Stampke, C. van Ingen, and K. Yung at Caltech.

All of these people have proven at times to be interesting, provocative, and diverting, but there has remained from the very beginning only one friend who has always been with me, dealing neither with the physicist nor the shell that housed him, but rather with the whole man, enduring numerous delays and disappointments, often bitter, and teaching me that the intelligent pursuit of and commitment to intelligent excellence in all things, but most especially friendship, is both the most demanding and most rewarding of human pursuits. For these reasons this thesis, representing nothing more nor less than my time, is dedicated to her. Christmas Eve, 1978.

For Luca

ABSTRACT

The production and subsequent dimuon decay of the vector meson resonance $\psi(3100)$ have been studied in the collisions of a 400 GeV proton beam incident on an iron target-calorimeter. The apparatus featured a large acceptance iron muon spectrometer, and observed the ψ over a range of transverse momentum (P_t) from 0 to 4 GeV and of Feynman x (x_F) from -.25 to .40.

The best fits to the data gave $E \frac{d\sigma}{dx_F} \propto (1 - |x_F|)^{2.96 \pm .27}$ (χ^2 = 12.9 for 11 degrees of freedom), and $\frac{1}{P_t} \frac{d\sigma}{dP_t} \propto e^{-2.23 \pm .05 P_t}$ (χ^2 = 8.6 for 12 degrees of freedom) for $P_t > 1.2$ GeV. The angular distribution of ψ decays, as measured in the s channel helicity frame, was consistent with a flat spectrum.

The observed values of dimuon branching ratio (B) times zero rapidity (y) and total cross sections ($B \left.\frac{d\sigma}{dy}\right|_{y=0}$ and $B\sigma$) were 14.0 ± 2.9 and 22.9 ± 4.7 nanobarns per nucleon respectively.

The observed cross sections and differential distributions are presented in the light of existing world data on hadronic ψ production.

TABLE OF CONTENTS

Chapter I: Introduction

A. Charm and the $\psi(3100)$ 1

B. Production and Decay Mechanisms 3

C. Outline of Thesis 5

References 7

Chapter II: Beam and Apparatus

A. Overview 9

B. The N-5 Beam Line 11

C. The PWC System 14

D. The Beam Counters 17

E. The Calorimeters 18

F. The Upstream Spark Chambers 20

G. The Toroidal Muon Spectrometer 23

H. The Toroid Detectors 25

I. The Trigger Counters and Trigger Logic 28

J. The Data Collection System 30

References 33

Chapter III: Data Reduction

A. Overview 35

B. Preliminary Raw Data Abstraction 37

C. Track Reconstruction 38

D. Momentum Fitting 39

Chapter IV: Triggering, Trigger Acceptance, Smearing, and Reconstruction Efficiency

A. Overview 41

B. The P_t Trigger 42

C. The Monte Carlo Program 44

D. Trigger Efficiency 46

E. Transverse Momentum Distribution of ψ Decay Muons 47

F. Monte Carlo Characteristics and Efficiency Definition 50

G. Efficiency Results 52

Reference 64

Chapter V: Data, Backgrounds, and Normalization

A. Overview....65

B. Non ψ Background Subtraction....67

C. Secondary Production Background....68

D. Normalization....71

E. X_F Distribution....72

F. P_t Distribution....78

G. Decay Angular Distribution....81

References....85

Chapter VI: Cross Sections and Summary

A. Cross Section Results....86

B. Cross Sections From Other Experiments....87

C. P_t Distributions....89

D. X_F Distributions....89

E. Angular Distributions....92

F. Atomic Weight Dependence....93

G. Associated Production....94

References....96

Appendix A: Calorimeter Instrumentation

1. Upstream Calorimeter....98

2. Downstream Calorimeter....100

3. Calorimetry Monitoring....101

References....105

Appendix B: Spark Chamber Processing and Track Reconstruction Routines

1. CD Chamber Spark Preprocessing....106

2. CIT Chamber Spark Preprocessing....107

3. Straight Line Segment Finding....108

4. Matching of X and Y Projections....109

5. Matching of First and Second Upstream Modules....110

6. Inefficiency Compensations....111

7. Straight Line Search Downstream of Magnet....113

8. Toroid Track Finding....113

9. Momentum Fitting....115

CHAPTER I

INTRODUCTION

A. Charm and the $\psi(3100)$

The discovery in 1974 of the $\psi(3100)$ resonance in hadron interactions[1] and e^+e^- collisions[2] marked the beginning of a period of unusual excitement in elementary particle physics. On the one hand, the exceedingly small width of the resonance argued convincingly for a suppression of strong decay modes, and thus for the probable presence of some new quantum number conserved by the strong but not by the weak interactions. On the other hand, although the ψ was produced by an electromagnetic process at SPEAR, the ratio of ψ events to continuum dimuons (believed to be of electromagnetic origin) in a subsequent experiment on neutron induced ψ production[3] showed that the ψ could be produced by the strong interactions.

Theoretical speculation had for some time centered on the possible existence of a fourth quark, called the c or charmed quark. In the conventional quark model, the three quarks u, d, and s participate in the weak interactions as the u and a linear combination of d and s, called the Cabibbo down quark ($d_c = d\cos\theta_c + s\sin\theta_c$). The weak charged current coupling the u to d_c contains a portion proportional to $\cos\theta_c$ coupling u to d, and responsible for nuclear beta decay, charged pion decay, and the major portion of charged current neutrino-nucleon scattering. The other part of the u-d_c current, proportional to $\sin\theta_c$, couples u and s quarks, and is responsible for beta decay of the Λ^o, charged kaon decay, and another portion of charged current neutrino-nucleon scattering.

The weak neutral currents, resulting from coupling of u to u and d_c to d_c, then linked u to u, d to d (with magnitude $\cos^2\theta_c$), s to s (with magnitude $\sin^2\theta_c$), and d to s (with magnitude $\cos\theta_c\sin\theta_c$). The first two of these were easily observable in neutral current neutrino-nucleon scattering. However, the last process, involving a strangeness changing weak neutral current, although it would give rise to such experimentally obvious decays as $K^0 \to \mu^+\mu^-$, was not observed.

In a four quark model, the c quark is coupled to the orthogonal d-s combination the Cabibbo strange quark ($s_c = s\cos\theta_c - d\sin\theta_c$). The neutral current coupling of s_c to s_c contains a strangeness changing component which exactly cancels the similar component in the d_c to d_c current. The c-s_c charged current analagous to the u-d_c current contains a portion coupling d to c, and provides a means of producing c quarks in neutrino-nucleon interactions, with the weak decay of the c quark producing the second muon in neutrino induced dimuon events. Finally, in the quark model, the ratio (R) of the rates for $e^+e^- \to$ hadrons to $e^+e^- \to \mu^+\mu^-$ is just the sum of the squares of the charges of all quarks (including all colors of quarks) which can be produced at the energy ($\sqrt{s}$) of the e^+e^- pair. The existence of an observed step in R at $\sqrt{s}$ near 3 or 4 GeV could be explained by a c quark of mass between 1.5 and 2 GeV.

Within this theoretical framework[4], the ψ found an immediate home [5] as the lowest lying spin one bound state of a charmed quark and a charmed antiquark. The discovery a week later of the excited state $\psi'(3685)$[6] and the subsequent appearance of even charge conjugation χ states[7] added credence to this interpretation. The final piece of supporting evidence came with the discovery of the D(1865) mesons[8],

which decay in the modes expected of a meson containing a single charmed quark and one normal quark, the $\psi''(3770)$ resonance of a $D\bar{D}$ pair[9], and the charmed vector mesons D*(2010)[10].

B. Production and Decay Mechanisms

In explaining the narrow width of the ψ, theorists appealed to an extension of the OZI rule [11], a postulate originally advanced to explain the large fraction of decays of the ϕ in which strange particles are present. Stated simply, the OZI rule proposes that decay processes in which the constituent quark and antiquark in a meson annihilate into an intermediate state containing no quarks are suppressed in the strong interactions. Thus the ϕ, containing one s and one $\bar{s}$ quark, decays primarily into $K\bar{K}$ while decays into states such as $\pi\pi$ are suppressed, although the phase space for such reactions is much larger than that for the $K\bar{K}$ decay. In the case of the ψ, the $D\bar{D}$ decay analagous to the $K\bar{K}$ decay of the ϕ is below kinematic threshold, and so only OZI forbidden strong decays can contribute. Thus the lifetime of the ψ is exceedingly long.

The problem for thecry is then one of constructing a model for copious ψ production in the strong interactions which does not simultaneously destroy the small width of the ψ. In particular, any process which produces the $c\bar{c}$ pair of quarks forming the ψ in a disconnected topology essentially violates the OZI rule (here applied in reverse). Production in a connected topology (e.g. fusion of a c quark from the ocean of the beam particle with a $\bar{c}$ quark from the target ocean) generally implies the existence in the final state of an additional c and $\bar{c}$

quark, i.e. a pair of charmed particles. Experimental searches for such associated production[12] have yielded negative results at the level of a few percent.

A theory which currently seems quite plausible is the gluon cascade model[13] in which a gluon from the beam particle and a gluon from the target fuse to form a $c\bar{c}$ state of even charge conjugation. This χ state then decays into a ψ and a photon. Such a process has the advantage that it is not reversible--the χ and not the ψ can decay into gluons. Recent experimental evidence[14] indicates that 70 ± 28 percent of the ψ's produced in π^--nucleon interactions at 217 GeV are products of the radiative decay of a χ state of mass near 3.5 GeV. A similar experiment at the CERN ISR[15] at an average $\sqrt{s}$ of 55 GeV indicates that χ decays account for 43 ± 21 percent of ψ production.

We thus find ourselves in a situation in which probably no one mechanism will account for all hadronic ψ production, and no one experiment can hope to provide enough input to the theory. In the gluon cascade model, both the cross sections and differential distributions for ψ production are sensitive to the gluon distributions within the nucleon. Other models, involving for instance the collision of a hard gluon from the beam particle with a $c\bar{c}$ pair in the ocean of the target, are sensitive to both gluon and quark distributions, while still other processes, involving quark-quark collisions, probe only quark distributions. Whatever the true mechanism (or mechanisms), construction and testing of models of hadronic ψ production are greatly aided by measurements of production cross sections and differential distributions over the widest possible range of kinematic variables.

C. Outline of Thesis

This thesis describes an experiment to measure ψ production and subsequent dimuon decay in 400 GeV proton interactions on an iron target-calorimeter. The experiment featured a large acceptance muon spectrometer, and was capable of observing ψ's of transverse momentum (P_t) from 0 to 4 GeV, and from Feynman x (x_F) of -.25 to .40.

Previous experiments at 400 GeV[16], the highest energy currently available for fixed target physics, have contained double arm spectrometer systems at 90 degrees in the center of mass, and thus have had their acceptance limited to a narrow region around x_F of zero. The largest acceptance apparatus has been that of the Chicago-Princeton group[17], which has only taken data up to 225 GeV. The need to identify muons by range in dense material, coupled with the low incident beam momentum, has restricted this experiment to observing only those ψ's produced in the forward hemisphere of the center of mass. Finally, higher energy experiments at the CERN ISR[18] have typically been limited by luminosity, and have been unable to observe large numbers of ψ events.

The general descriptions of beam and apparatus used in this experiment are contained in chapter II, with technical details of some hardware used in the experiment but not in the current analysis relegated to appendix A. Chapter III contains a brief description of the data reduction employed in this analysis, with a more detailed description of track finding requirements located in appendix B. Details of triggering, trigger acceptance, and overall experimental differential efficiency are described in chapter IV, while background corrections, normalization, and differential distributions are located in chapter V. Finally, cross

section results are presented in chapter VI, which also attempts to place results in the perspective of existing world data on hadronic ψ production.

REFERENCES

1-1 J. J. Aubert et al., Phys. Rev. Lett. 33, 1404, (1974).

1-2 J. E. Augustin et al., Phys. Rev. Lett. 33, 1406, (1974); C. Bacci et al., Phys. Rev. Lett. 33, 1408, (1974).

1-3 B. Knapp et al., Phys. Rev. Lett. 34, 1044, (1975).

1-4 M. K. Gaillard, B. W. Lee, and J. L. Rosner, Rev. Mod. Phys. 47, 277, (1975).

1-5 T. W. Appelquist and H. D. Politzer, Phys. Rev. Lett. 34, 43, (1975); A. De Rújula and S. L. Glashow, Phys. Rev. Lett. 34, 46, (1975).

1-6 G. S. Abrams et al., Phys. Rev. Lett. 33, 1453, (1974).

1-7 W. Braunschweig et al., Phys. Lett. 57B, 407, (1975); G. J. Feldman et al., Phys. Rev. Lett. 35, 821, (1975); W. Tanenbaum et al., Phys. Rev. Lett. 35, 1323, (1975); J. S. Whitaker et al., Phys. Rev. Lett. 37, 1596, (1976); C. J. Biddick et al., Phys. Rev. Lett. 38, 1324, (1977).

1-8 G. Goldhaber et al., Phys. Rev. Lett. 37, 255, (1976); I. Peruzzi et al., Phys. Rev. Lett. 37, 569, (1976).

1-9 P. A. Rapidis et al., Phys. Rev. Lett. 39, 526, (1977).

1-10 G. J. Feldman et al., Phys. Rev. Lett. 38, 1313, (1977).

1-11 S. Okubo, Phys. Lett. 5, 165, (1963); G. Zweig, unpublished report; J. Iuzuka, Prog. Theor. Phys. Suppl. 37-38, 21, (1966).

1-12 M. Binkley et al., Phys. Rev. Lett. 37, 578, (1976); J. G. Branson et al., Phys. Rev. Lett. 38, 580, (1977).

1-13 M. B. Einhorn and S. D. Ellis, Phys. Rev. D12, 2007, (1975); M. Glück, J. F. Owens, and E. Reya, Phys. Rev. D17, 2324, (1978);

C. E. Carlson and R. Suaya, Phys. Rev. D14, 3115, (1976), Phys. Rev. D18, 760, (1978), and preprint SLAC-PUB-2212.

1-14 T. B. W. Kirk et al., preprint FERMILAB-Pub-78/76-EXP, submitted to Phys. Rev. Lett.

1-15 J. H. Cobb et al., Phys. Lett. 72B, 497, (1978).

1-16 H. D. Snyder et al., Phys. Rev. Lett. 36, 1415, (1976); B. C. Brown et al., preprint FERMILAB-77/54-EXP.

1-17 K. J. Anderson et al., Phys. Rev. Lett. 37, 799, (1976); J. G. Branson et al., Phys. Rev. Lett. 38, 1331, (1977).

1-18 F. W. Büsser et al., Phys. Lett. 56B, 482, (1975); J. H. Cobb et al., Phys. Lett. 68B, 101, (1977), and reference 1-15.

CHAPTER II

BEAM AND APPARATUS

A. Overview

The experiment was performed in Neutrino Area Laboratory E of the Fermi National Accelerator Laboratory in Batavia, Illinois. The beam utilized was the N-5 hadron beam line[1] originally installed to provide high quality low intensity hadron beams for the 15' bubble chamber. An additional 16 milliradian horizontal dipole magnet and 4 x-y PWC's were added to the beam line for this experiment in order to provide event by event incident particle momentum and position information.

The apparatus, pictured in figure 2-1, consisted of beam defining detectors, a steel/scintillator sandwich target-calorimeter, a module of spark chambers, a second calorimeter/muon identifier, a second spark chamber module, and the Lab E Toroidal Muon Spectrometer[2]. This last piece of apparatus, consisting of three 11.5' diameter steel toroids, is mounted on rollers and can be moved transversely to the beam axis in order to change triggering conditions or for use in counter neutrino experiments conducted by the Caltech group in Lab E. For the part of the running utilized in this thesis, the spectrometer was centered on the beam axis. Fast trigger counters were located throughout the apparatus in Lab E. In addition, the counters most downstream were located in a separate "doghouse" approximately 7 meters downstream of the lab.

The MULTI data collection and analysis system[3], hosted by a DEC PDP-11/50 computer, recorded information about each physics event on magnetic tape. In addition, four special data records were recorded during each accelerator cycle. The data collection system also passed

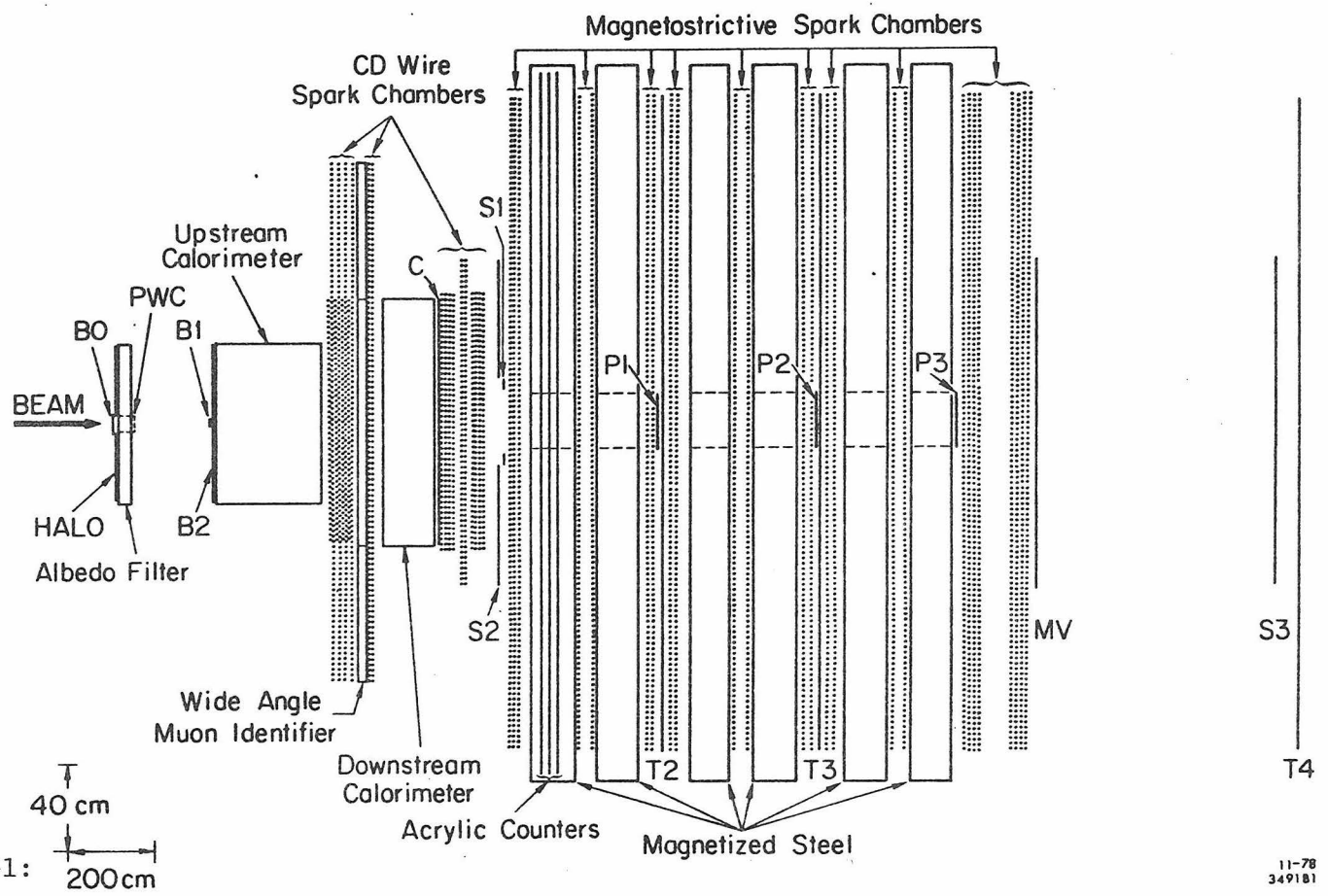

Figure 2-1: Plan view of the experimental apparatus. A 400 GeV proton beam is incident from the left. B0-2, H (HALO), C, S1-3, ACR1-3 (Acrylics), T2-4, MV, and P1-3 are all counters used in trigger logic or event selection.

a fraction of the collected events to an on-line data analysis program capable of making low level hardware operation checks, providing a graphical representation of physics events, and of performing many interactively defined data accumulation activities.

The apparatus was constructed by the members of Fermilab experiment 379[4], a Caltech-Stanford collaboration, during the period from the completion of the Lab E building in December, 1975 until the commencement of data collection (March-June, 1977). The data taken in experiment 379 can be analyzed in search of several different event topologies, containing zero[5], one[6], or two muons in the final state. The present thesis deals only with the last of these, and due to the nature of the analysis, required the utilization of data from only a few of the experimental detectors. Descriptions of the remainder of the detectors are included because of the amount of time the author spent in making them operate, but the details have been related to an appendix.

B. The N-5 Beam Line

For the portion of the run utilized in this analysis, the N-5 beam line (figure 2-2) was set to transport 400 GeV diffracted protons. The N-7 primary proton beam was tuned to deliver $\sim 2 \times 10^{11}$ protons per accelerator cycle to enclosure 100, where they were focused onto one of a number of production targets. The horizontal targeting angle was controlled by dipole magnet 7BOOT which, because of the steepness of the intensity versus production angle curve characteristic of diffractive scattering, provided a convenient means of varying secondary beam line production angle and thus N-5 beam intensity in order to compensate for varying conditions of incident primary beam intensity and quality.

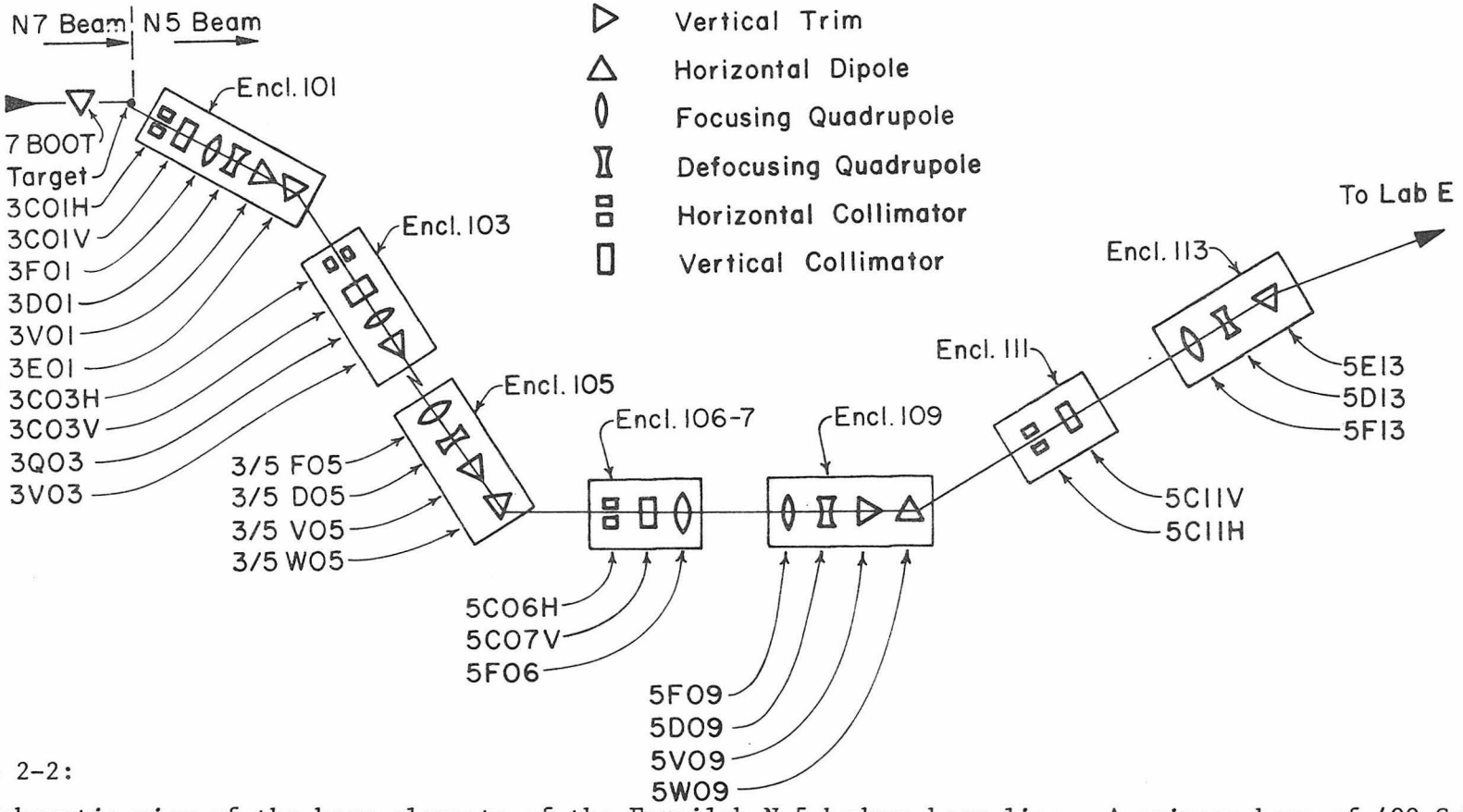

Figure 2-2:

Schematic view of the beam elements of the Fermilab N-5 hadron beam line. A primary beam of 400 GeV protons is delivered from the accelerator to the production target via the N-7 beam line. Only 10^{-5} of the primary protons are accepted by the N-5 secondary beam and delivered to the experiment.

The N-5 secondary beam consists of a number of beam line enclosures housing magnetic and/or collimation elements. The principal elements are described here. Enclosure 101 contains a pair of collimators (horizontal and vertical), a quadrupole doublet, a vertical trim magnet, and the critical east bending horizontal dipole 3E01. This last element was interlocked to all the radiation safety devices and enclosure access controls in the beam line because when shut down, it allows the beam to travel straight ahead and be dumped rather than following the beam line into the downstream enclosures.

An additional pair of collimators, a quadrupole field lens, and a vertical trim magnet were located in enclosure 103. Enclosure 105 contained a quadrupole doublet, a vertical trim magnet, and a west bending horizontal dipole. A pair of collimators and an additional quadrupole field lens were placed in enclosures 106 and 107, while enclosure 109 housed a third quadrupole doublet, vertical trim magnet, and west bending horizontal dipole. A final pair of collimators was located in enclosure 111, followed by the last quadrupole doublet in enclosure 113.

Monitoring of the beam for tuning purposes was provided by four sets of beam profile monitor wire chambers located in the various enclosures. The particles passing each wire of these chambers were counted in individual blind scalers, and a resulting beam profile histogram was constructed once per accelerator cycle by the Neutrino Area MAC-16 control computer and was displayed via the local closed circuit television (CCTV) system. The MAC computer also verified once per accelerator cycle that beam line magnet currents were within specified tol-

erances, typically 1% for quadrupoles and .05% for horizontal dipoles. Power supply regulation requirements were considerable because of the exceedingly long lever arms in the beam line (e.g. 200 meter drifts after 50 milliradian bends), with shifts of 1 ampere in a string of three half megawatt power supplies connected in series and providing 4000 amperes typically causing 1 mm beam motions at downstream locations.

The acceptance of the beam line was approximately $\Delta\Omega = .3$ μsteradians and $\frac{\Delta p}{p} = 1\%$[7]. However, the momentum spread of the beam was determined not by the line acceptance but by the width of the elastic scattering distribution entering the beam line. The $\frac{\Delta p}{p}$ of the delivered beam was typically 5×10^{-4} to within a factor of two. The spot size of the beam on target was claimed to be entirely contained in a region 1" high by 2" wide, with an angular divergence less than .1 milliradian[8]. The beam line was usually run with 10^5 - 10^6 protons per accelerator cycle reaching Lab E. Typical duty cycle was a 1.8 second long slow spill once per 16 to 18 seconds.

C. The PWC System

For the purposes of this experiment a PWC spectrometer was added to the beam line to allow determination of the individual beam particles' trajectories and momenta, enabling the rejection of off momentum (halo) particles and the accurate steering of the beam into the experimental apparatus. The spectrometer consisted of a horizontal dipole magnet and eight planes of proportional wires.

The magnet system, designated 5E13, was constructed of two main ring B-2 dipole magnets, each of which had a good field region 4" wide

by 2" high by 20' long. A current of 4900 amperes excited the system to a field of 18 kilogauss, providing an east bend of 16.4 milliradians to the incoming beam. The magnets were located approximately 20 meters upstream of the target-calorimeter.

The PWC system, provided by the Fermilab Research Services Department[9], contained eight planes of 48 wires each, arranged as four x-y pair. These were located 20 meters upstream of 5E13, directly upstream and directly downstream of 5E13, and $\sim$1 meter upstream of the target-calorimeter, as shown in figure 2-3. The spacing between adjacent proportional wires was 1 mm. The chambers were provided with a flow of dried gas 80% Ar and 20% CO_2 from manifolds running throughout the beam line enclosures.

Electronics consisting of amplifiers, discriminators, and differential ECL line drivers were located on circuit cards mounted directly on the chamber housings. This circuitry drove sets of 32 pair flat ribbon cable connected to latch cards located in a crate in the experiment counting house. Each set of three cards, containing the 96 latches for one x-y chamber pair, was provided with a single fast NIM strobe signal. The latch crate also contained a scan controller card capable of sequentially addressing the latch cards and converting their data into a string of 24 16 bit data words, with each bit corresponding to the state (hit or miss) of one particular wire. These data were then routed to a CAMAC interface card for readout.

The complete spectrometer system provided a spatial resolution of $\sigma_{space} = 1\ mm/\sqrt{12} \simeq .3$ mm and an angular resolution for a pair of chambers of $\sigma_{ang} = \sqrt{2}\ \sigma_{space}/$lever arm $\simeq .035$ milliradian for a momen-

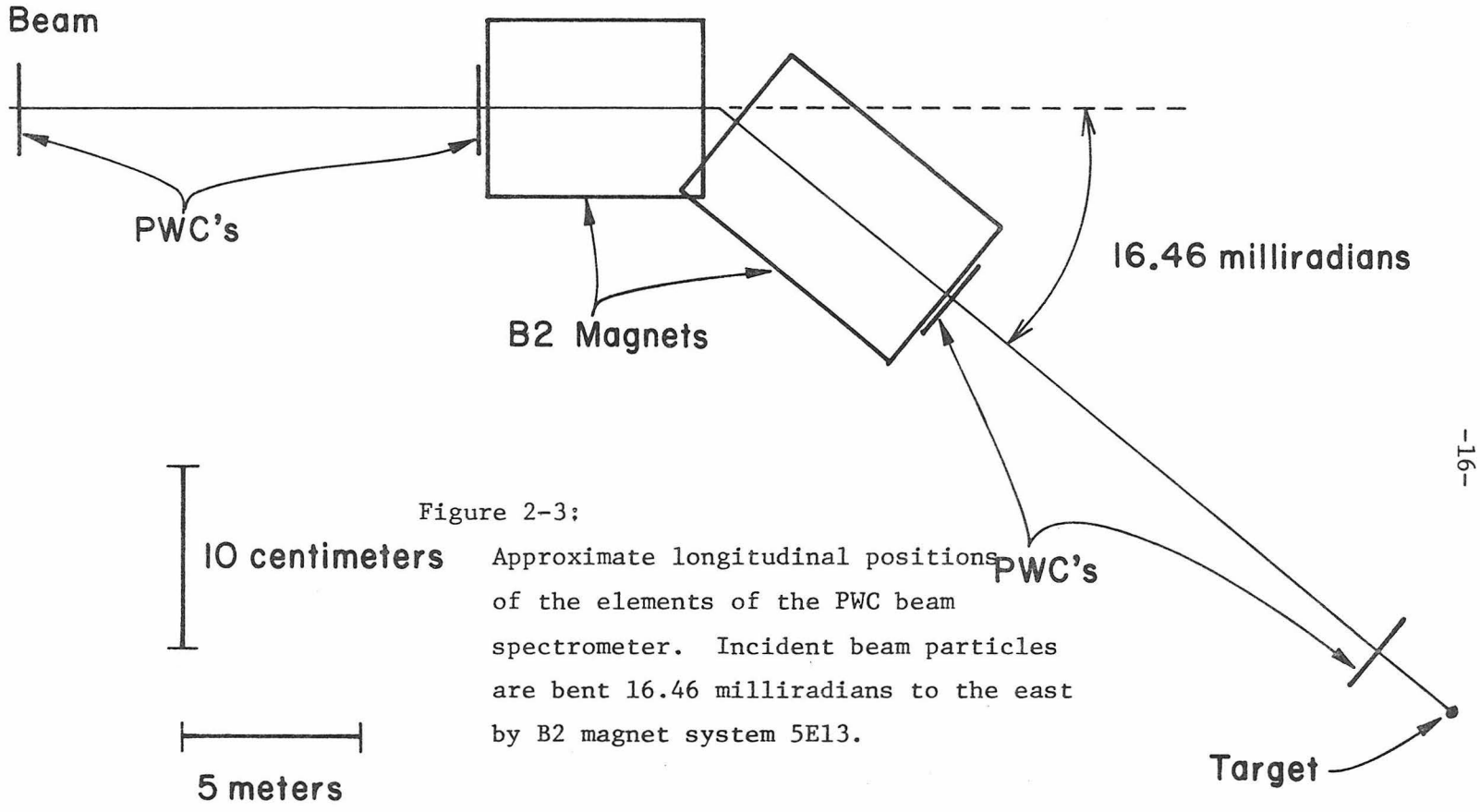

Figure 2-3:
Approximate longitudinal positions of the elements of the PWC beam spectrometer. Incident beam particles are bent 16.46 milliradians to the east by B2 magnet system 5E13.

tum resolution $\frac{\Delta p}{p} = \frac{\Delta\theta}{\theta} = \sqrt{2}\ \sigma_{ang}/\theta \simeq .3\%$. These theoretical results were verified by reconstruction of computer simulated events. However, the PWC data were not utilized in this analysis.

D. The Beam Counters

A system of three beam counters and one halo veto counter was utilized to detect particles in the incident beam. Counters B1 and B2 were transversely centered on and positioned directly upstream of the front face of the target-calorimeter, and were 2" square and 30" square respectively. The H counter, 30" square with a 2.5" square central hole cut out, was located approximately two meters upstream of B1, and was shielded from particles back scattered from interactions in the target-calorimeter by a 12" thick steel albedo shield located immediately downstream of it. The albedo shield had a profile identical to that of the counter, i.e. 30" square with a 2.5" square central cutout. One additional 3" square beam counter, B0, was located just upstream of H.

The beam as tuned for the intensities used in this data taking typically contained 5-10% halo particles, i.e. 5-10% of the good hits in B2 were accompanied by a hit in the H counter. The albedo shield was included in the apparatus to reduce the fraction of hits in H which resulted not from halo particles in the beam but rather from particle "backsplash" from interactions early in the target-calorimeter[10].

All counters were constructed of 1/4" thick plastic scintillator, with the exception of B0, which was 1/8" thick. Each scintillator was viewed by a single 14 stage photomultiplier tube of Amperex type 56AVP. Phototube anode signals were passively split, and were then routed to

both the trigger logic and to commercial 10 bit integrating pulse charge digitizers (LRS type 2249A).

The first intermediate level of logic, indicating a particle anywhere in the vicinity of the beam, was defined as BLOB = B2 · (B0 + H), where the symbol "+" denotes a logical OR and "·" denotes a logical AND. It should be noted that because of the 53 MHz radio frequency accelerating system utilized at Fermilab, beam particles arrived in discrete RF "buckets," each typically 2-4 nanoseconds wide and spaced every 18.8 nanoseconds. Beam particles in the central 2" square region of the apparatus, and unaccompanied by particles in the 30" square area during the preceding and subsequent two buckets, were then identified by BEAM = BLOB · B1 · $\overline{\text{BLOB}}_{\text{delayed}}$ · $\overline{\text{BLOB}}_{\text{advanced}}$. Finally, particles unaccompanied by in-time halo were selected via BEAM$\bar{\text{H}}$ = BEAM · B0 · $\overline{(\text{B0} \cdot \text{H})}$. These requirements were all imposed to ensure that only one beam particle entered the apparatus within the time resolution of both the PWC spectrometer and the calorimeter analogue electronics, and that the particle was likely to be at the nominal beam momentum and not be the low energy product of some beam scraping.

E. The Calorimeters

The calorimeters utilized in this experiment performed multiple functions. In addition to providing a measurement of the total hadronic energy in any given event, they served as both interaction target and muon identifiers, and provided information used in the trigger logic. The design and construction of the calorimeters were performed at Stanford University, and complete descriptions of both their assembly and

operation are provided in the thesis of J. P. Dishaw[5]. In this experiment the calorimeters were utilized as the target and hadron absorbers, but no use was made of the analogue information on hadron shower energy which they provided.

The upstream calorimeter, which also served as the target, was composed of 45 steel plates each 30" square. The upstream 20 plates were 1.5" thick, while the remainder were 2" thick. The plates, with the exception of the most downstream four, which were welded in place in order to provide structural rigidity, could be individually longitudinally positioned by sliding along rails parallel to the beam direction. This feature allowed the density of the target to be directly varied for use in the single muon final state data, where a separation of a signal from prompt and non-prompt sources is required[11]. For the portion of the running utilized in this analysis, this density variation was not necessary and so the plates were spaced as closely as feasible, with a typical spacing of 2" between the first 20 plates and 2.5" between the remainder, and all plates were positioned as far downstream as possible in order to maximize the solid angle acceptance of the Fe toroidal spectrometer system.

The second calorimeter, located ~ 1.4 meters downstream of the first unit, was intended to make a lower resolution measurement of the energy contained in the portion of the hadronic cascade escaping out the back of the first 45 plates, i.e. to improve the longitudinal containment of showers at minimal extra cost. However, in this analysis, the only purpose it served was as a muon identifier/hadron absorber. This unit was constructed from 10 steel plates 44" wide by 48" high by

4" thick.

Additional details of calorimetry counters and associated readout and monitoring electronics are contained in appendix A. The only signals provided by the calorimeters relevant to this experiment are the following: (1) F3-10, indicating greater than 50 particles observed in the analogue sum of pulses from counters after the third through tenth plates of the upstream calorimeter, and thus signifying an interaction within the first ten Fe plates; (2) E_{sum}, an analogue signal representing the total energy detected in the upstream calorimeter; and (3) W583MU, indicating three or more particles observed in plates five to eight of the downstream calorimeter.

F. The Upstream Spark Chambers

The upstream spark chamber system, consisting of two modules of ten planes each, was utilized to measure trajectories of muons immediately downstream of both calorimeters. Because of the relatively large numbers of punch through hadrons in these regions, especially the region between the two calorimeters, chambers specially designed for high multiple spark efficiency were necessary. The upstream module was located as close to the interaction region as possible in order to obtain the best possible estimate of muon production angle before large multiple coulomb scattering occurred, while maintaining the ability to distinguish individual tracks. The second module was located in a region where essentially all surviving charged particles were muons (3 meters of Fe downstream of the interaction point), and after matching tracks with the upstream module, indicated which upstream tracks were indeed

muons, and provided the best estimate of their trajectories upon entering the magnetic field region of the spectrometer.

Details of chamber construction have previously appeared elsewhere[12], so only a brief summary will be given here. Each module contained 4 x planes, 4 y planes, and one tilted u-v plane pair. Plane dimensions and u-v rotation angles are given in table 2-1. Readout wires were located every 1.06 mm, and were attached to individual capacitor-diode network elements. A recirculated gas mixture of 90% Ne and 10% He with a small admixture of 1-propanol was utilized. High voltage pulses of 8 kv typical amplitude were applied to the chambers via groups of thyratron switched charged delay lines. DC clearing fields of 85 volts upstream and 50 volts downstream were applied to reduce the number of old tracks causing sparks in the chambers. These had the unfortunate effect of reducing efficiency in the upstream chambers. The operating points chosen reflected a careful compromise between efficiency and chamber saturation. System dead time for high voltage recharge was nominally 20 milliseconds.

The spark chamber readout hardware was considerably modified for use in this experiment in order to allow for direct memory access (DMA) readout on a PDP-11. Two UNIBIN modules, one capable of becoming bus master, were interfaced to a data scanner and modified formatter. The scanner addressed successive groups or boards of 32 sense wire and searched for clusters of adjacent struck wires on each board. One 16 bit data word was constructed by the formatter for each cluster on a board. The data consisted of 6 bits containing the board number, 5 bits specifying the last struck wire in the cluster, and 5 bits of cluster width. Spark clusters extending over a board boundary generated two

TABLE 2-1

UPSTREAM SPARK CHAMBER CHARACTERISTICS

Characteristic	Upstream Module	Downstream Module
Size of first two x-y chamber pair	2.2 by 1.2 meters	1.2 by 1.2 meters
Size of second two x-y chamber pair	1.2 by 2.2 meters	1.2 by 1.2 meters
Size of u-v chamber pair	2.0 by 2.3 meters	1.7 by 1.7 meters
Tilt angle of u-v chamber pair	317 milliradians	784 milliradians

data words, one for the portion of the cluster on each board. One additional word containing 5 bits of plane identification number was generated before the scan of each plane was initiated.

Two stand alone test programs for the readout system were developed and were typically run once per week or whenever readout trouble was suspected. One of these checked the operation of the PDP-11 DMA readout hardware, while the other verified the ability of each individual wire to record either a hit or a miss.

The chambers had a typical final resolution of from .3 to .5 mm. The average single spark efficiency for the first module was 85%, while that for the second module was 94%.

G. The Toroidal Muon Spectrometer

The Lab E Toroidal Muon Spectrometer[2] was used in this experiment to measure the momenta of all observed muons and to provide additional triggering information. The spectrometer consisted of an 11.5' diameter steel magnet assembly interspersed with 16 planes of spark chambers to measure muon trajectories and numerous scintillation counters, all mounted on three magnet carriages and an additional spark chamber cart.

The magnet was constructed of 24 11.5' diameter steel discs each nominally 8" thick. These laminations were grouped into six half toroids of four discs each, with each pair of half toroids sharing common coil assemblies consisting of four packages of 12 turns each. A 10" diameter central hole was provided through each lamination to provide for coil return. A current of 1250 amperes provided an excitation of 60,000 ampere turns. The total $\int B_\phi dz$ of the magnet system was 80 kilogauss

meters, for a transverse momentum kick of 2.4 GeV. The momentum resolution obtained was limited by multiple scattering, and was 10% independent of momentum for particles traversing the entire magnet.

Each magnet lamination was composed of two semicircular halves split along the horizontal diameter. A series of small 3/8" high aluminum shims was inserted between the two halves of each disc, creating 3/8" air gaps in the laminations, and thus allowing insertion of a Hall probe to measure the magnetic field. The computer program TRIM[13] was used to calculate the shape of the field at all radii and azimuths. Agreement of this calculation with the Hall probe measurement to 1.5% at the one azimuth accessible for verification was used as justification for believing the TRIM result at all radii and angles.

A simple parameterization for the field shape calculated by TRIM was developed: $B(\text{kilogauss}) = 17.4 + A(\phi) \cdot (57.15 - r)$, where r is the cylindrical radius in centimeters. The slope $A(\phi)$ was given by $.072 - .01269 \cdot \phi^2$ when r was less than 57.15 centimeters. Here ϕ on $[-\pi/2,\pi/2]$ is the azimuthal angle from the horizontal. For r greater than 57.15, two azimuthal regions were considered. Defining ϕ on $[0,\pi]$ now as the absolute value of the azimuthal angle from the upward vertical, $A(\phi)$ was given by $.0252 - .861 \cdot (\phi - 2.484)^2$ for ϕ between 2.372 and 2.596 radians, and by the constant value .0144 elsewhere. The former azimuthal region corresponded to the portion of the magnet near the legs supporting each lamination. This field shape was then adjusted by an individual multiplicative constant for each disc so that the calculated field multiplied by disc thickness agreed with a measurement of $\int B_\phi dz$ made with the Hall probe in the air gap at a radius near 38".

H. The Toroid Detectors

Fifteen 10' by 10' planes of magnetostrictive readout wire spark chambers were assembled from 5' by 10' units previously used and described by Caltech neutrino experiment 21 at Fermilab[14]. Two of these planes were located upstream of the first half toroid, two downstream of each of the first four half toroids, one downstream of the fifth half toroid, and four downstream of the entire magnet. A sixteenth plane consisted of a single prototype 10' by 10' chamber of similar design, and was also located immediately downstream of the magnet. One plane upstream of the entire magnet and one downstream were u-v oriented with tilts of $\sim$110 milliradians; the remainder were x-y planes.

The chamber pulsing system was upgraded for use in this higher repetition rate experiment by decreasing the size of the capacitor recharging resistors in all pulsers. In addition, large capacitor banks were utilized to store charge at the output of each high voltage power supply, and the regulation circuitry of the supplies was reworked to provide lower effective output impedance. The upgraded system operated reliably with 20 millisecond recharging dead time and average rates of 20-25 pulses per second.

The gas system for the spark chambers was also improved, with the aims of providing lower leak rates and reduced system flow impedance, thus allowing the use of lower operating pressures. A gas mixture of 90% Ne and 10% He with added ethanol was employed.

The revised chamber readout system, first utilized in E-21A but never previously described, was again used here. Signals from the wand

preamplifiers were connected to pulse center finding modules, where they were further amplified by 733 integrated circuits. The center of the wand pulse from each spark was found by searching for the coincidence of positive signal with negative time derivative of the signal. This coincidence generated a 75 nanosecond long TTL inverse logic pulse, which was routed to the input of a standard SPEAR "ANNA" multi-time digitizer (MTD) module[15].

The MTD CAMAC module, which could process the pulses from 4 chamber wands, operated by starting to count a 20 MHz clock in a 16 bit wide scaler whenever a conversion cycle was initiated. When a wand pulse center was detected, the current contents of this scaler were loaded into the next available location of a 16 bit wide by 16 word random access memory (RAM). Overflow of the 20 MHz scaler ended conversion, and caused an additional word of all zeroes to be loaded into the next location of the RAM. The null word served to flag the end of valid data at readout time. The system thus had the capability to digitize 15 sparks, two of which were typically fiducial marks, on any wand, instead of the 4 sparks past first ficucial capability of the SAC system previously employed.

The resolution of the toroid spark chamber system varied from .3 to 1.0 millimeters. Typical chamber efficiencies of 90% were realized.

The spectrometer magnets were constructed with 2" wide gaps between successive laminations. These were destined to be filled with 10' by 10' acrylic-base scintillation counters[16]. However, at the time these data were taken, only the first 3 of these 24 counters had been installed. The acrylic counters were particularly useful in the

construction of the event trigger described in section I of this chapter and section B of chapter IV.

The acrylic scintillators consisted of 4 separate quadrants, each composed of three 5' by 5' by 1/2" thick sheets of acrylic plastic to which scintillation fluors and blue wavelength shifter had been added. Wavelength shifter bars on all four sides of each quadrant reemitted the collected blue light in the green portion of the spectrum, and conveyed this light to a total of 10 RCA type 6342A 2" diameter 10 stage photomultiplier tubes per 10' by 10' plane. The use of the shifter bar technique enabled collection of light from almost 1500 square inches of scintillator edge surface onto only 30 square inches of photocathode, with an efficiency greater than 10%.

The phototube outputs were routed through LRS type 612 amplifiers. Signals from the two tubes of each plane which viewed each quadrant (and no other) were then mixed and fed through an LRS 335 amplifier before being discriminated. A 2 out of 3 fold majority of the installed planes was then used to define a particle passing through a particular quadrant.

Two additional 10' by 10' planes of standard plastic scintillator were also located in the spectrometer. Counter T2 was located downstream of the second half toroid; T3 was downstream of the fourth half toroid. Each plane was composed of two 10' wide by 5' high by 1" thick halves, with a pair of RCA type 4522 5" diameter 14 stage photomultipliers on each half.

I. The Trigger Counters and Trigger Logic

In addition to the beam counters (section D) and spectrometer trigger scintillators (section H), a number of fast counters were used in the primary physics trigger. A series of coincidence latches and blind CAMAC scalers were used to monitor the efficiency and counting rates of the triggering system. The conceptual design of the trigger is described in section B of chapter IV.

The C hodoscope, located downstream of the second calorimeter, was a 4' by 4' array consisting of four 2' by 2' counters, each viewed by a single Amperex 56DVP 2" diameter 14 stage phototube. The S1 counter, located just upstream of the spectrometer, was 16" square with a 12" diameter central hole. The scintillator was split into upper and lower halves, with an RCA 6655A 2" diameter 10 stage phototube on each half.

The S2 and MV hodoscopes were both constructed from rectangular "paddle" counters 10" wide by 60" long, with 6655A tubes on both 10" edges. The S2 array, located immediately upstream of S1, consisted of 2 groups of 4 counters each, with the long dimension of elements of one group oriented vertically and the other horizontally. Each set of 4 counters extended over two regions 20" by 60", with an empty central band 16" by 60" between the two. Thus two counters were located entirely above the beam axis, two entirely below, two to the west (left, looking downstream), and two to the east. The MV hodoscope, placed against the downstream wall of Lab E, utilized 6 counters with long dimensions horizontal to form an array 60" square.

Small circular veto counters P1-3, each 12" in diameter and viewed

by a single 6655A tube, were located behind the magnet coil return holes downstream of every second half toroid. The remaining scintillators, each 64" high by 70" wide by 1" thick, were placed in a separate building, the "doghouse," downstream of Lab E. Each counter was equipped with a single 4522 photomultiplier. One of these, S3, was centered on the beam line, while the remaining four were configured into 140" by 128" hodoscope T4.

Multiple intermediate levels of logic were utilized to construct the high transverse momentum muon triggers (PT).

$$S_{vh} = (S1_h \cdot S3) + S2_v + S2_h$$

$$Q_{vh} = ACR_{vh} \cdot C_{vh} \cdot T2_h \cdot T3_h$$

$$T4^{sum} = \sum_{vh}\sum T4_{vh}$$

$$MT4_{vh} = MV_h + T4_{vh} + (MV^{fuzzy} \cdot \overline{P2}) + (MV^{fuzzy} \cdot W583MU)$$

$$PT_{vh} = S_{vh} \cdot Q_{vh} \cdot T4^{sum} \cdot MT4_{vh}$$

Here the subscript v takes on the values west or east while h takes values up or down. The four signals represented by the symbols $S2_v$ and $S2_h$ each refer to the logical "or" of the 4 phototubes on 2 paddle counters which were entirely located in the indicated half plane. ACR_{vh} indicates the 2 out of 3 majority logic signal described in section H. A T2 or T3 signal represents the "or" of two tubes on one 5' by 10' half counter, while MV_h is the "or" of 6 tubes on 3 counters in one half of the MV array. The MV^{fuzzy} signal is the "or" of 4 tubes on the 2 counters of MV closest to the beam axis, while W583MU represents an analogue signal greater than 2.5 times minimum ionizing in the linear

sum of the 16 counters in planes 5 through 8 of the downstream calorimeter/muon identifier.

A logic signal (IB), indicating a good particle interacting in the upstream portion of the target, was defined by the coincidence of signals BEAM$\bar{H}$ (see section D) and F3-10 (see section E). The final requirements on beam particles, that they be unaccompanied by additional beam in the preceeding and subsequent 5 RF buckets, were implemented by defining IBV = IB $\cdot$ $\overline{(E_{sum} > 600\ GeV)}$ $\cdot$ $\overline{BO}_{delayed}$ $\cdot$ $\overline{BO}_{advanced}$. Total and live time fluxes in both IB and IBV were monitored by Jorway 85A blind scalers read once per accelerator cycle. The final experiment PT trigger was constructed via TRIGGER = $\sum_{h}$ (IB $\cdot$ IBV $\cdot$ $\sum_{v}$ PT_{vh})

J. The Data Collection System

The on-line data collection and analysis system was located in a DEC PDP-11/50 minicomputer, run under a modified version of the RT-11SJ V02C operating system. This system was responsible for the collection and recording of all events, and for the analysis of whatever fraction of these events was permitted by time.

The computer was connected to a CAMAC branch highway via a Jorway branch driver capable of DMA operation with double buffering. A CAMAC serial driver was located in one of the branch crates, and was used to drive a serial highway into Lab E, where the LED pulsing system was located. The branch crates contained most experiment readout modules, including ADC's, coincidence latches, MTD's, blind scalers, PWC readout, and calorimetry monitors.

A single UNIBIN, a crate with PDP-11 UNIBUS directly accessible on its backplane, was used for upstream spark chamber readout and for additional calorimetry monitoring. This bin has the advantage that modules located in it can be addressed directly via single machine instructions rather than indirectly through an interface such as a branch driver and its appropriate software handler.

The software was divided into two distinct parts: data collection and data analysis. During the beam spill, a data collection program constructed event records in a series of core buffers, the contents of which were subsequently transferred to a disc buffer. When the beam spill had ended and all core buffers had been spooled to disc, the collection program was replaced by a routine which transferred the disc buffer contents to magnetic tape. The data analysis program MULTI, which had been checkpointed to disc to make room for core buffers during the spill, was also restored and restarted, proceeding to analyze the disc buffer contents.

The MULTI system contained two major components. The basic system is an experiment independent program providing interactive histogram construction, scatterplots, expression evaluation, and numerous displays as well as useful facilities such as dynamically assigned memory, a dictionary of variable names, syntax analyzer and sentence parser, and graphics capabilities. The "user appendages" contain routines to perform data analysis and display construction germane to a particular experiment. Tasks such as monitoring of ADC pedestals, LED pulse heights, and spark chamber ficudial efficiencies and conversion of ADC counts to pulse heights in equivalent minimum ionizing particles or of spark chamber

clock counts or encoded hits into spark coordinates in space were performed by code falling into this classification. User generated displays included schematic representations of events, running averages of hadron shower longitudinal development and spark chamber hit counts and spark widths, and calorimeter reference tube NaI pulse height spectra, in addition to pure text displays of raw or partially processed hardware interface data.

REFERENCES

2-1 J. Lach and S. Pruss, Fermilab Memo TM-285, (1971).

2-2 Appendix II, Fermilab E-379 agreement, (1975).

2-3 MULTI, the creation of J. F. Bartlett, is now a data collection system supported by the computer department of Fermilab.

2-4 B. C. Barish, J. F. Bartlett, A. Bodek, K. W. Brown, M. H. Shaevitz, and E. J. Siskind of Caltech; and A. M. Diamant-Berger, J. P. Dishaw, M. Faessler, J. K. Liu, F. S. Merritt, and S. G. Wojcicki of Stanford.

2-5 J. Patrick Dishaw, Ph.D. thesis, Stanford University.

2-6 K. Wyatt Brown, Ph.D. thesis, California Institute of Technology.

2-7 J. Ritchie, Fermilab Memo TM-805 and addenda, (1978).

2-8 J. P. Dishaw, private communication of results of TRANSPORT runs.

2-9 Design, construction, installation, and maintenance by M. Atac and J. Urish.

2-10 G. B. Yodh et al., Proceedings of the Calorimeter Workshop, Fermilab, page 201, (1975).

2-11 B. C. Barish et al., Caltech preprints CALT 68-655 and CALT-68-686; K. W. Brown et al., CALT 68-666 and reference 2-6.

2-12 R. Coombes et al., Nucl. Inst. and Meth. 98, 317, (1972).

2-13 J. S. Colonias, "TRIM: A Magnetostatic Computer Program for the CDC 6600," University of California at Berkeley Lawrence Radiation Laboratory publication UCRL 18439, August, 1968.

2-14 Frank S. Merritt, Ph.D. thesis, California Institute of Technology, (1977).

2-15 B. Bertolucci, I.E.E.E. Trans. on Nucl. Sci. NS-20, 361, (1973).

2-16 B. Barish et al., I.E.E.E. Trans. on Nucl. Sci. NS-25, 532, (1978).

CHAPTER III

DATA REDUCTION

A. Overview

The thrust of the initial data analysis was towards the reconstruction of all tracks upstream of the spectrometer and the momentum determination of that subset of tracks which traversed at least the first half toroid. Thus the data reduction consisted of the preparation from abstracted raw data of summary tapes (DST's) containing track rather than spark information, but with all other quantities relating to an event left unchanged. All events on the DST's containing reconstructed $\mu^+\mu^-$ pairs were then selected and written onto condensed summary tapes (CST's).

All data reduction and simulation described in this thesis were performed on the CDC 7600 system at Lawrence Berkeley Laboratory, using the Caltech COPE link for remote job submission. The input data sample of 105 raw 9 track 800 BPI tapes, containing $\sim 1.3 \times 10^{10}$ bits of information, was reduced to a single merged CST requiring less than one 6250 BPI reel, and consisting of $\sim 2.4 \times 10^{8}$ bits.

Data summary tapes were prepared using the ψ reconstruction version (ANAL379) of the program TIOGA. Reduction of the abstracted version of one raw data tape required 50 to 60 seconds of computation; operation on raw unabstracted data required 240 to 275 seconds per tape.

A summary of the types of records on raw data tapes is given in table 3-1. The DST preparation modified only physics events and end spill records. The pedestal and LED calibration events and begin spill records were left in the DST in their original form. Processing of end spill records consisted simply of summing the fluxes in IB and IBV (see

TABLE 3-1

TYPES OF RECORDS ON RAW DATA TAPES

Type	When Collected	Purposes/Contents
Physics Event*	Upon event detection	Description of event.
Pedestal	Before each spill	Determine zero offsets in ADC's.
LED	Before each spill	Verify operation of counters with LED's; determine tube gain with light flasher.
Begin Spill	Before each spill	Determine gain of NaI reference tubes between beam spills.
End Spill	After each spill	Determine gain of NaI reference tubes during beam spill; read blind scalers containing beam fluxes and tube singles rates.
Begin Run	First record of run	Text describing run purpose and running conditions.

*Physics events include both high transverse momentum muon triggers (section B of chapter IV) and interacting beam triggers (section B of chapter III).

section I of chapter II) signals for beam normalization. The end spill record written to the DST was identical to the raw data tape version with the exception that the record was truncated to remove the portion containing data from the blind scalers.

B. Preliminary Raw Data Abstraction

Before any attempt at event reconstruction was made, raw data tapes were run through the abstraction program ABS2AC, which retained only those events which could possibly be useful to a ψ analysis. Operation of this program required ~ 7 seconds of computer time, of which ~ 5 seconds were exclusively for I/O operations, per raw data tape. This step reduced the actual size of the data sample by at least a factor of 3 by removal of physics events containing only one muon or muon pairs with low (i.e. $\leqslant 1$ GeV) invariant mass, and reduced the processing time by a minimum factor of 4. The time reduction was larger than the data volume reduction because much of the content of the abstracted tape was composed of calibration events requiring minimal (or no) reduction.

Events retained consisted of all non-physics records, including ASCII begin run logs, begin and end spill events, and pedestal and LED calibrations, plus a sample of physics events. This latter sample included all interacting beam triggers (events triggered on every 16384th good beam particle with no additional requirements) for calibration of the calorimeters, plus those high transverse momentum muon triggers (see section B of chapter IV) in which hits in two or more quadrants of the toroid acrylic (ACR) counter system were observed. This last two quadrant requirement was designed to be a simple cut to ensure the

presence of two muons with a large opening angle in a trigger which only required one muon, and effectively reduced the number of muon triggers by about one order of magnitude while maintaining relatively high efficiency for the high mass ψ state.

For the purpose of this abstraction, a quadrant hit was defined as either a count in the 2 out of 3 majority logic circuit or counts in 2 or more of the 3 individual planes of the ACR counter (section H of chapter II contains details of ACR counter construction). The small difference between these two definitions was due primarily to the looser timing requirements imposed on observing counts in the individual planes.

C. Track Reconstruction

Track reconstruction proceeded in a straight line flow. First, all hardware related raw data were converted into spark coordinates in centimeters. At this time, various status checks were made on hardware performance, and a small fraction, typically 2.5%, of events was rejected as containing possible hardware failures. After these operations, sparks in the upstream capacitor diode (CD) chambers and spectrometer magnetostrictive (CIT) chambers could be treated completely equivalently.

Straight line segments were found separately in the horizontal (x) and vertical (y) projections of both modules of the upstream chambers. These segments were then correlated using the appropriate rotated u-v chambers. Next, the lines in the two modules were matched with one another. Unmatched segments were then used as input to various routines designed to find events where chambers were inefficient, events where

pairs of tracks were degenerate in either the x or y view, events containing extremely wide angle tracks, and particles which suffered severe multiple scattering in traversing the downstream calorimeter/ muon identifier.

After all upstream tracks had been found, a similar search was made for straight correlated lines in both x and y projections in the spark chamber cart downstream of the spectrometer magnet. Both these lines and the previously found upstream fully matched tracks were then used as input to a toroid track search routine using an algorithm based on conservation of angular momentum. This algorithm utilized the fact that, expressed in a cylindrical coordinate system with a z axis along the toroid axis, the magnetic field in the spectrometer was entirely in the ϕ (azimuthal) direction, and thus the ϕ component of a particle's angular momentum was not changed by the field. This method does not require that the toroids be centered on the incoming beam axis. In that case (these data), the azimuthal component of the angular momentum should always have the constant value zero.

D. Momentum Fitting

Toroid tracks were momentum fitted by an iterative method capable of rejecting existing sparks in a track and searching for new ones. Finally, the fitted momenta were corrected for energy loss resulting from traversing the calorimeters, assuming that the longitudinal (z) position of the primary event vertex was located at the upstream face of the target-calorimeter. For determining transverse momentum, the measured slopes of the track in the upstream module of the CD chambers

were assumed to reflect the muon directions at the production vertex, and no correction for multiple scattering in the upstream calorimeter was employed. The smearing of transverse momentum resulting from this scattering was compensated for by the acceptance calculations (see section F of chapter IV).

The detailed operation of the spark chamber processing and track reconstruction routines is contained in appendix B, as are descriptions of the various χ^2 cuts employed and normalizations used in calculating the χ^2.

CHAPTER IV

TRIGGERING, TRIGGER ACCEPTANCE, SMEARING, AND RECONSTRUCTION EFFICIENCY

A. Overview

The data for this experiment were collected using a trigger designed to accept a single positive muon of large (i.e. $\gtrsim 1$ GeV) transverse momentum (p_t) with no bias against additional muons. If no p_t requirement had been imposed and instead the experiment were triggered on any muon, we could estimate the trigger rate by assuming 10 pions produced per event and 10^{-4} muons per pion, or a rate of 10^{-3} per incident proton. However, experiment dead time effects necessitated a maximum trigger rate of order 4×10^{-5}, and thus the p_t cut was imposed to lower the raw trigger rate by the necessary factor of 25 while maintaining good sensitivity to muons produced by the decays of high mass states.

The pre-analysis abstraction cut (see section B of chapter III) requiring hits in two quadrants of the toroid acrylic counters ensured that two muons were present, that the opening angle between the muons was large and thus the mass of the muon pair was likely to be high, and that both tracks were sufficiently far from the toroid central hole that the probability of reconstructing their momenta was large. This cut reduced the initial data set of ~ 100 tapes containing $\sim 10^4$ p_t trigger events each to a more tractable sample of approximately 1.5×10^5 events.

The trigger acceptance and smearing corrections as well as effects of resolution were calculated using the Monte Carlo program MCR379. This program could be run in several modes, and was capable of calculating distributions in laboratory variables (energy, transverse momentum,

etc.) of particles given any set of assumptions on center of mass production parameters and decay probabilities, of mapping trigger efficiency as a function of any variable, and of generating an output tape of simulated data identical in format to raw data tapes from the experiment. These tapes were then processed by the usual reconstruction programs, providing an estimate of both reconstruction efficiency and smearing errors.

B. The P_t Trigger

The high p_t trigger utilized the fact that the toroidal spectrometer was centered on the incoming beam axis to select only those muons whose p_t exceeded a threshold value which was independent to lowest order of the particles' total momentum. The trigger was constructed by requiring that a muon remain in the same azimuthal quadrant of the apparatus until it reached the MV counter downstream of the spectrometer, i.e. by requiring hits in the same quadrant of all counters. The actual trigger logic is described in section I of chapter II, while the trigger efficiency as a function of p_t of the muon is detailed in section D of this chapter.

Figure 4-1 presents examples of "typical" muon trajectories in the apparatus. If a particle's trajectory is described in cylindrical coordinates and if multiple scattering and any small radial components of the toroids' magnetic fields are ignored, the particle moves in a plane of constant azimuth starting from a radius (r) of zero at the longitudinal position of the interaction point (z_{ip}). If we further neglect the effects of energy loss in the steel of the calorimeters and

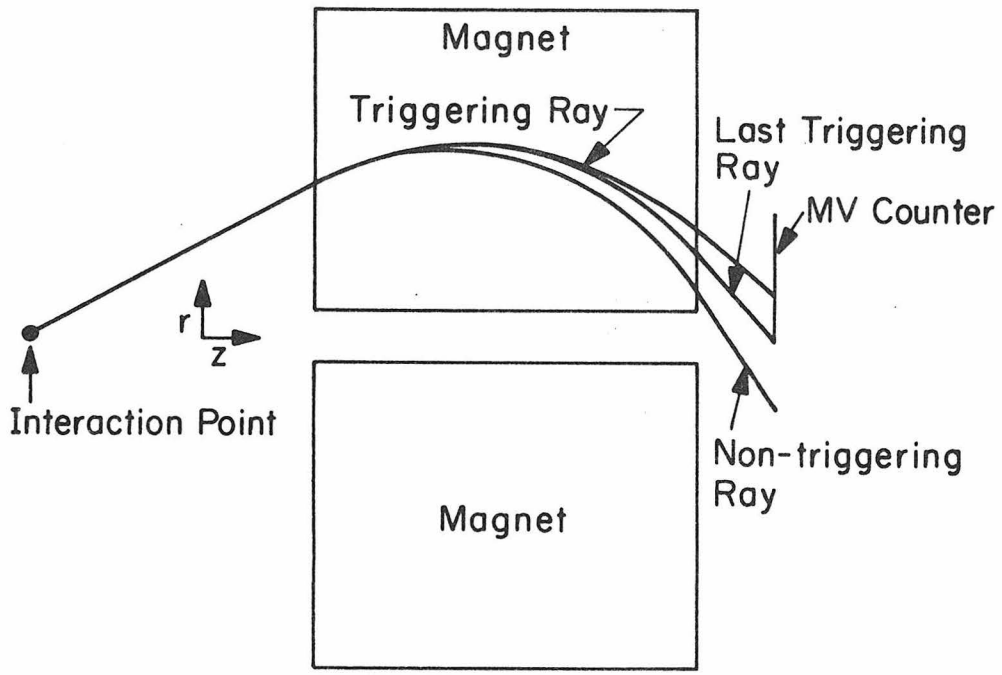

Figure 4-1:

"Typical" muon trajectories in a plane of constant azimuth. Those focusing (positive) muons which remain in the same quadrant of the toroidal magnet until passing the MV counter (one half of which is shown) trigger the apparatus.

toroidal magnets and approximate the effect of the magnetic field by a point kick of magnitude p_t^{mag} at the longitudinal position of the center of the magnet (z_{mag}), then the radius of the trajectory of a positive (i.e. focusing) muon at z_{MV} downstream of the magnet is given by $r = (z_{MV} - z_{ip})p_t/p - (z_{MV} - z_{mag})p_t^{mag}/p$. The condition of no cross-over to the opposite quadrant is just that r be positive, or that p_t of the positive muon be greater than $p_t^{mag}(z_{MV} - z_{mag})/(z_{MV} - z_{ip})$ independent of p.

The above condition breaks down if the muon path passed through the hole in the center of the toroidal magnet. In order to remove rays passing through the hole, which subtended an angle of 22.5 milliradians in the laboratory when viewed from the interaction point, the trigger required a hit in either of the S1 or S2 counters upstream of the magnet front face. These counters covered a region essentially 5' square with a 1' diameter central hole cut out (see section I of chapter II for details). Negative muons which did not enter the toroid central hole were typically defocused entirely out of the spectrometer magnet, and so did not trigger the apparatus.

C. The Monte Carlo Program

The acceptance of the trigger and associated cuts, and the effects on measured variables due to experimental resolutions were studied using Monte Carlo techniques. The Monte Carlo program consisted of the following major portions: incident beam particle momentum and interaction point position and inclination angle simulation, generation of parameters in the center of mass frame of all relevant leptons, transforma-

tion of lepton momenta to the laboratory system, ray tracing of all muons, trigger logic simulation, and raw data output generation. Any number of these sections could be skipped; e.g. if only histograms of laboratory momenta were required, the execution could be terminated before ray tracing; if acceptances were desired as a function of laboratory parameters, rays could be generated directly in the laboratory frame with any desired distribution.

Trigger efficiencies or effects of data cuts could be calculated differentially by bin-wise division of histograms of accepted events by generated events. This allowed the concentration of generation statistics in any interesting portion of a distribution, or alternatively provided good statistical errors on acceptance in precisely the regions where events naturally occurred.

Ray tracing through the apparatus proceeded in a series of discrete steps, with one step for each plate in the calorimeters or for each lamination of the toroids. For each step energy loss was calculated corresponding to the momentum of the particle and its actual path length for the step. Multiple scattering was simulated in each step separately in both vertical and horizontal projections according to a joint gaussian distribution in scattering angle and displacement. Effects of energy loss and multiple scattering in any material other than steel were ignored, as were fringe magnetic fields in the toroid central hole and outside the magnet.

It should be emphasized that the Monte Carlo procedure is almost entirely model independent. Once the momenta of muons in the center of mass frame are specified, the acceptance for an event is entirely

determined by the known geometry of the apparatus and modified only by the effects of multiple coulomb scattering and energy loss. Although our knowledge of these effects can hardly be questioned, it is gratifying to note that the observed and calculated widths of the ψ peak were essentially identical.

The only question that can then be raised as to the validity of the Monte Carlo is one of whether the assumed distributions for ψ production and decay are consistent with those measured in this experiment. The initial values of all such parameters were taken from the published data of Branson et al.[1], and were modified via three iterations of Monte Carlo generation until the assumed values lay within one standard deviation from the fitted data values. In addition to the confidence inspired by this consistency, it should be noted that the differential efficiency is independent of the assumed distribution, and that in addition, the efficiency was relatively slowly varying; i.e. for each bin of the differential efficiency, the systematic errors calculated by varying the parameters of distributions in other variables by one standard deviation were smaller than the statistical errors in the efficiency.

D. Trigger Efficiency

In order to determine the efficiency of the p_t trigger for single positive muons the Monte Carlo was run for 40,000 events uniformly distributed in momentum from 10 to 50 GeV and in transverse momentum from 0 to 2 GeV. The results showed an efficiency versus p_t which was virtually independent of p from 17 to 50 GeV. A typical efficiency plot,

for muons of momentum between 20 and 30 GeV, is shown in figure 4-2. The trigger had a limiting efficiency of .9, due to multiple scattering between quadrants and dead regions in counter planes, and reached 10%, 50%, and 90% of this value at p_t of .7, 1.0, and 1.3 GeV respectively.

A two dimensional plot of positive muon acceptance region in the laboratory is presented in figure 4-3. The horizontal boundaries represent the p_t cut of the trigger, while the vertical line indicates the effective range cut introduced on the muon total momentum. The oblique lines at constant angle represent the laboratory angles of the inner and outer radii of the toroidal magnet at the magnet front face.

E. Transverse Momentum Distribution of ψ Decay Muons

Before entering into the results of a detailed calculation of the p_t distribution of muons from ψ production and decay, one can gain a rough feeling for the acceptance of the trigger for such events by noting that a "typical" ψ is produced essentially at rest in the center of mass of the initial 400 GeV proton-nucleon collision. In addition, if the angular distribution of decays is flat, the most solid angle for decay occurs at 90° in the center of mass. Thus, typical muons from ψ decay have p_t of 1.5 GeV and energies of 23 GeV in the laboratory, and therefore fall well within the region of trigger acceptance.

The experiment Monte Carlo was usually run assuming that ψ's were produced according to $\frac{d^3\sigma}{dP_t^2\, dx_F\, d\cos\theta^*} \propto e^{-2.08\, P_t}\, (1 - |x_F|)^{4.65}$, where θ^* is the s channel helicity angle of the μ^+ (also known as the Jacob-Wick angle), i.e. the angle between the μ^- and the system recoiling from

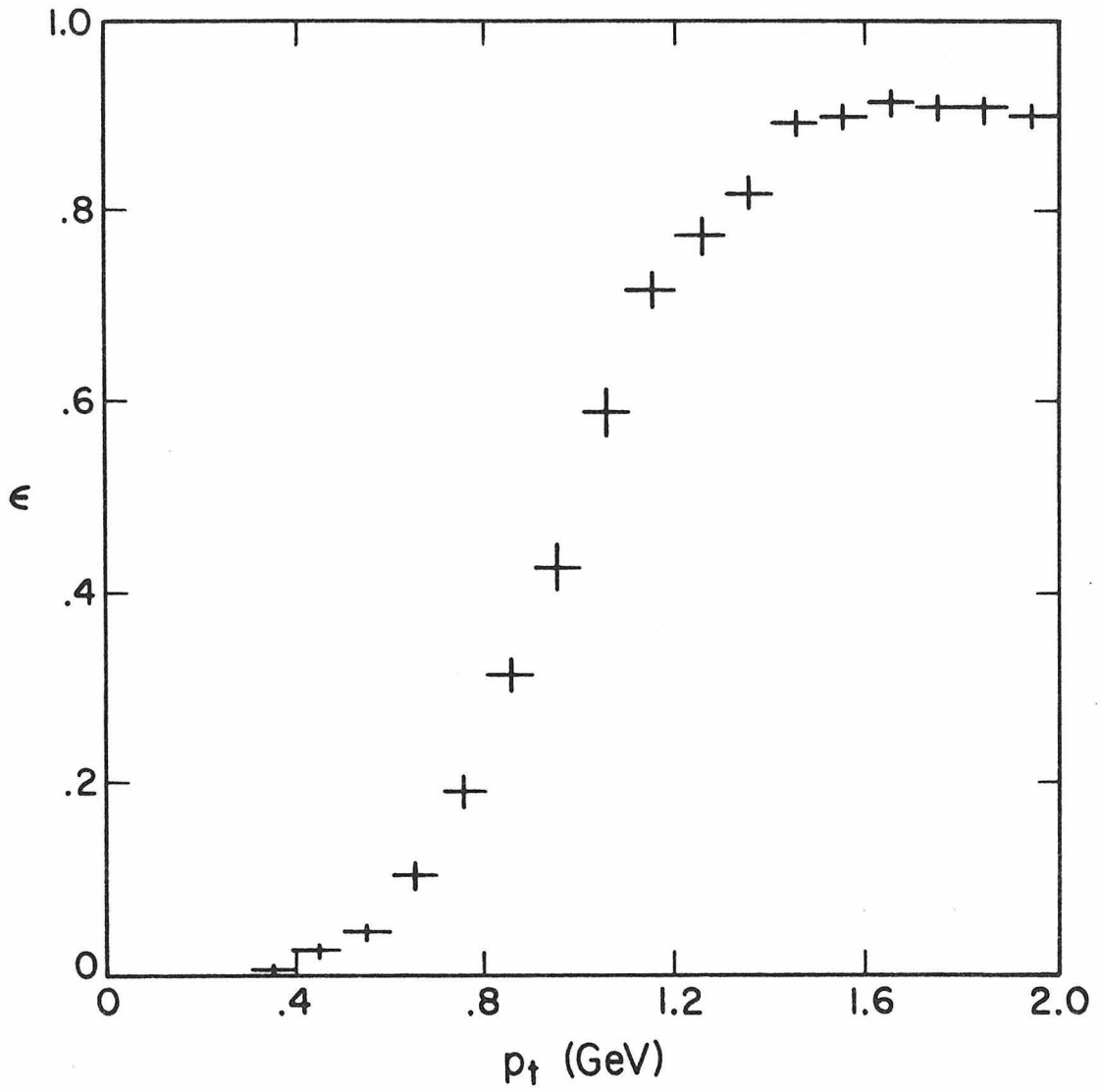

Figure 4-2:

Calculated efficiency (ε) of p_t trigger for single positive muons uniformly distributed in laboratory momentum from 20 to 30 GeV, as a function of muon transverse momentum (p_t).

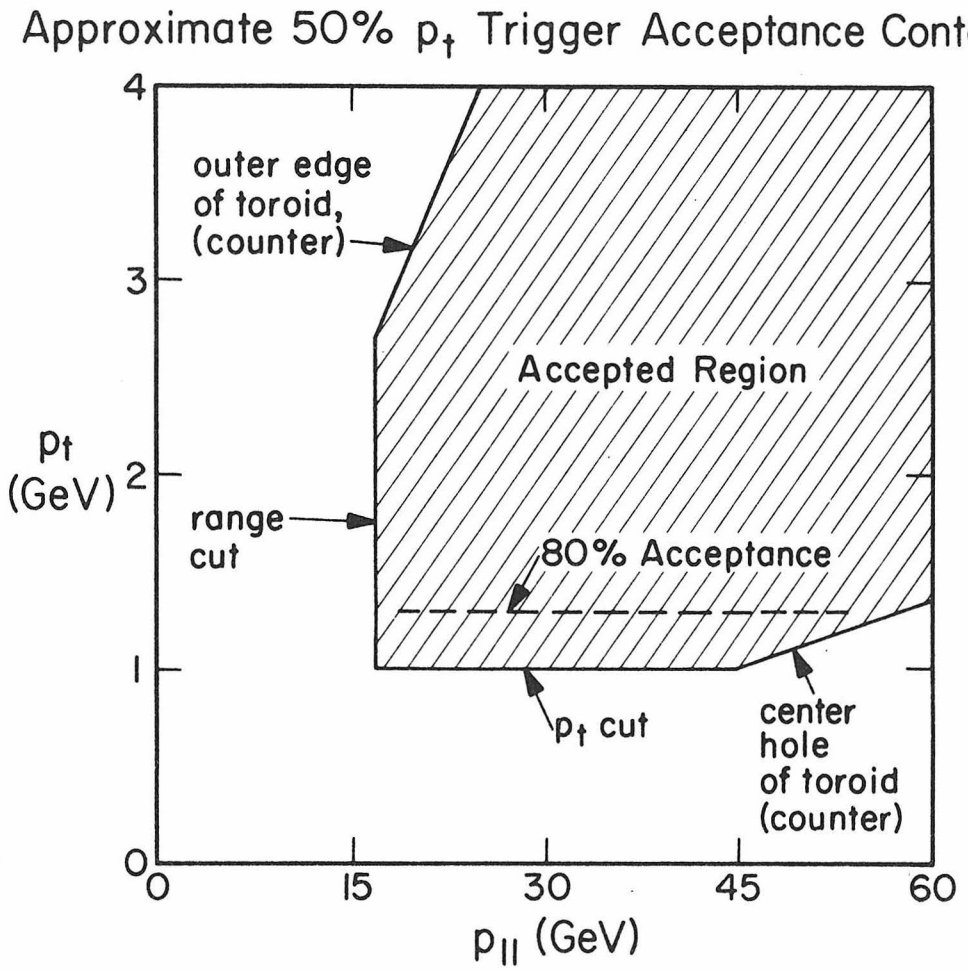

Figure 4-3:

Accepted region of p_t trigger for single positive muons as a function of laboratory parallel and transverse momenta. The solid lines indicate an approximate contour of 50% acceptance. The cutoffs for the toroidal magnet central hole and outer radius are provided by counters on the front face of the magnet.

the ψ as measured in the ψ rest frame. Here P_t refers to the total transverse momentum of the muon pair, and not an individual muon (p_t), while x_F is the fractional parallel momentum of the ψ in the center of mass ($x_F = p_z/p_z^{max}$). The p_t spectrum of the positive muons produced from 25,000 ψ decays simulated according to this distribution is shown in figure 4-4. If we fold this spectrum with the trigger acceptance, we obtain the result that .430 ± .003 of these events satisfy the p_t trigger. The two acrylic quadrant abstraction cut reduces this fraction to .302 ± .003.

F. Monte Carlo Characteristics and Efficiency Definition

Although it is possible to define the acceptance of the trigger and reconstruction efficiency as a function of the three variables x_F, P_t, and $\cos\theta^*$, in practice it was difficult to obtain sufficient statistics in the Monte Carlo program to do this. Instead, the efficiency was integrated over two of the three variables assuming production distributions in these variables similar to those actually observed in the data, and the process was repeated (see section C) until convergence was obtained. As the efficiencies were slowly varying, the errors in the resulting functions ε_{x_F}, ε_{P_t}, and $\varepsilon_{\cos\theta^*}$ due to systematics in use of inexact production parameters were small compared to the statistical errors in the efficiencies.

In general, the efficiencies utilized in calculating distributions were the product of several factors: trigger acceptance, reconstruction efficiency, mass cut efficiency, and smearing factors. The mass cut inefficiency resulted from the fact that the finite resolution of the spectrometer moved the mass of some reconstructed ψ events outside of

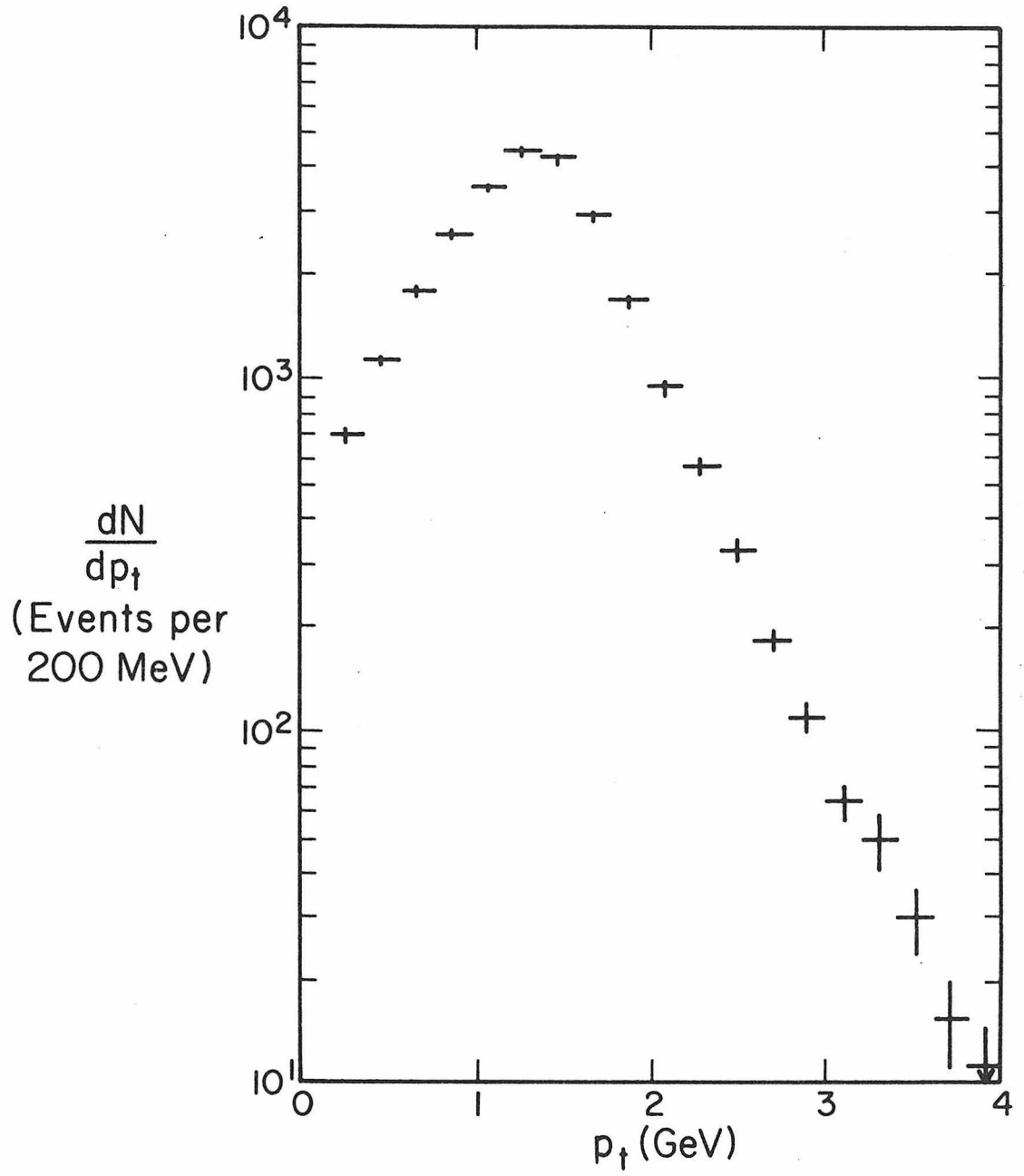

Figure 4-4:

Calculated transverse momentum (p_t) distribution of positive muons from ψ decays. The assumed ψ production distribution is given in the text.

the 2.4 to 4.0 GeV region defined as the ψ in this analysis. This same resolution problem also shifted the reconstructed values of dynamical parameters away from their actual values.

The effects of this smearing can be included in the efficiency by the following general formalism. If $O(\alpha_{obs})$ is the observed distribution in some observed value of a parameter α, and $P(\alpha_{act})$ is the true physical distribution in terms of the actual value of the parameter, then $O(\alpha_{obs}) = \int P(\alpha_{act})\ S(\alpha_{act},\alpha_{obs})\ d\alpha_{act}$, where $S(\alpha_{act},\alpha_{obs})$ is the probability that an event of true value α_{act} will be triggered on, reconstructed at a value α_{obs}, and have a reconstructed mass between 2.4 and 4.0 GeV. Again it is in principle possible to calculate $S(\alpha_{act},\alpha_{obs})$ by reconstruction of a large number of Monte Carlo events, but it proved reasonable only to assume a function $P(\alpha_{act})$ close to the physically measured distribution and then to define $\varepsilon_{\alpha}(\alpha)$ as $O(\alpha)/P(\alpha)$, iterating as necessary until ε converged. In the language of linear algebra this corresponds to solving the following problem: given an equation $O = SP$ for a known operator S and a particular choice of vector P, we define ε as that operator which satisfies $O = SP = \varepsilon P$ and is diagonal in a basis whose elements are characterized by the parameter α.

G. Efficiency Results

The efficiencies in x_F, P_t of the ψ, and $\cos\theta^*$ were calculated with a single Monte Carlo run in which 25,000 ψ events were generated according to the distribution described in section E. Of these events, 10741 satisfied the p_t trigger requirement, 7549 with the hits in two quadrants of the toroid acrylic counters. Figure 4-5 shows the mass dis-

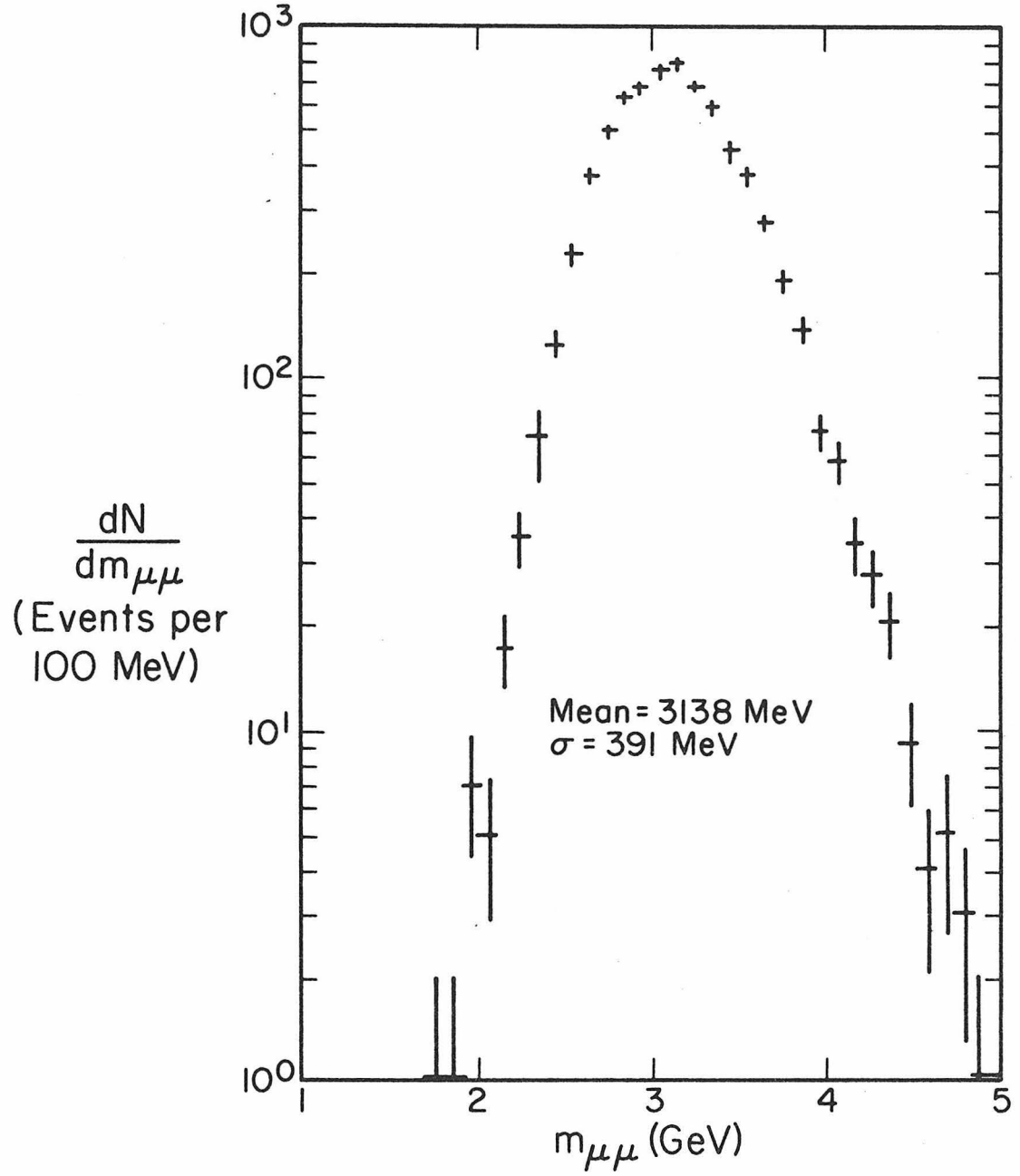

Figure 4-5:

Invariant mass ($m_{\mu\mu}$) distribution of 6991 reconstructed Monte Carlo ψ events.

tribution of the 6991 Monte Carlo events which were successfully reconstructed. Most of the 558 remaining events contained negative muons of such low energy that they stopped in the spectrometer magnet without leaving a track of length sufficient to reconstruct their momenta. Because of the resolution of the apparatus, with a standard deviation of 13%, only 6684 of the reconstructed events fell within the mass region from 2.4 to 4.0 GeV. The distribution indicates the actual effect of smearing on the invariant mass ($m_{\mu\mu}$) of a muon pair.

Figures 4-6 to 4-8 present the trigger with two acrylic quadrant requirement acceptance as functions of the actual (physical) variables x_F, P_t and $\cos\theta^*$ respectively. Note that although the experiment was triggered only on muons of $p_t \gtrsim 1$ GeV, the acceptance as a function of ψ P_t was relatively flat from 0 to 4 GeV. The final differential efficiencies as functions of the measured variables are shown in figures 4-9 to 4-11. The quotients of these sets of plots, figures 4-12 to 4-14, represent the distortions (D) of the measured distributions due to the combined effects of smearing, mass cut efficiency, and reconstruction efficiency.

Figures 4-6 to 4-8:

Probabilities (ε_{trig}) that a ψ will be triggered on and meet the two quadrant abstraction cut as a function of the physical (i.e. non-smeared) values of the parameters x_F, P_t, and $\cos\theta^*$. For each

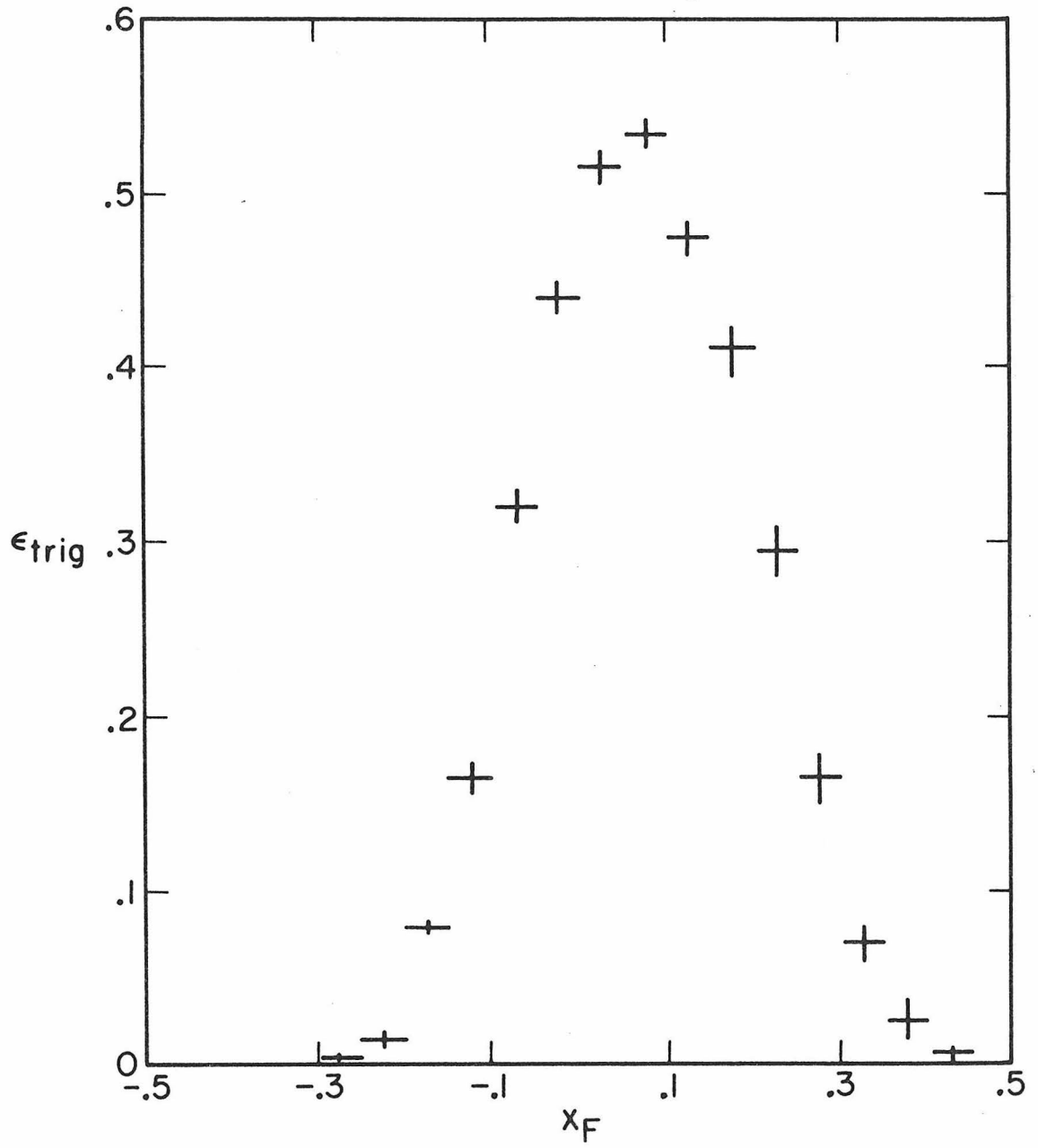

Figure 4-6

plot, the values of the remaining two parameters are integrated over the distribution described in section E of the text.

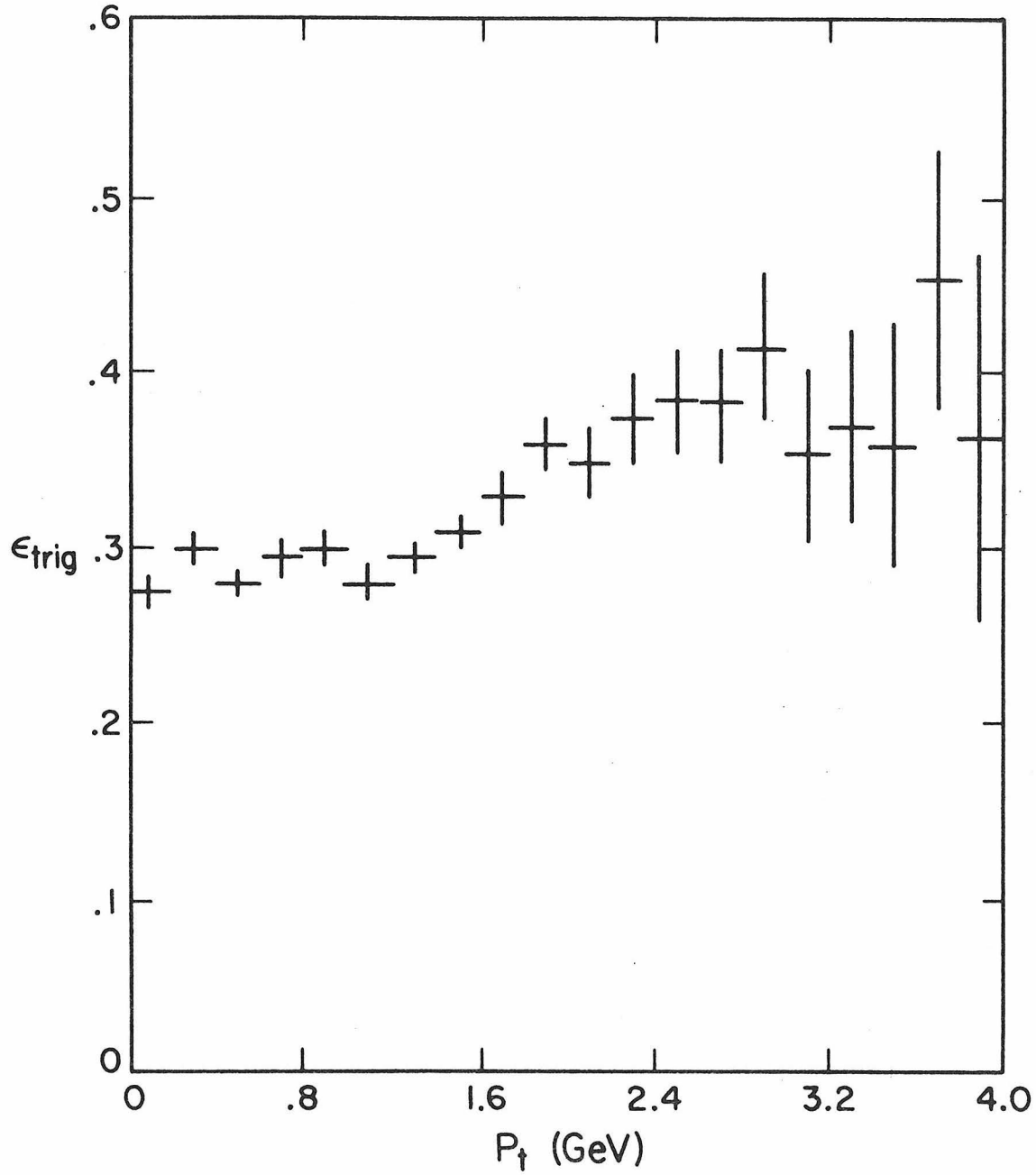

Figure 4-7

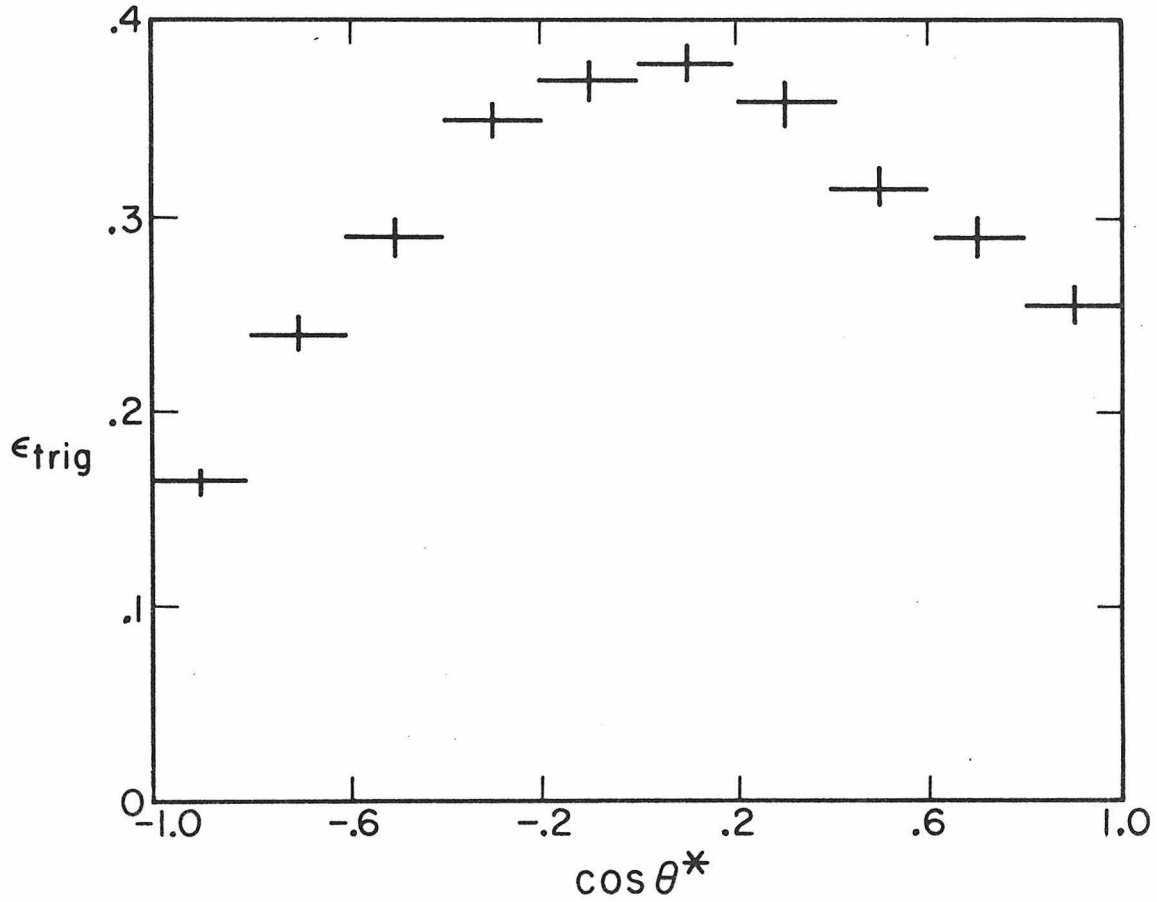

Figure 4-8

Figures 4-9 to 4-11:

Experimental efficiencies (ε) as functions of the reconstructed values of the parameters x_F, P_t, and $\cos\theta^*$. Effects of trigger

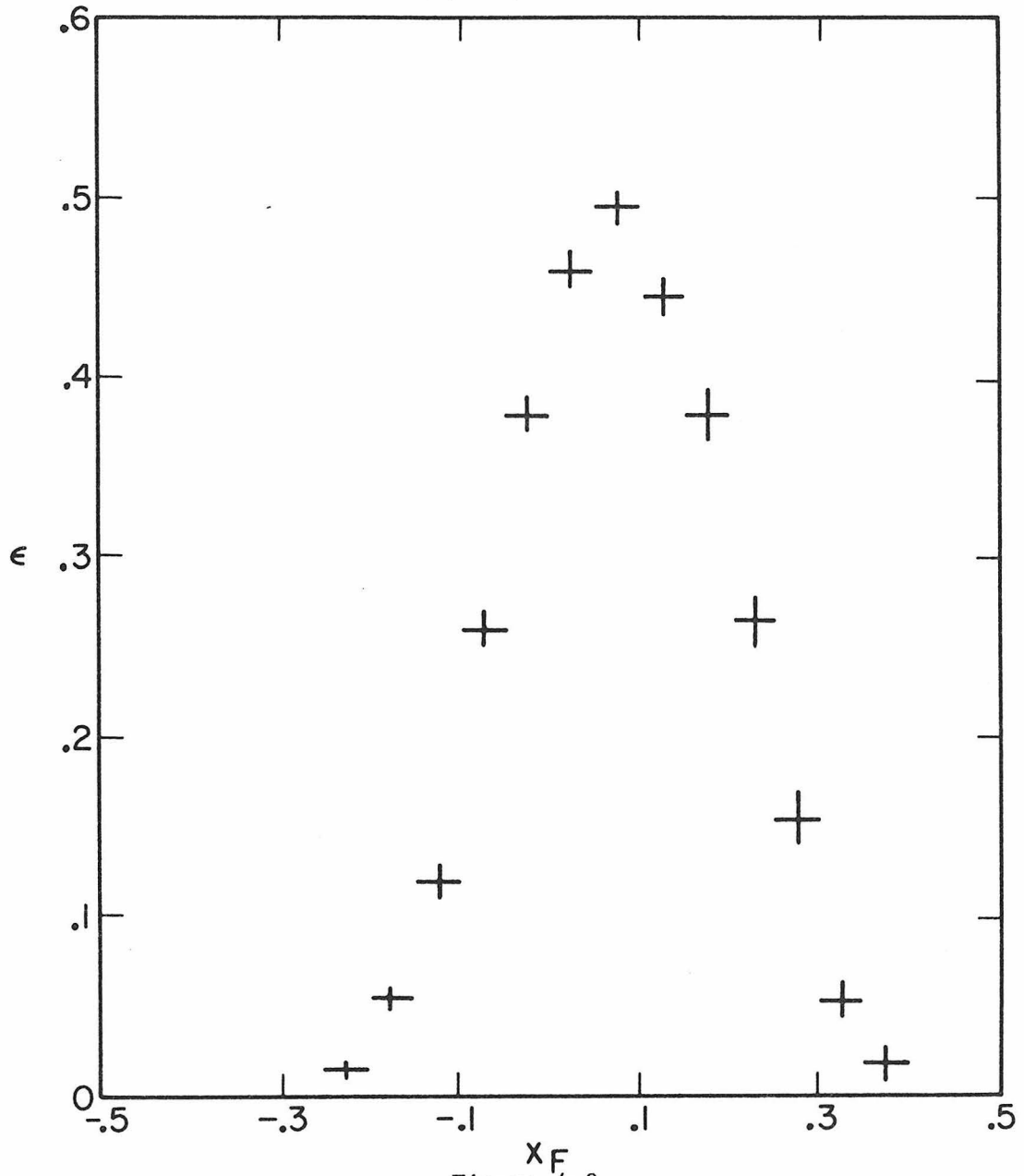

Figure 4-9

and reconstruction efficiency as well as smearing effects on the measured parameters and muon pair mass have been included.

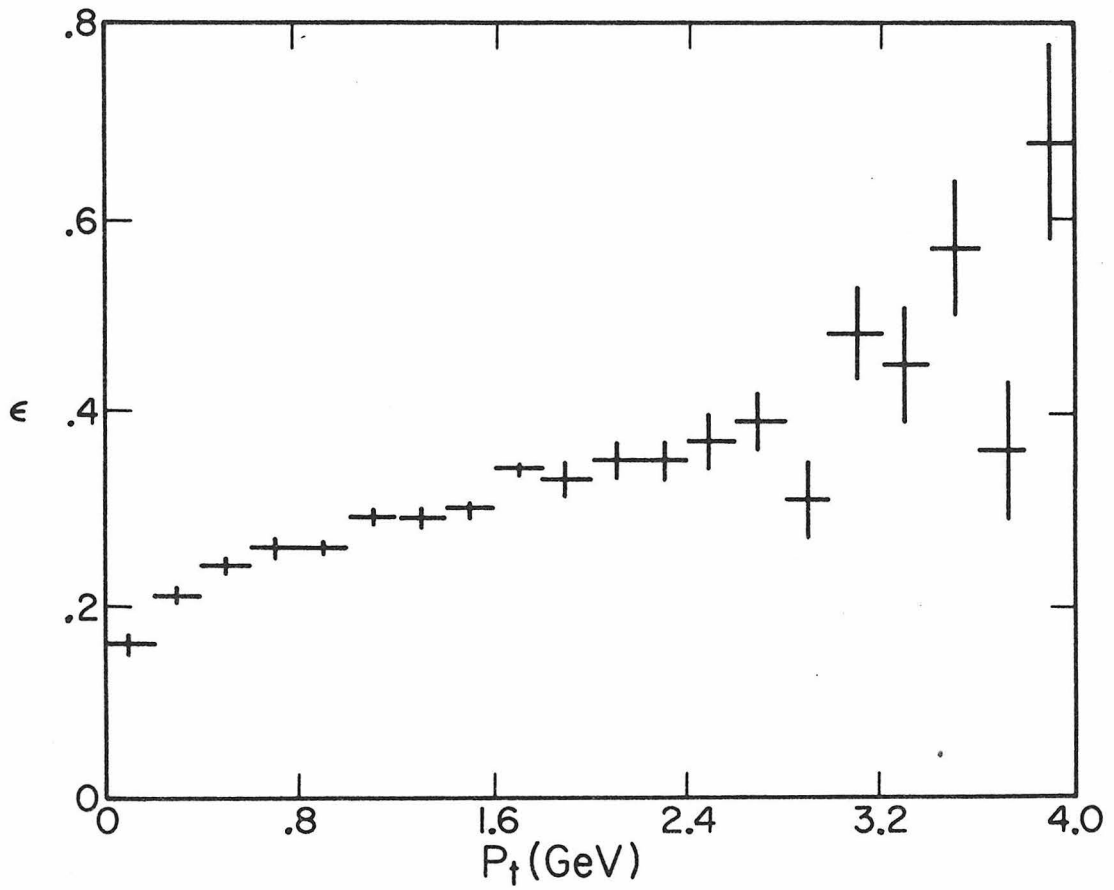

Figure 4-10

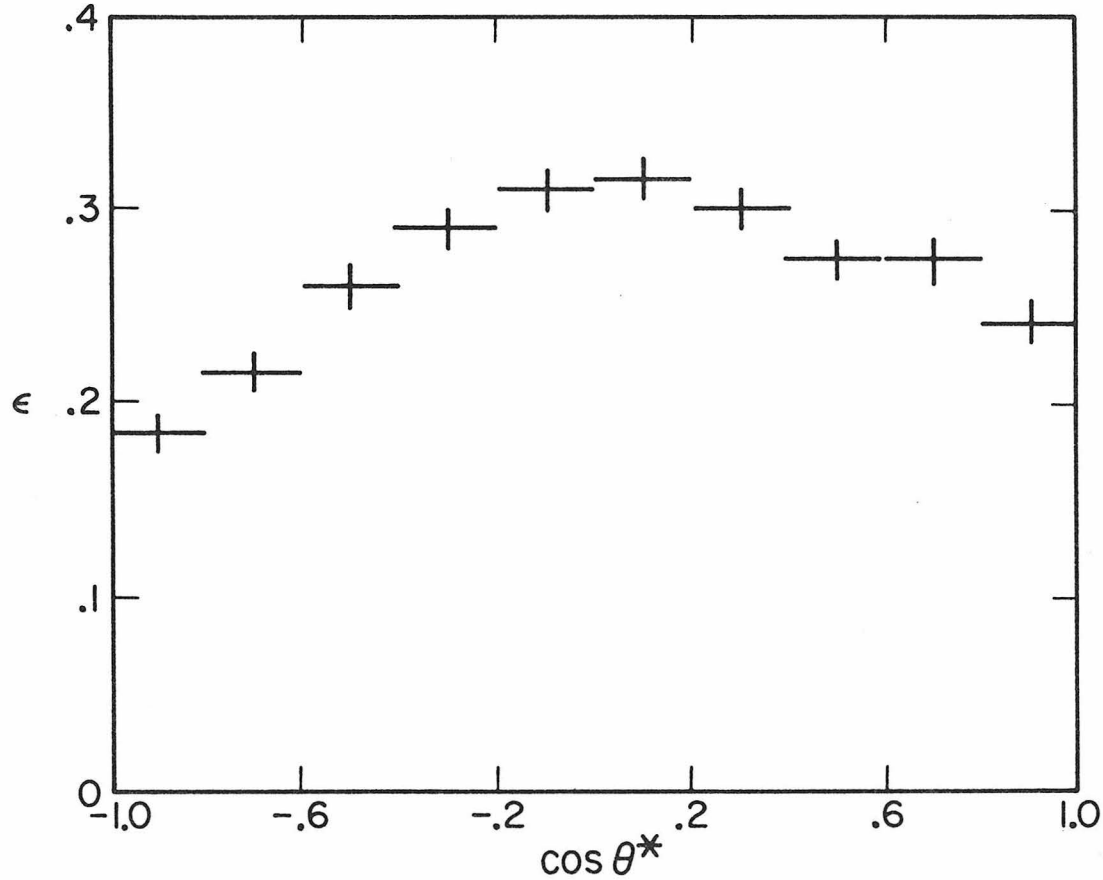

Figure 4-11

Figures 4-12 to 4-14:

Distortion factors (D) representing effects of reconstruction efficiency, smearing, and muon pair mass cuts as functions of

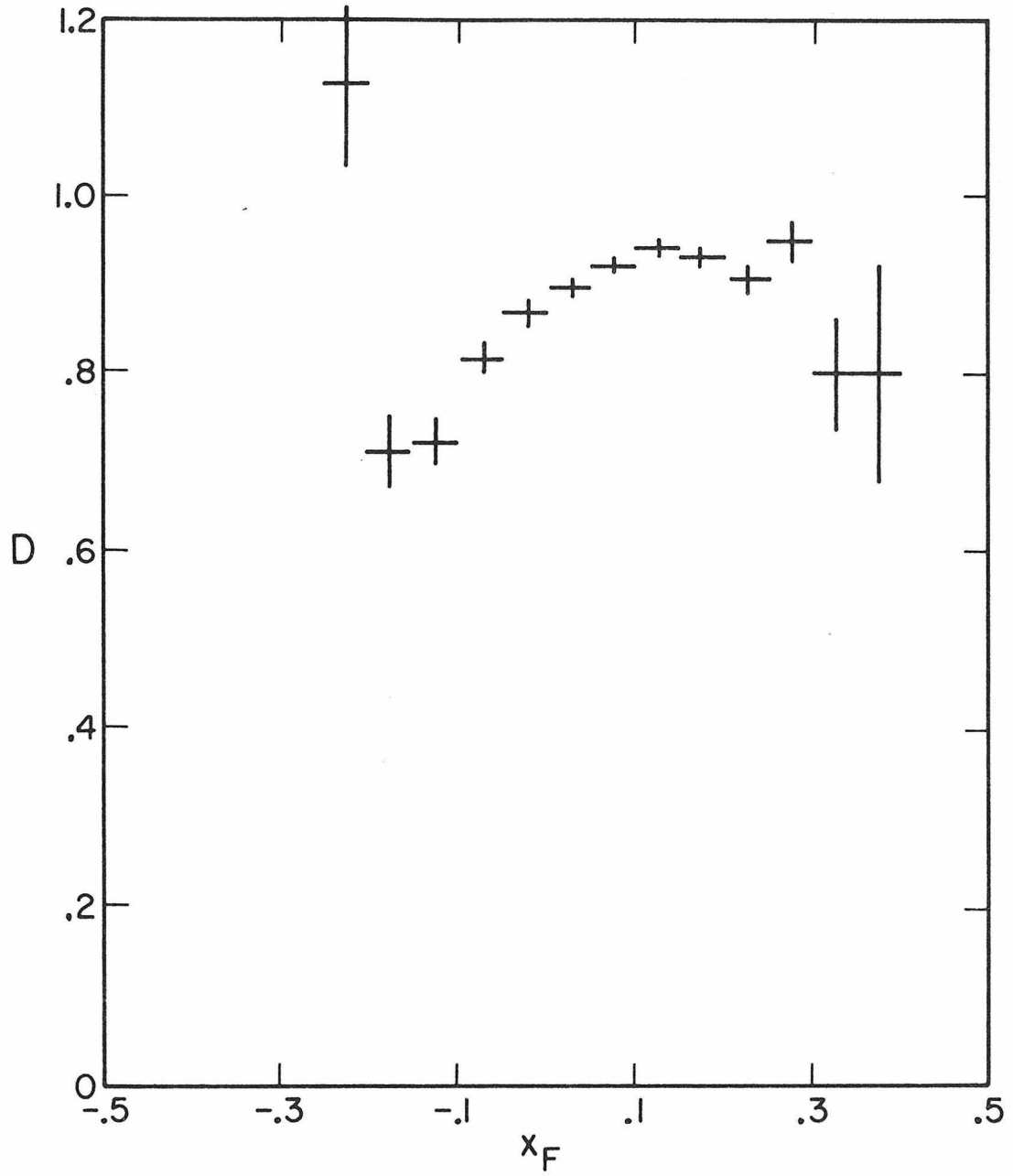

Figure 4-12

x_F, P_t, and cosθ*. The D factors are the ratios of experimental efficiency (figures 4-9 to 4-11) to trigger efficiency (figures 4-6 to 4-8).

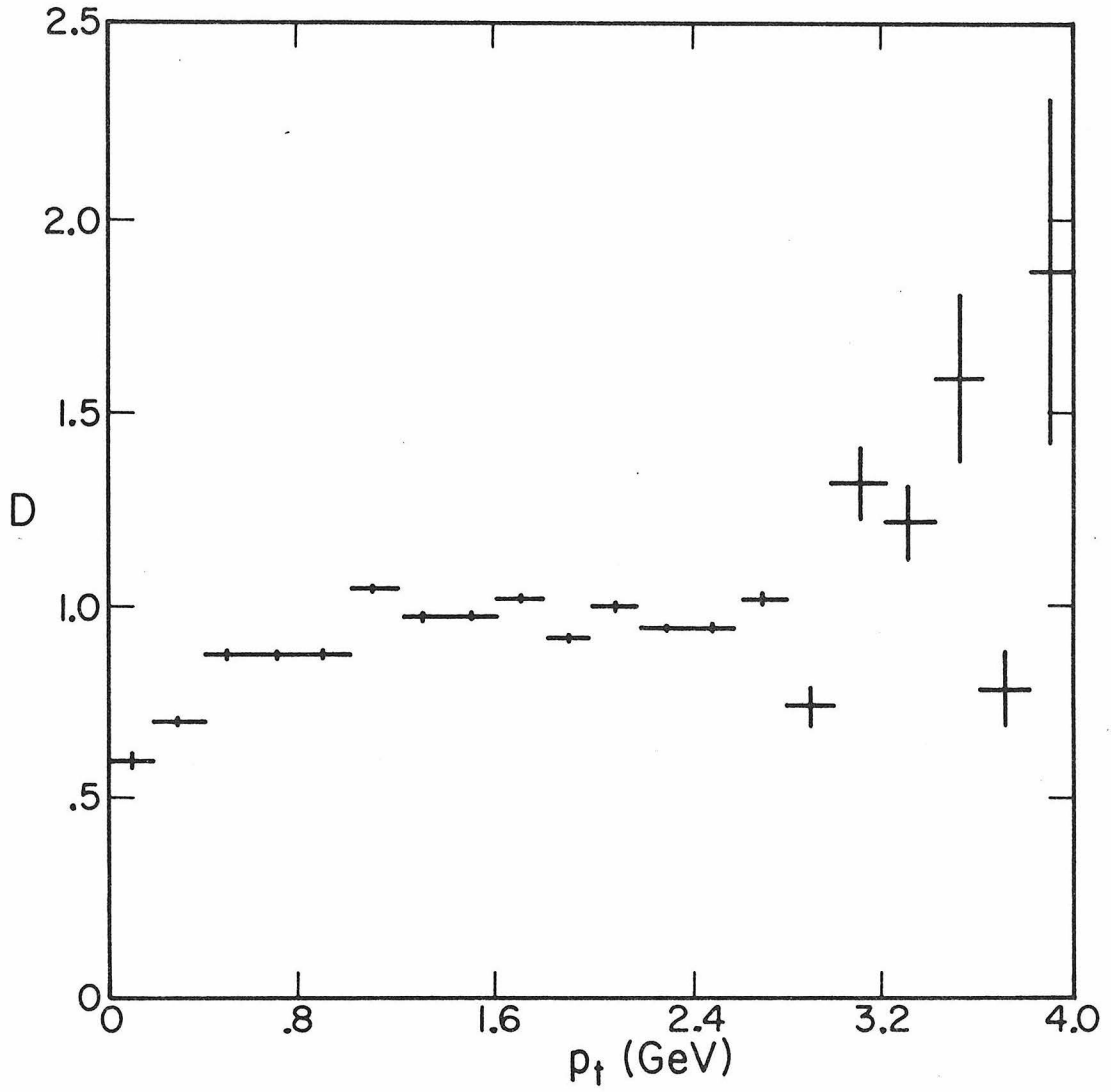

Figure 4-13

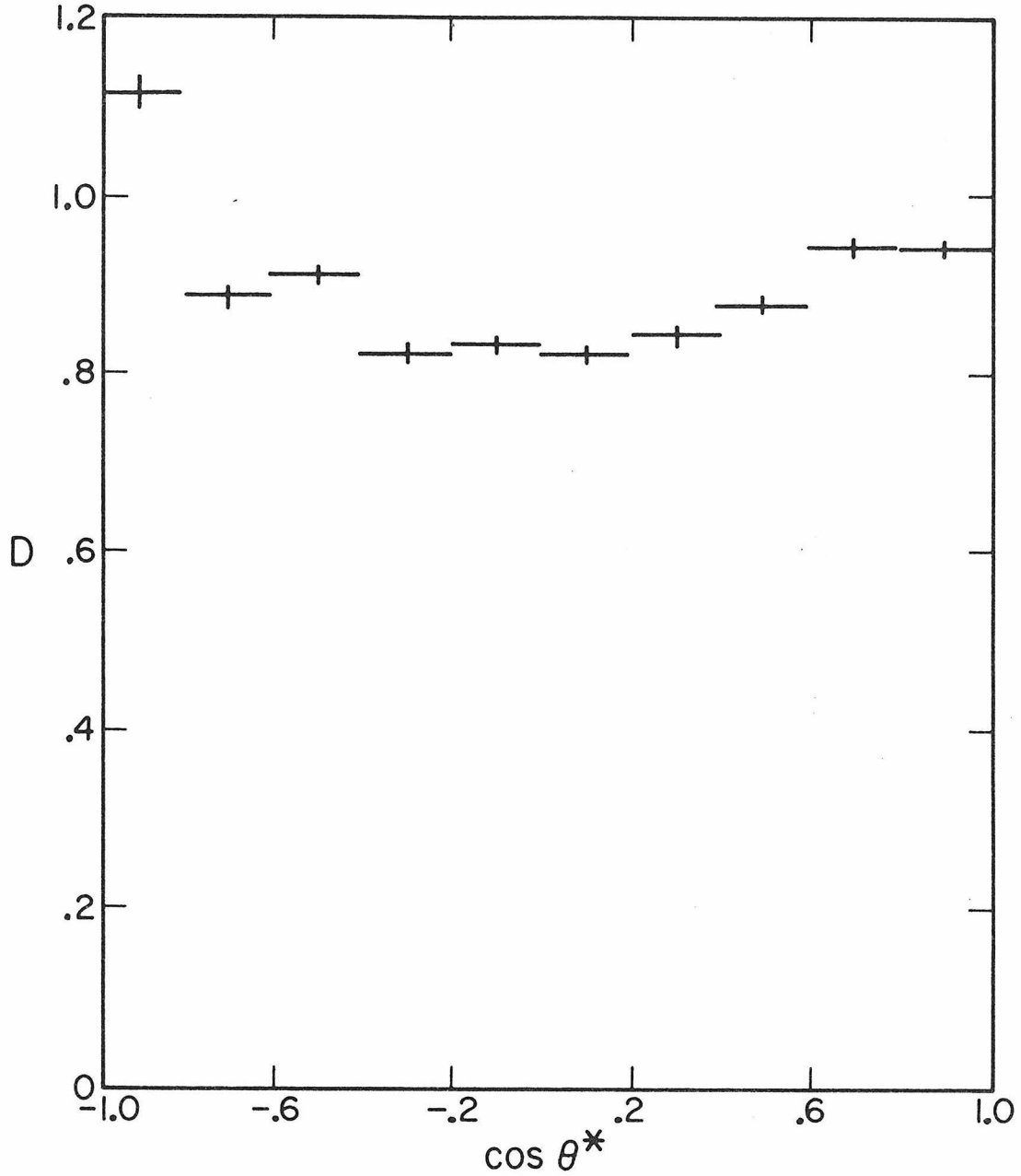

Figure 4-14

REFERENCE

4-1 J. G. Branson et al., Phys. Rev. Lett. 38, 1331, (1977).

CHAPTER V

DATA, BACKGROUNDS, AND NORMALIZATION

A. Overview

The mass spectrum of 35300 events in which the momenta of one positive and one negative muon were reconstructed is shown in figure 5-1. No cuts other than the p_t trigger on the positive muon (see section B of chapter IV) and the software pre-analysis abstraction cut selecting two muons of large opening angle by requiring hits in two quadrants of the acrylic counters (see section B of chapter III) have been imposed. In addition, no correction for the variation of acceptance with muon pair mass has been applied. The ψ peak is clearly visible sitting on a falling dimuon background, presumably arising from tails of low mass vector mesons (e.g. ρ, ω, etc.) decaying to two muons and from a non-resonant dimuon continuum (possibly Drell-Yan[1] electromagnetic pairs). The apparatus lacks the resolution necessary to distinguish the $\psi(3685)$ resonance.

The cut-off in the data at low mass is due to the apparatus acceptance, especially with the two acrylic quadrant requirement which was imposed precisely to reduce acceptance for low mass pairs. If we assume that the two acrylic quadrant cut biases the acceptance towards the region of symmetric (i.e. 90° in the center of mass) decays, and recall that the p_t trigger becomes efficient at about 1 GeV of transverse momentum, we can estimate that the acceptance would fall rapidly for muon pair masses below 2 GeV. The effect of this cut may be gauged by noting that the observed signal in the vicinity of the ρ is only about one order of magnitude larger than it is at the ψ, while the expected production differs by two to three orders of magnitude[2].

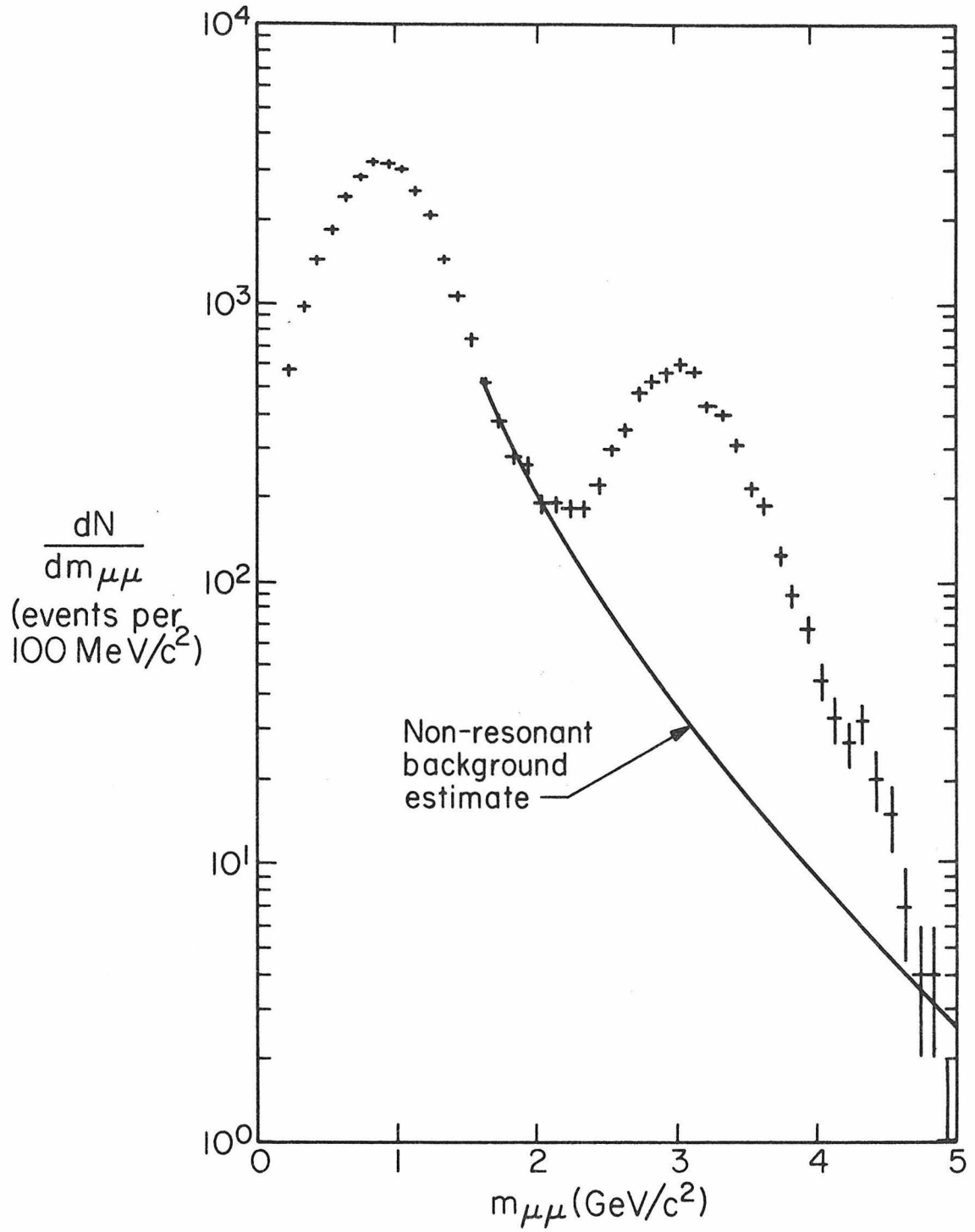

Figure 5-1:

Raw invariant mass ($m_{\mu\mu}$) distribution of opposite sign muon pairs. The curve represents the best estimate of the non-resonant continuum contribution.

Interpreting the ψ production data and extracting both normalized cross sections and differential distributions requires correcting the data for two effects: (1) non-resonant production in the ψ mass region and (2) ψ production in the collisions of secondary particles created during the hadronic shower in the thick target. These corrections, the flux normalization, and the resulting differential distributions are presented in the remainder of this chapter, while cross section results are detailed at the beginning of chapter VI.

B. Non ψ Background Subtraction

The non ψ background resulted from continuum dimuon pairs with a possible small contribution from the tail of the ρ and other low mass vector mesons. A background shape was suggested by an extension of Drell-Yan scaling[3], which purports that $\left.\frac{M^3 d^2\sigma}{dM\ dy}\right|_{y=0}$ is a function only of the dimensionless variable $\sqrt{\tau} = M/\sqrt{s}$. Here M is the invariant mass of a muon pair, y is the center of mass rapidity of the pair, and s is the total center of mass energy squared. Noting that both the cross section and the experimental efficiency peak near y of 0, it was assumed that the raw mass distribution could be described similarly, i.e. by assuming that $\frac{d\sigma}{dM} \propto \frac{1}{M^3} f(\sqrt{\tau})$, where $f(\sqrt{\tau}) = e^{-14.9\sqrt{\tau}}$ is the observed form of the y=0 scaling function[4], and by further neglecting the effects of mass resolution and the dependence of acceptance upon pair mass. Note that over the 2.4 to 4.0 GeV ψ mass region $f(\sqrt{\tau})$ changes by only about half as much as the M^3 factor, and that therefore the background contribution is relatively insensitive to the exact form of the parameterization of the continuum distribution. In essence, the

Drell-Yan form of the background is used only because it provides a convenient estimate of the shape, and not because of any assumption that the background is dominated by the Drell-Yan process.

The normalization of the background was calculated by the following method: the continuum contribution was estimated at 30 events per 100 MeV at 3.1 GeV, thus leaving a signal of 560 events per 100 MeV. The ψ was assumed to have a Gaussian shape centered at 3.1 GeV with this height and with width 400 MeV, thus predicting a signal of 180 events per 100 MeV at 2.5 GeV. Comparison with the observed signal plus background of 265 events indicated that a background contribution of 85 events per 100 MeV at 2.5 GeV was a reasonable estimate.

The appropriate curve for the non-resonant background is also shown in figure 5-1, and corresponds to $\frac{M^3 dN}{dM} = 51700\ e^{-14.9\sqrt{\tau}}$ events GeV^2. The continuum contribution in the 2.4 to 4.0 GeV mass region was 578 of the 5443 observed events, corresponding to a correction for resonant production of .894 ± .004. The .4% error quoted reflects only statistics. The systematic error in the overall normalization of the background may be estimated by noting that the continuum distribution agrees with the observed data in the 2 GeV region to better than 10%. Assuming then a systematic error estimate of 10% of the estimated background increases the error to .011.

C. Secondary Production Background

The contribution to the observed ψ signal due to ψ production by secondary particles produced in the 400 GeV hadron shower was calculated by a Monte Carlo procedure. The x_F dependence of the cross

section for inclusive proton production in 400 GeV proton-proton interactions was determined by integration of the invariant cross section as parameterized by Taylor et al.,[5]. The shape of this cross section versus x_F was assumed, but the normalization was adjusted to correspond to the production of one nucleon in the forward hemisphere per collision.

The effects of the heavy Fe nucleus were included by assuming that $\frac{d\sigma}{dx_F}$ (p + nucleus → p + anything)/$\frac{d\sigma}{dx_F}$ (p + p → p + anything) $\propto A^{-.25x_F}$[6], where A is the atomic weight of the nucleus (56 for Fe). Given the form of $\frac{d\sigma}{dx_F}$ (p-p) normalized to unit integral, we can calculate the mean number of forward nucleons per collision on Fe as $\int_0^1 A^{-.25x_F} \frac{d\sigma}{dx_F}$ (p-p) dx_F, or .72 nucleons per collision. The functional form $A^{-.25x_F}$ breaks down for values of x_F near zero[7], and in fact the remaining .28 nucleons per collision necessary to conserve baryon number may be found at very small x_F, where because of their greatly reduced efficiency for producing ψ's, their effects may be safely ignored.

Finally, the probability of producing a ψ using a lower energy incident nucleon was taken as being proportional to $e^{-10.8\sqrt{\tau}}$[8]. If we normalize this probability to unity for 400 GeV nucleons, then the average value of the excitation probability for secondary nucleons from 400 GeV primary interactions is .32. This figure, coupled with the .72 secondaries per primary, gave a probability of a secondary nucleon producing a ψ of 23% of the probability that a ψ was produced in the primary 400 GeV proton interaction.

The efficiency for observing these events was then calculated by a Monte Carlo generation of a tape of simulated events from secondaries with an energy distribution given by the probability of secondary nucleon production multiplied by the probability of ψ excitation. The

production dynamics were assumed to be independent of center of mass energy and were identical to those used in calculation of primary acceptance. The reconstruction efficiency for secondary events was 70% of that for primary events.

This entire procedure was repeated for production by tertiary nucleons with the additional assumption that the shape of $\frac{d\sigma}{dx_F}$ is independent of the energy of the interacting nucleon. The mean excitation for tertiaries was 8.0%, which when coupled with a mean of $.72^2$ tertiaries per primary gives a probability for production by tertiaries of 4.1% of that for primaries. In addition, the reconstruction efficiency for tertiary ψ's was 45% of that for primary ψ's.

Combining production by secondaries and tertiaries one obtains the result that 84.9% of observed events were produced by primaries. The systematic errors in this quantity arise from uncertainties in the measurements of $\frac{d\sigma}{dx_F}$ for proton-proton scattering, in the $A^{-.25x_F}$ effect of the heavy nucleus, and in the $e^{-10.8\sqrt{\tau}}$ shape of the excitation curve. Using the published errors for the p-p scattering and assuming 20% errors in the latter two effects, the resulting errors of 15% on the secondary contribution and 30% for the tertiary contribution were obtained. These errors were included in the subsequent bin-wise subtractions of the Monte Carlo estimates of secondary production in the differential distributions.

The effects of production by secondary pions were not included in these calculations. Instead, it was noted that inclusive pion production in proton-proton interactions is only of order one percent of nucleon production near x_F of .5, where most of the calculated ψ's

from secondary production were observed, and does not reach 10% of nucleon production until x_F of .3.

D. Normalization

The total data sample observed resulted from an exposure of 1.429×10^{10} protons meeting the IBV requirement (see section I of chapter II) during experiment live time. A correction due to hardware failure in the readout system for the upstream spark chambers resulting in loss of all spark information for some events during $\sim 5\%$ of the run reduced this flux to $1.40 \pm .03 \times 10^{10}$. This number must then be corrected by a factor of .985 to account for events discarded for CD chamber readout status errors and overflow (section 1 of appendix B) and a factor of .990 for MTD readout status errors (section 2 of appendix B).

Although the calculated efficiencies include the effects of track reconstruction efficiency (see section F of chapter IV) assuming all spark chambers fired, an additional correction was necessary to account for the low (85%) efficiency of the first module of upstream chambers. If ε is the mean chamber efficiency, then the probability of sufficient chambers firing to reconstruct a single track is approximately given by $(\varepsilon^4 + 4\varepsilon^3(1 - \varepsilon))^2 + 12\varepsilon^2(1 - \varepsilon)^2(\varepsilon^4 + 4\varepsilon^3(1 - \varepsilon))$. The correction for chamber efficiency for two tracks is estimated to be $.935 \pm .020$.

The above corrections bring the effective flux to $1.29 \pm .04 \times 10^{10}$ protons. If the correction for non-resonant background (section B) is made, this increases to $1.43 \pm .05 \times 10^{10}$. If we use the value 690 millibarns[9] for the inelastic proton-iron cross section, this corre-

sponds to a single event cross section sensitivity of 48.3 ± 1.6 picobarns per Fe nucleus. Finally, assuming the nucleon number dependence of the ψ cross section is of the form $A^{.90 \pm .05}$[10], this sensitivity becomes 1.29 ± .26 picobarns per nucleon per event. This normalization should be applied to the differential distributions in the remainder of this chapter. Table 5-1 summarizes the normalization corrections. Note that the P_t distributions (section F) do not have an explicit subtraction for secondary production made, and thus the flux normalization used in these distributions must be divided by an additional factor of .849 ± .017.

E. x_F Distribution

The raw x_F distribution, corrected for efficiency but without any subtraction for production by secondaries, is shown in figure 5-2. The non-resonant background is assumed to have the same shape as the ψ. The reconstructed efficiency corrected spectra for events excited by simulated secondary and tertiary nucleons are shown in figures 5-3 and 5-4 respectively. Note that these distributions appear to peak at x_F near -.1 because in their reconstruction x_F was calculated in the center of mass of the primary interaction rather than that of the secondary interaction. The curve for secondaries should be scaled by a factor of .394 (1 ± .15) while that for tertiaries should be multiplied by .071 (1 ± .3) before subtraction from the data.

The data after correction for secondary production are shown in figure 5-5. A fit of $\frac{dN}{dx_F}$ to the form $(1 - |x_F|)^a$ gives a best fit value for a for the $x_F > 0$ data of 4.69 ± .30 (χ^2 = 6.7 for 6 degrees of

TABLE 5-1

CORRECTIONS TO FLUX OF 1.43×10^{10} PROTONS

1.	Hardware Failure	Subtract	$.03 \pm .03 \times 10^{10}$
2.	CD Chamber Readout System Status Errors	Multiply by	.985
3.	MTD System Readout Status Errors	Multiply by	.990
4.	Spark Chamber Inefficiency Correction	Multiply by	$.935 \pm .020$
5.	Non-Resonant Background Correction	Divide by	$.894 \pm .011$
6.	Secondary Production Background Correction*	Divide by	$.849 \pm .017$

*The secondary production background correction should be made only to the flux for the P_t distribution. In the x_F and $\cos\theta^*$ distributions the secondary contribution has been subtracted from each bin.

Note that although corrections 1-4 represent inefficiencies in the experiment (i.e. events which should have been observed, but were not), items 5 and 6 correspond to excess events in the observed data, and thus the corrections involved should be more properly applied by multiplying the data by the fraction of non-background events. The mathematically equivalent procedure of dividing the flux by the identical factor is used here for the sake of simplicity. All corrections are applied to the flux, rather than some to the flux and some to the number of observed events.

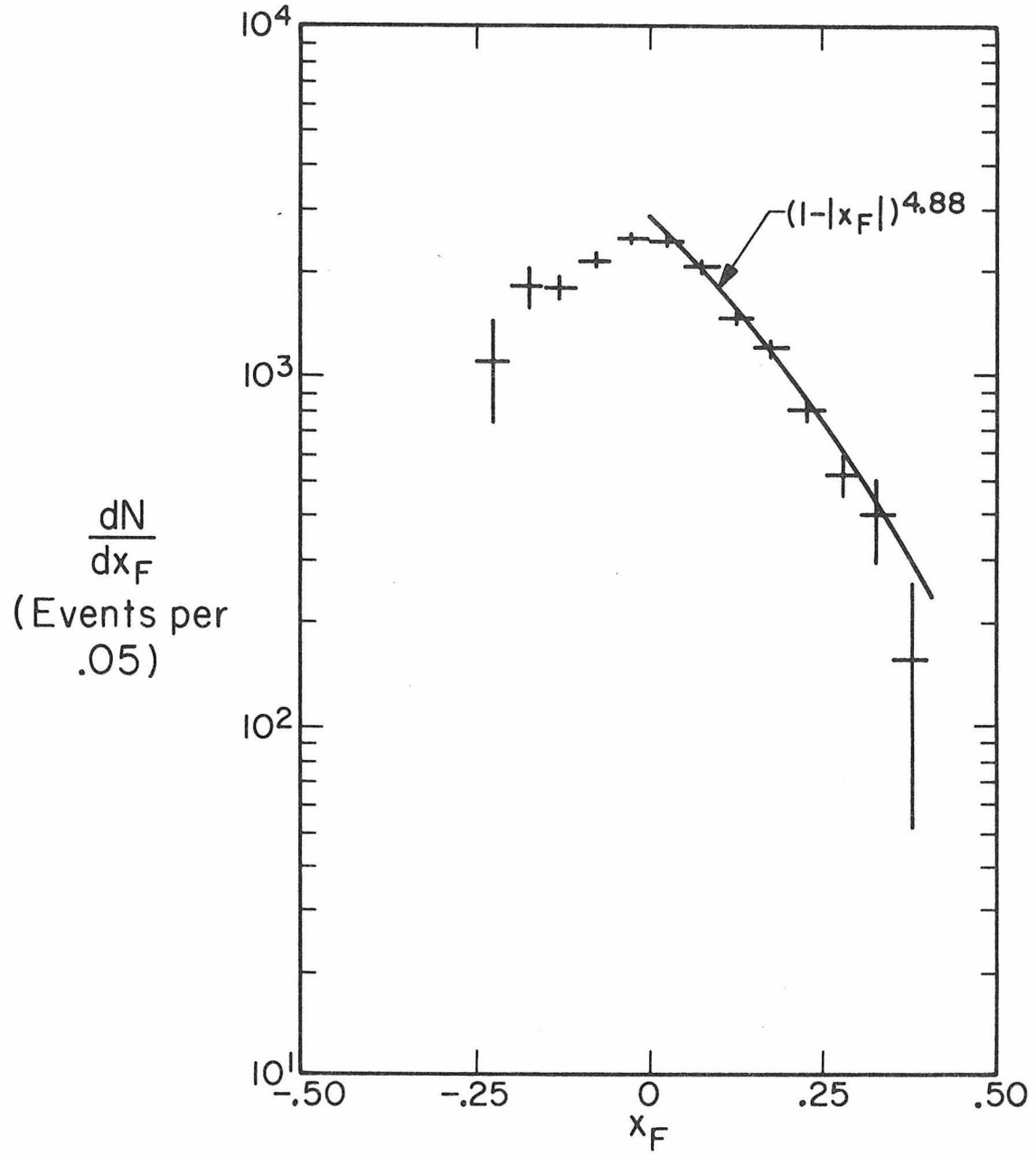

Figure 5-2:

The x_F distribution of ψ events. No subtraction for secondary production has been made. The non-resonant background under the ψ is assumed to have the same production dynamics as the ψ. The data have been corrected for acceptance (figure 4-9).

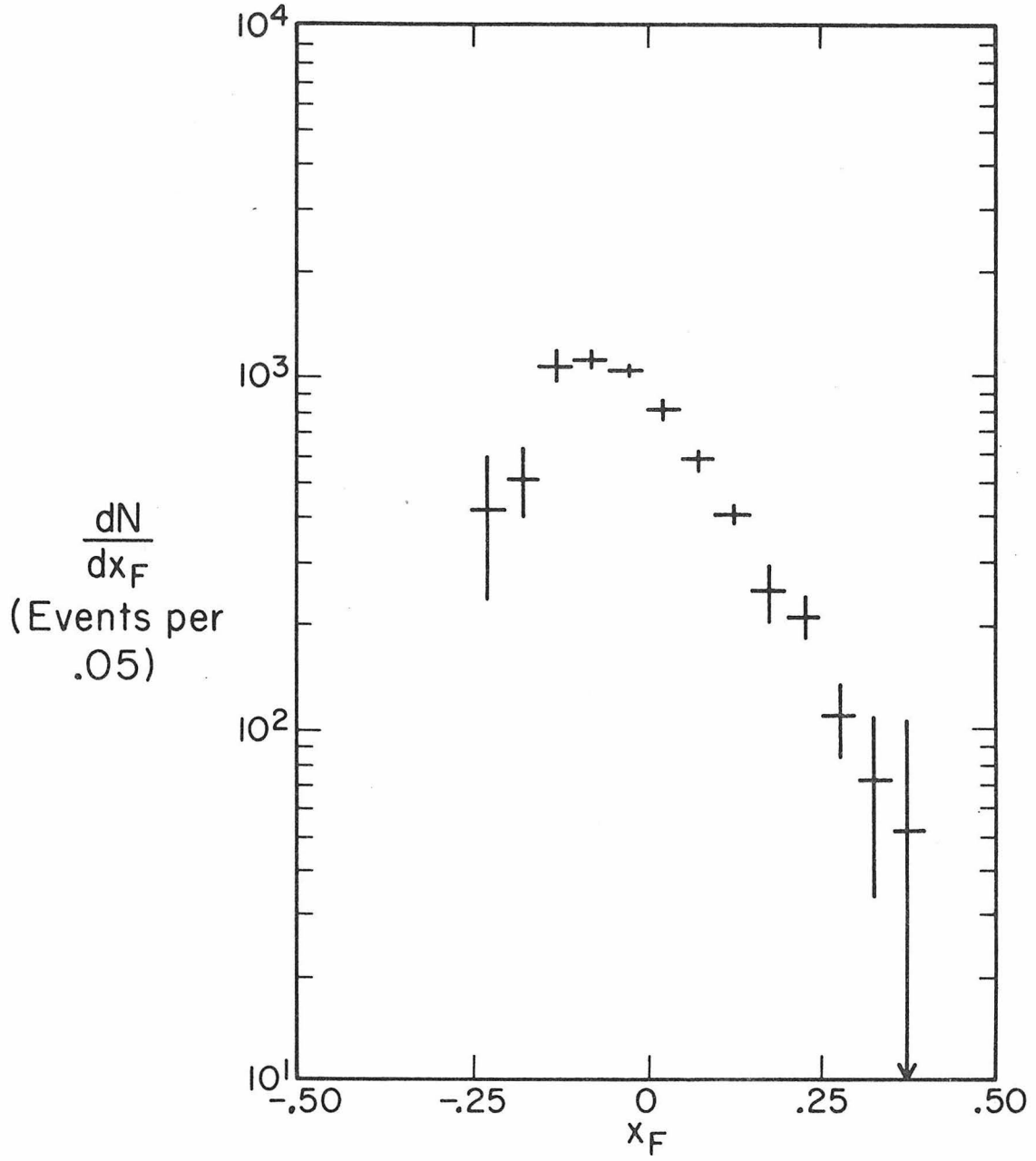

Figure 5-3:

The calculated reconstructed x_F distribution for secondary events. The data have been corrected for acceptance, but should be scaled by a factor of .394(1 ± .15) before subtraction for the observed distribution (figure 5-2).

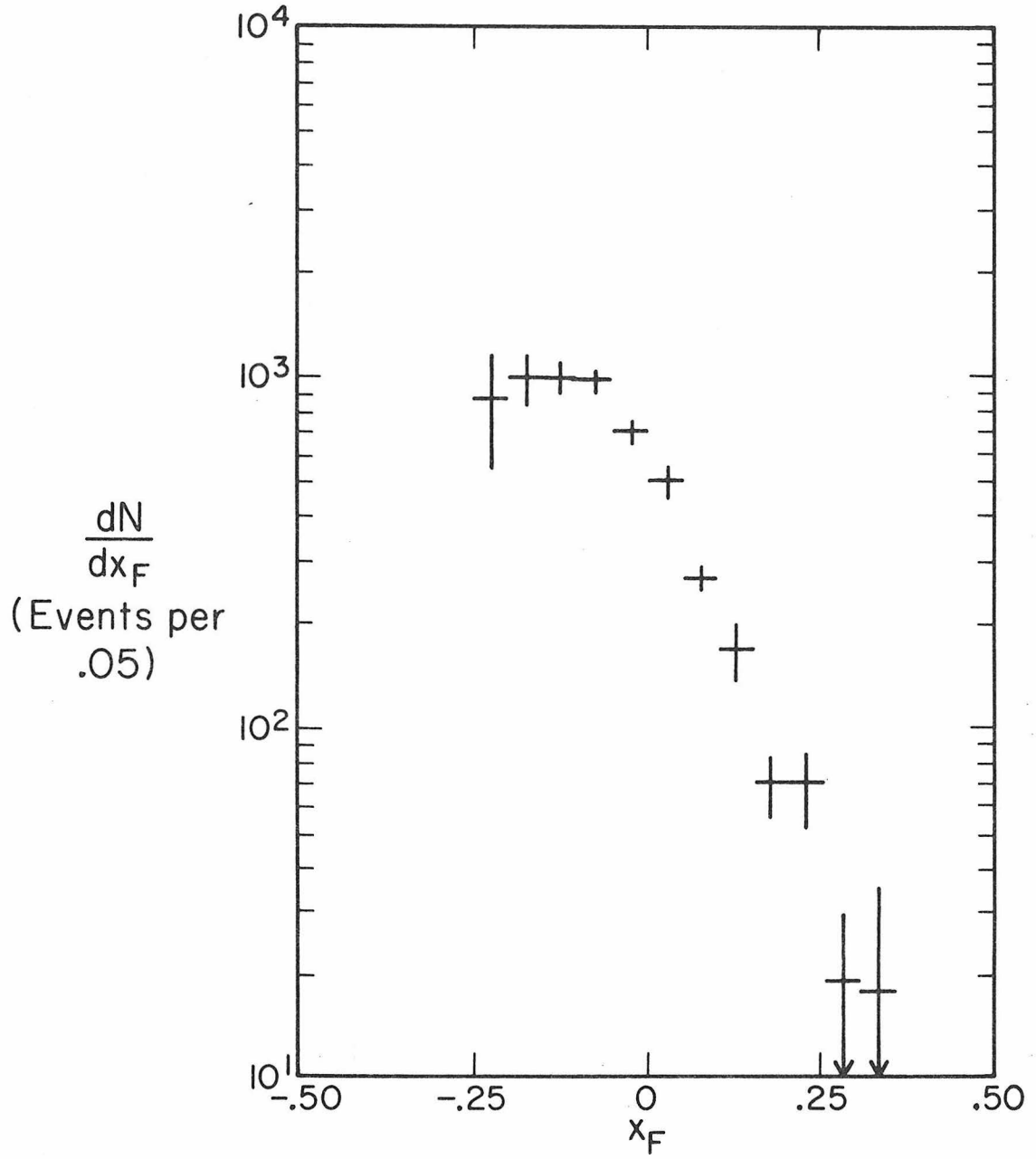

Figure 5-4:

The calculated reconstructed x_F distribution for tertiary events. The data have been corrected for acceptance, but should be scaled by a factor of .071(1 ± .3) before subtraction from the observed distribution (figure 5-2).

Figure 5-5:

The acceptance corrected x_F distribution of ψ events after subtraction of the calculated background from secondary and tertiary

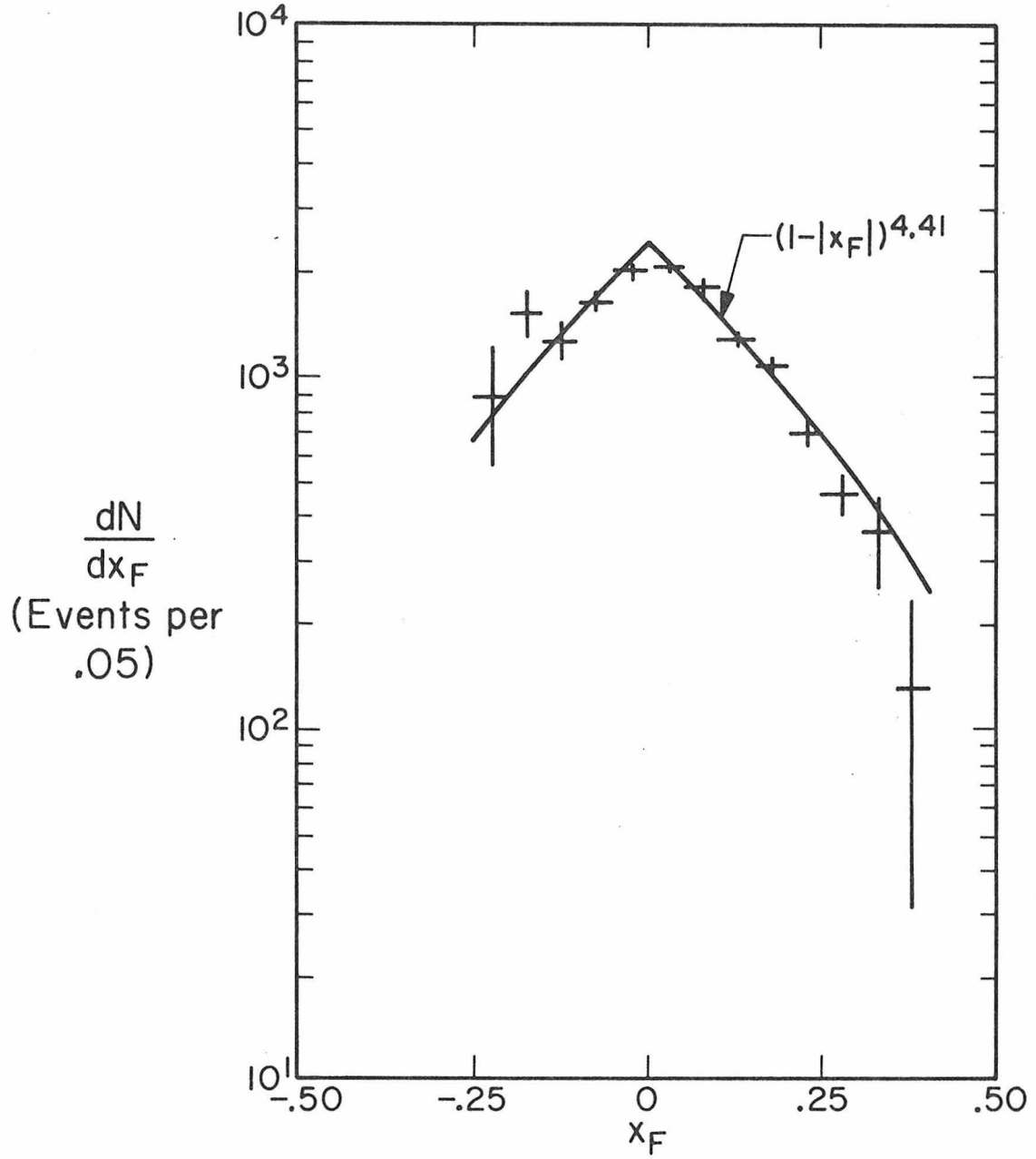

production. The curve represents a best fit to the form $(1 - |x_F|)^a$: $a = 4.41 \pm .27$ ($\chi^2 = 14.9$ for 11 D.F.). The normalization for ψ's (assuming that $.894 \pm .011$ of these events are ψ's and the remainder are non-resonant background with the same production distributions) is $1.29 \pm .26$ picobarns per nucleon per event.

freedom) after the subtraction compared to 4.88 ± .26 (χ^2 = 6.4 for 6 D.F.) before correction. The fit to the corrected data over all x_F gives an a of 4.41 ± .27 (χ^2 = 14.9 for 11 D.F.). Most of the additional χ^2 is due to the bin between -.20 and -.15; eliminating this bin from the fit yields a value of 4.51 ± .28 (χ^2 = 8.9 for 10 D.F.) for a.

Figure 5-6 presents the invariant x_F distribution $E\frac{dN}{dx_F}$ after the secondary subtraction is made. A fit to the form $(1 - |x_F|)^c$ gives a value for c of 3.20 ± .30 (χ^2 = 5.1 for 6 D.F.) for the $x_F > 0$ data and 2.96 ± .27 (χ^2 = 12.9 for 11. D.F.) for all x_F. Again, elimination of the -.20 to -.15 bin yields a better fit: 3.06 ± .28 (χ^2 = 6.9 for 10 D.F.).

F. P_t Distribution

The P_t distribution $\frac{1}{P_t}\frac{dN}{dP_t}$ is shown in figure 5-7. No secondary production subtraction has been made. The data are well fit by a single exponential for P_t above $\sim$1 GeV, but some curvature is evident at lower P_t. This low P_t region is precisely that regime in which the correction for smearing becomes important, with an average multiple scattering corresponding to P_t of 300 MeV. The phenomenon of curvature at low P_t is also evident in the 225 GeV data of Branson et al.[11], and may possibly be more prevalent in their data on tin than on carbon targets (i.e. the effect <u>may</u> be exaggerated by a heavy nucleus[12]).

A fit of $\frac{1}{P_t}\frac{dN}{dP_t}$ to the form e^{-bP_t} over the region of P_t from 1.2 to 4.0 GeV gives a best fit value for b of 2.23 ± .05 (χ^2 = 8.6 for 12 D.F.). Consideration of any additional points leads to a rapid

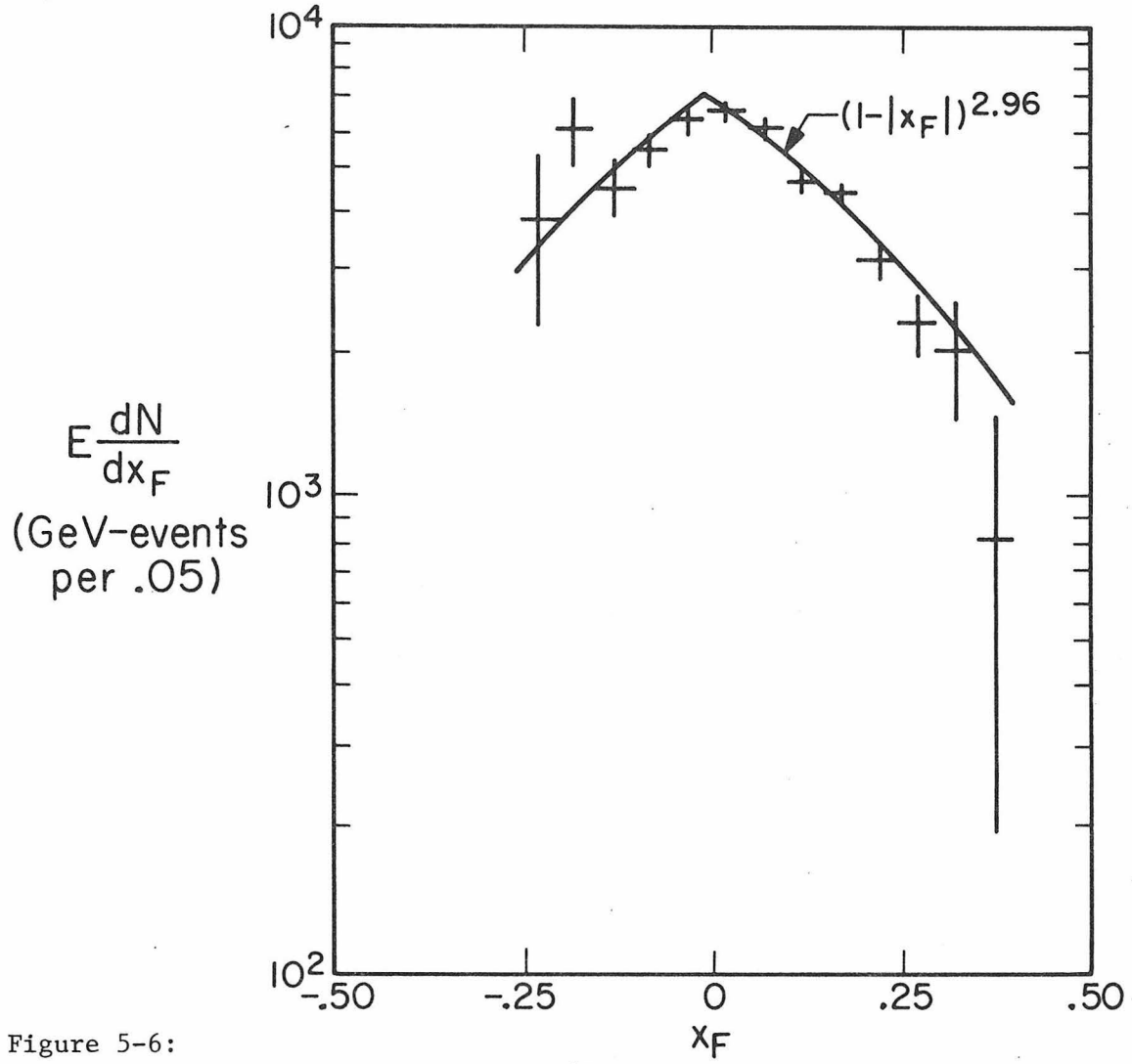

Figure 5-6:

The invariant x_F distribution $E\frac{dN}{dx_F}$ of ψ events after correction for acceptance and subtraction of calculated background from secondary and tertiary production. The curve represents the best fit to the form $(1 - |x_F|)^c$: $c = 2.96 \pm .27$ ($\chi^2 = 12.9$ for 11 D.F.). The normalization is $1.29 \pm .26$ picobarns per nucleon per event.

Figure 5-7:

The P_t spectrum $\frac{1}{P_t}\frac{dN}{dP_t}$ for ψ events, corrected for acceptance (figure 4-10). No subtraction for secondary and tertiary production has

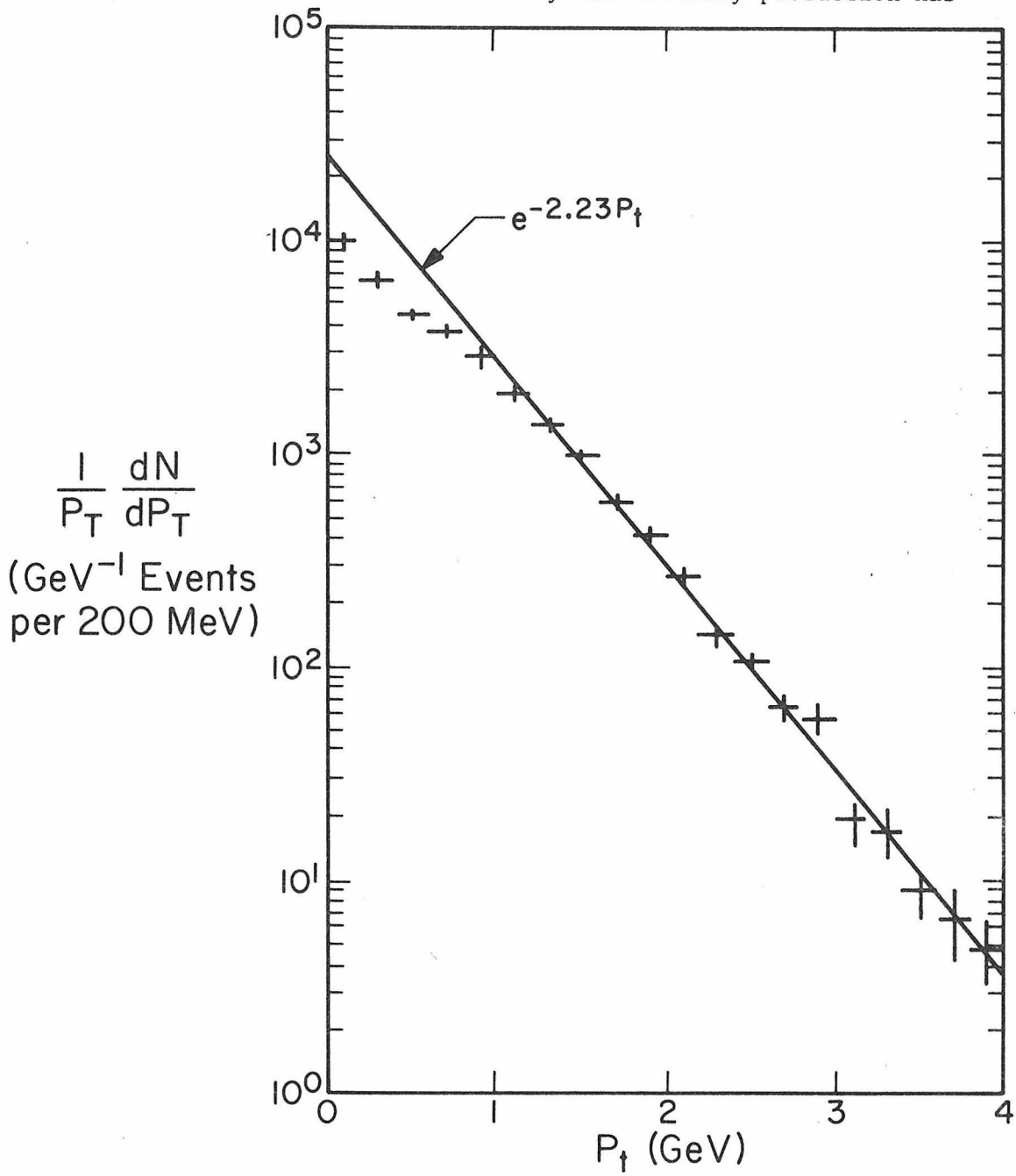

been performed, nor one for non-resonant production. The curve represents the best fit to the form $e^{-bP}t$: $b = 2.23 \pm .05$ ($\chi^2 = 8.6$ for 12 D.F.). The data below P_t of 1.2 GeV have been excluded from the fit. The normalization is $1.10 \pm .22$ picobarns per nucleon per event.

increase in the χ^2 for the fit. In order to gain a feeling for the amount of curvature, a fit was also made to the data for P_t less than 1.2 GeV, yielding a value for b of 1.52 ± .08 (χ^2 = 5.7 for 4 D.F.).

G. Decay Angular Distribution

The angular distributions in the s channel helicity frame (also known as the Jacob-Wick frame[13]) both before and after correction for secondary production are shown in figures 5-8 and 5-9 respectively. The effects of secondary production are seen to be negligible.

Two fits to the corrected data were made. The first, a flat fit, yields a χ^2 of 13.9 for 9 degrees of freedom. The second, a fit to the form $1 + P\cos^2\theta^*$ yielded a best value for P of .156 ± .079 (χ^2 = 10.0 for 8 D.F.). If we consider this distribution as composed of a flat component and a $(1 + \cos^2\theta^*)$ component, then after integration over angles, the $(1 + \cos^2\theta^*)$ component comprises a fraction $\frac{4P/3}{1 + P/3}$ of the total production, or .20 ± .10 in this case.

This figure may be compared with the fraction .106 ± .011 of non-resonant production obtained by inspection of the raw invariant mass distribution (section B) with two caveats. Firstly, the acceptance of the apparatus is falling near $|\cos\theta^*|$ of 1, exactly the region where $(1 + \cos^2\theta^*)$ production is large, and thus the fraction of observed $(1 + \cos^2\theta^*)$ events would be expected to be less than the fraction of actual events. Secondly, the polarization in the s channel helicity frame from Drell-Yan type events is not expected to be as great as unity since the polarization occurs in the rest frame of a quark-anti-quark collision. For example, Collins and Soper[14] have estimated

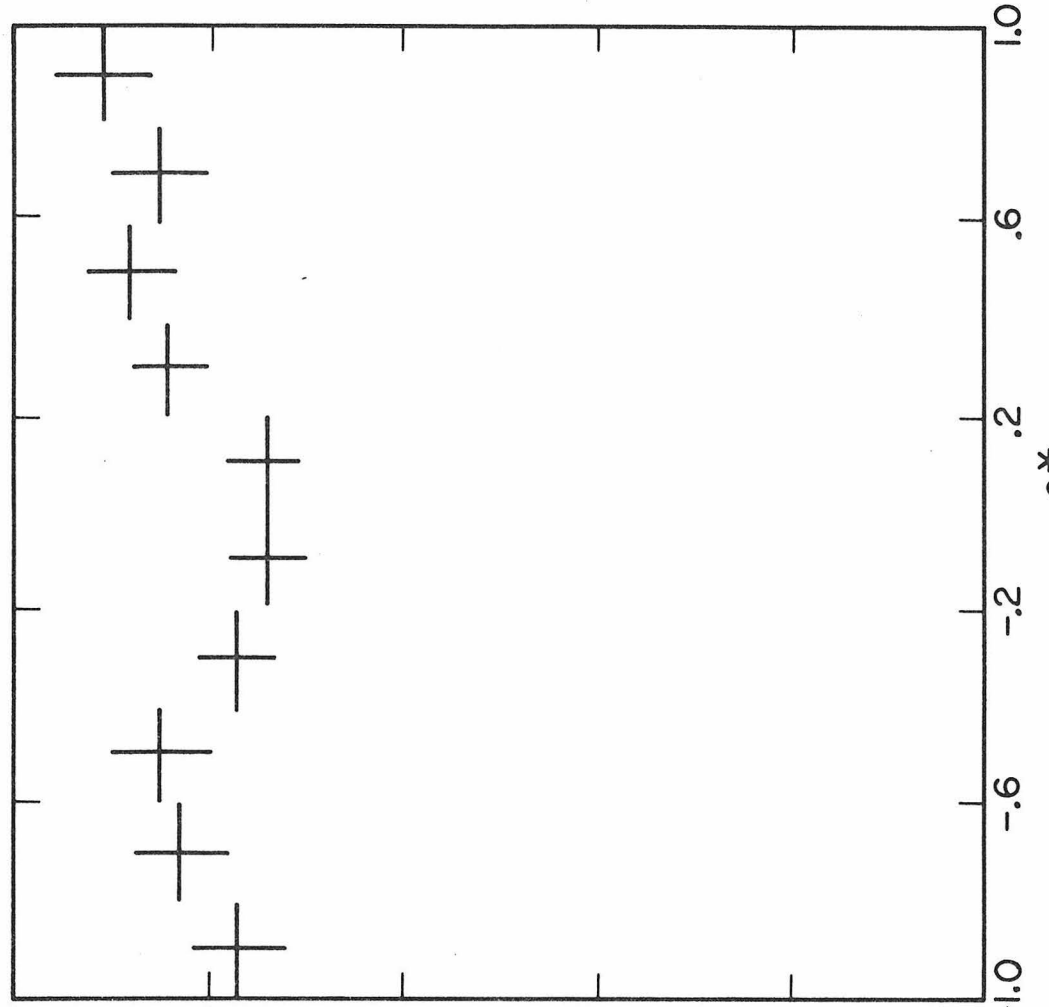

Figure 5-8:
Angular distribution of events in ψ mass bin as measured in the s channel helicity frame (Jacob-Wick frame), corrected for acceptance (figure 4-11). No corrections for secondary or tertiary production or for non-resonant production have been made.

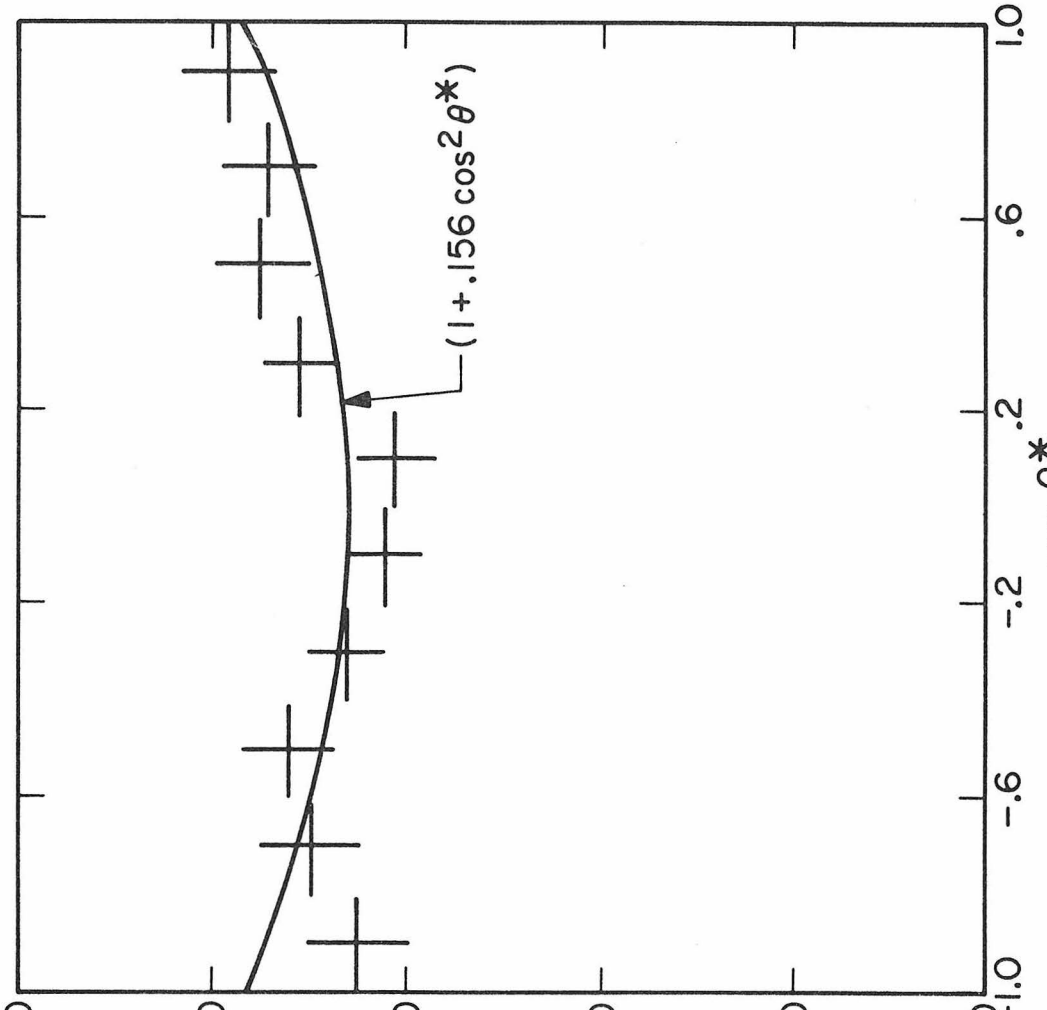

Figure 5-9:
Angular distribution of events in ψ mass bin as measured in the s channel helicity frame (Jacob-Wick frame). The data have been corrected for acceptance (figure 4-11) and a subtraction made for secondary and tertiary production. The curve represents the best fit to the form $1 + P\cos^2\theta^*$: $P = .156 \pm .079$ ($\chi^2 = 10.0$ for 8 D.F.). The normalization is $1.29 \pm .26$ picobarns per nucleon per event.

that $(1 + \cos^2\theta^*)$ production in the $q\text{-}\bar{q}$ rest frame may produce a flat component containing of order $\frac{3\langle p_t^2 \rangle}{2M^2} \simeq .15$ of the events in a certain frame identical to the s channel helicity frame at x_F of 0, where most of the events observed in this analysis occur. Bearing all of this in mind, a model of flat ψ production with an 11% background from Drell-Yan type production does not seem inconsistent with the observed distribution.

REFERENCES

5-1 Sidney D. Drell and Tung-Mow Yan, Phys. Rev. Lett 25, 316, (1970).

5-2 e.g. K. Anderson et al., Phys. Rev. Lett. 37, 799, (1976) show a ratio of 710 to 3.3 at 150 GeV.

5-3 M. J. Shochet, in "Proceedings of Summer Institute on Particle Physics, July 11-22, 1977," SLAC-204, p. 321.

5-4 Fit by M. J. Shochet, Ref. 5-3, p. 330.

5-5 F. E. Taylor et al., Phys. Rev. D14, 1217, (1976).

5-6 W. Busza, Acta Phys. Pol. B8, 333, (1977).

5-7 The data of Ref. 5-6 for the $A^{-.25x_F}$ fit were taken between x_F of .3 and .9.

5-8 This represents a fit to data presented in review by W. R. Innes in "Proceedings of Summer Institute on Particle Physics, July 11-22, 1977," SLAC-204, p. 425.

5-9 A. S. Carroll et al., Preprint FERMILAB-Pub-78/80-EXP; and private communication.

5-10 M. Binkley et al., Phys. Rev. Lett. 37, 571, (1976); J. G. Branson et al., Phys. Rev. Lett. 38, 1334, (1977); and B. C. Brown et al., preprint FERMILAB-77/54-EXP.

5-11 J. G. Branson et al., Phys. Rev. Lett. 38, 1331, (1977).

5-12 J. G. Branson, Ph.D. thesis, Princeton University, COO-3072-81, (unpublished).

5-13 M. Jacob and G. C. Wick, Annals of Physics 7, 404, (1959).

5-14 J. C. Collins and D. E. Soper, Princeton University Preprint.

CHAPTER VI

CROSS SECTIONS AND SUMMARY

A. Cross Section Results

The product of zero rapidity (y) cross section and ψ dimuon branching ratio (B) was determined from the fit of the x_F distribution $\frac{dN}{dx_F}$ with secondary production events subtracted (figure 5-5). The fit value of $\frac{dN}{dx_F}\Big|_{x_F=0}$ was 47900 ± 1660 events. Multiplication by the single event sensitivity of 1.29 ± .26 picobarns per nucleon (section D of chapter V) yields a value for $B\,\frac{d\sigma}{dx_F}\Big|_{x_F=0}$ of 61.8 ± 12.6 nanobarns per nucleon. Scaling by an additional factor of $2m_{\mu\mu}/\sqrt{s}$ gives $B\,\frac{d\sigma}{dy}\Big|_{y=0}$ = 14.0 ± 2.9 nanobarns per nucleon. Emphasis should be placed on the fact that the largest source of the quoted error lies in the A dependence, i.e. in converting cross section per nucleus to cross section per nucleon. The more basic result is that 7.43 ± .34 x 10^{-7} of all incident protons produced a ψ decaying to two muons in a unit of rapidity at y of zero in their primary interaction.

The ψ total cross section was determined from the observed distribution $\frac{dN}{dx_F}$ (figure 5-5). Summing the observed region of x_F from -.25 to .40 yields 15437 ± 543 events. Extending the observed distribution $(1 - |x_F|)^{4.41 \pm .27}$ over all x_F, we calculate that 86.3 ± 1.3 percent of all ψ events lay in the observed x_F region. Thus the observed value of $B\sigma$ is 22.9 ± 4.7 nanobarns. Because of the large acceptance of the apparatus, this result is quite insensitive to the details of the distribution outside of the observed x_F region. Again, if we ignore the questions of A dependence and proton-iron inelastic cross section, the basic result is that 1.22 ± .06 x 10^{-6} of primary proton-iron collisions at 400 GeV produce a ψ decaying to two muons.

B. Cross Sections From Other Experiments

Comparison of the cross section results of this experiment with published data on hadronic ψ production [1] is made difficult by the varying beam projectiles and energies employed, differing apparatus acceptance available, and divergent assumptions on both angular dependence (section E) and A dependence (section F). In particular, comparison to pion-nucleon cross section magnitudes is impossible without large theoretical overhead because the pion contains a valence antiquark. The remaining nucleon-nucleon experiments may be divided into three classes: (1) ISR experiments, (2) fixed target double arm 90 degree spectrometers, and (3) fixed target forward spectrometers.

Of the published ISR results, the first, from the CERN, Columbia, Rockefeller, Saclay e^+e^- pair experiment (Büsser et al.[1]), contains 9 ψ events at $\sqrt{s}$ from 30 to 53 GeV. The apparatus covered rapidity from -.32 to .32, observed a flat y distribution, and quoted $B\frac{d\sigma}{dy}$ = 7.5 ± 2.5 nanobarns, with an increase of 60% if the b parameter in the P_t distribution (see section F of chapter V) was 2 instead of 3. The CERN, Hamburg, Orsay, Wien collaboration (Nagy et al.[1]) observed ψ muon pairs at $\sqrt{s}$ of 52 GeV, with a mean P_t corresponding to a b of 2. Their x_F acceptance ran from .2 to .6, with a quoted $B\frac{d\sigma}{dy}$ of 7.2 ± 2.4 nanobarns at $\langle y \rangle$ = 1.6. Finally, a BNL, CERN, Syracuse, Yale group (Cobb et al.[1]) reported cross sections to e^+e^- pairs from their initial data in 1977. Their data, with a b parameter of 2.1 ± .4, and acceptance running from y of -.65 to .65 (quite similar to this experiment), were based on 6, 13, 42, and 15 events at $\sqrt{s}$ of 23, 31, 53 and 63 GeV respectively. Quoted values of $B\frac{d\sigma}{dy}\Big|_{y=0}$ were 5.9 ± 3.9,

8.4 ± 5.0, 16.6 ± 9.2, and 31.9 ± 18.8 nanobarns. The observed rapidity distribution was consistent with flat.

Of the double arm spectrometer experiments, the e^+e^- pair work of the MIT-BNL group (Aubert et al., [1]) was of course responsible for the discovery of the ψ. Their quoted cross section was $\sim .1$ nanobarn at $\sqrt{s}$ of 5.1 GeV. The most recent results from the Columbia, Fermilab, Stony Brook collaboration (Brown et al.[1]) claim a rapidity distribution consistent with flat from -.2 to .3 at 400 GeV, and from -.4 to .4 at 300 GeV. The $B \left.\frac{d\sigma}{dy}\right|_{y=0}$ for muon pairs at 400 GeV was 10.6 ± 2.7 nanobarns, while for e^+e^- pairs it was 8.8 ± 2.2 nanobarns. A 300 GeV electron pair measurement yielded 6.5 ± 1.2 nanobarns. The acceptance was calculated assuming an angular distribution of $1+\cos^2\theta^*$ a flat distribution would increase their cross sections by 60 percent. The CFS 400 GeV muon data set, comprised of 843 events on Cu and 294 on Be (for an $A^{.9}$ dependence) is the result most directly comparable with the $B \left.\frac{d\sigma}{dy}\right|_{y=0}$ determined in this thesis.

Of the forward spectrometers, we consider first those at Fermilab energies. The Northeastern experiment (Blanar et al.[1]) measured ψ dimuons in a 240 GeV beam, finding that $5.9 \pm 3.0 \times 10^{-8}$ of protons interacting in iron produce a ψ at $|x_F| > .38$. The Columbia, Hawaii, Illinois, Fermilab collaboration (Binkley et al.[1]), working with a 300 GeV neutron beam, found 3.5 nanobarns of ψ dimuon cross section between x_F of .24 and 1.0, using their own measured $A^{.93}$ dependence. Assuming a flat rapidity distribution for $|x_F| < .3$, they calculate $B \left.\frac{d\sigma}{dy}\right|_{y=0} = 8.9$ nanobarns, and $B\sigma = 22$ nanobarns. Finally, the Chicago-Princeton group (Branson et al.[1]) has measured ψ muon pairs at 225 GeV, using the Chicago Cyclotron Spectrometer, for $x_F \geq .05$. Extrapo-

lating to x_F of zero, and using a linear A dependence, they find $B \left.\frac{d\sigma}{dy}\right|_{y=0}$ of ~ 5 nanobarns per nucleon on carbon. They also quote[2] a $B\sigma$ of 71 ± 3 nanobarns per carbon nucleus (statistical errors only) for $x_F > 0$, working from a sample of 1007 events.

The early result of the Sigma group (Antipov et al.[1]), using 70 GeV protons on beryllium, was a total cross section $B\sigma$ of 9.5 ± 2.5 nanobarns per nucleus to muon pairs.

C. P_t Distributions

A summary of P_t distributions for ψ events is given in Table 6-1. Recall that $\frac{1}{P_t}\frac{d\sigma}{dP_t}$ is fit to the form e^{-bP_t}, and thus the mean P_t is 2/b. It should be emphasized that although this experiment obtained b = 2.23 ± .05 for P_t between 1.2 and 4.0 GeV, at lower P_t the value 1.52 ± .08 was found for b. It should also be noted that although the result of the Goliath spectrometer (Abolins et al.[1]) has the smallest quoted error, the χ^2 per degree of freedom for that measurement was 5.2, reflecting a similar change in exponential slope with P_t. Similarly, the most recent Chicago-Princeton result (b = 2.2 ± .05) was restricted to the $P_t > 1$ GeV region.

D. x_F Distributions

The x_F distributions can typically be determined best by the fixed target forward spectrometer experiments. Both the ISR and double arm 90 degree spectrometer experiments are sensitive to relatively small regions around x_F of zero, and all report rapidity distributions consistent with flat.

TABLE 6-1

P_t DISTRIBUTIONS

First Author	E_{beam}	Beam	Target	Lepton	b
This expt.	400	p	Fe	μ	2.23 ± .05
Büsser	$\sqrt{s}$=30-53	p	p	e	$\langle P_t \rangle$ = .67
Nagy	$\sqrt{s}$=52	p	p	μ	$\langle P_t \rangle$ = 1.0 ± .2
Cobb	$\sqrt{s}$=23-63	p	p	e	2.1 ± .4
Snyder	400	p	Be	e	1.6 ± .35
Brown	400	p	Be,Cu	e	1.54 ± .14
Brown	400	p	Be,Cu	μ	1.50 ± .10
Brown	300	p	Be,Cu	e	1.65 ± .23
Blanar	200	π^-	Fe	μ	1.6 ± .2
Blanar	240	p	Fe	μ	2.2 ± .5
Binkley	300	n	Be,Al,Cu,Pb	μ	1.6 ± .2
Anderson	150	π^+	Be	μ	2.57 ± .36
Anderson	150	p	Be	μ	2.08 ± .26
Branson	225	p	C	μ	2.05 ± .09
Branson	225	p	Sn	μ	2.02 ± .14
Branson	225	π^+	C	μ	2.06 ± .10
Branson	225	π^+	Sn	μ	1.78 ± .15
Branson	225	π^-	C	μ	1.98 ± .13
Kirk	217	π^-	p	μ	1.16 ± .18
Kirk	217	π^-	Be	μ	1.66 ± .22
Abolins	150	π^-	Be	μ	1.855 ± .027
Anderson	225	π^-	C,Cu,W	μ	2.2 ± .05

Of the nucleon-nucleon forward spectrometer experiments, fitting $E\frac{d\sigma}{dx_F}$ to the form $(1 - |x_F|)^c$, The Columbia, Hawaii, Illinois, Fermilab group reports $c = 5.2 \pm .5$ for $x_F > .3$, using 300 GeV incident neutrons on various nuclei. They assume a flat distribution below x_F of .3 in calculating their cross sections. The Chicago-Princeton experiment with 150 GeV protons on beryllium quotes c of $2.94 \pm .32$ for $x_F > .15$, and with 225 GeV beams claims $c = 3.44 \pm .14$ for $x_F \gtrsim .05$ on a carbon target, and $4.01 \pm .37$ with a tin target.

Use of a pion beam, containing a valence antiquark, tends to increase the yield of high x_F, and thus lowers the value of the parameter c. The Chicago-Princeton experiment obtained a value $1.72 \pm .38$ for 150 GeV π^+ on beryllium, while at 225 GeV the results were $1.33 \pm .21$ for a carbon target and $1.50 \pm .28$ with tin. With a π^- beam on carbon target they also quote the value $1.93 \pm .20$. In a modified version of the same apparatus, the Fermilab, Harvard, Illinois, Oxford, Tufts collaboration (Kirk et al.[1]), using a 217 GeV π^- beam, reports c of $1.11 \pm .28$ on hydrogen and $1.39 \pm .33$ on beryllium.

The results of the Goliath group are cast in a different form. They fit $\frac{d\sigma}{dx_F}$ to the form $(1 - |x_F - x_0|)^a$, and find values of $.20 \pm .06$ $2.60 \pm .13$ for x_0 and a respectively. Qualitatively similar distributions were obtained with 39.5 GeV π^+ and π^- beams on copper by the CERN Omega group (Corden et al.[1]).

Finally, the Chicago-Princeton group has recently presented new data for ψ production by 225 GeV antiprotons. Using a carbon target, and on the basis of 46 $\bar{p}$ induced events, they find $\frac{\sigma(\bar{p}C \to \psi X)}{\sigma(pC \to \psi X)} = 1.2 \pm .6$. Fitting $\frac{d\sigma}{dx_F}$ to the form $(1 - |x_F|)^a$, they find values for a of $2.20 \pm$

.06 and 1.99 ± .05 for π^+ and π^- beams, and 4.30 ± .10 and 3.90 ± .40 for protons and antiprotons respectively.

Theoretical attempts to fit both the nucleon-nucleon and the flatter pion-nucleon x_F distributions typically use some combination of gluon-gluon fusion cascading through intermediate ψ states and light quark fusion[3]. Most of the nucleon-nucleon distribution can be explained by the gluon-gluon portion, but the high x_F region of the pion-nucleon result is quite sensitive to the quark-antiquark fusion component, and so models vary both the amount of this contribution and the shape of the quark distributions, especially for the valence quarks in the pion, in order to fit these experiments' results. Because the nucleon does not contain valence antiquarks, the data from this thesis are most useful for determining the nucleon gluon distribution in the context of the gluon fusion model.

E. Angular Distributions

The angular distribution of decays in the ψ rest frame $\frac{d\sigma}{dcos\theta^*}$ is fit to the form $1 + Pcos^2\theta^*$, where we have defined θ^* as the s channel helicity angle of the positive muon. This experiment reports P = .16 ± .08, but without correction for a continuum contribution of 11% in the ψ mass bin (section G of chapter V), and claims a distribution consistent with flat after the correction. The Columbia, Fermilab, Stony Brook collaboration reports a value of P near unity, and more than three standard deviations away from zero. They have also tried fitting the distribution in the t channel (Gottfried-Jackson) frame, but failed to get a good fit.

The Goliath group had initially reported a P of $-.66 \pm .1$ in the t channel frame, but now claims a distribution consistent with flat. The first 225 GeV result of the Chicago-Princeton group was a P of $-.28 \pm .22$ in the s channel frame. Their more recent analysis includes values of $.03 \pm .04$, $.33 \pm .06$, $.09 \pm .06$, and $-.10 \pm .05$ in the s channel, t channel, u channel, and Collins-Soper frames respectively, based mostly on π^- data.

A flat angular distribution is predicted in the gluon cascade model, where the ψ is produced in the decay of a spinless particle. However, in a Drell-Yan type quark-antiquark fusion, the helicities of the quarks force an alignment along the collision axis, and thus a $1 + \cos^2\theta$ distribution with respect to the quark-antiquark direction in the ψ rest frame.

F. Atomic Weight Dependence

In fitting ψ cross sections on nuclei to the form A^α, the Columbia, Hawaii, Illinois, Fermilab collaboration obtained a value $\alpha = .93 \pm .04$ for 300 GeV neutrons[4]. The Chicago-Princeton group then reported $\alpha \approx .9$ for 225 GeV π^+ and proton beams[5]. The exponent for π^+ production appears to be closer to .8, while the proton data, with twice the statistics at the ψ mass, has an α of .9[2].

The recent Columbia, Fermilab, Stony Brook experiments quotes a value $\alpha = .90 \pm .10$ for 400 GeV protons. The Sigma group also quotes a value $.92 \pm .06$ for a 43 GeV π^- beam. Finally, the new high statistics 225 GeV π^- experiment of the Chicago-Princeton group has studied α as a function of both x_F and P_t. They find no significant variation with x_F,

but a systematic increase from $\sim$.9 at P_t of 0 to $\sim$1.1 at P_t of 3 GeV. The overall value is approximately .99 $\pm$ .04.

G. Associated Production

The question of OZI rule allowed production, in which additional charmed particles are created along with the ψ, has prompted several searches for D mesons or their decay muons produced in association with ψ's. The Columbia, Hawaii, Illinois, Fermilab collaboration reported no additional muons in a sample of 2500 ψ's above the level expected from π and K decays, and quoted a 90% confidence limit $\frac{2B(C \rightarrow \mu X)\sigma(\psi C\bar{C})}{\sigma(\psi)} <$ .006 (here C represents any charmed particle)[6]. The Chicago-Princeton group obtained a similar limit, and assuming a value .1 for $B(C \rightarrow \mu X)$, they quote a 90% confidence limit $\frac{\sigma(\psi\bar{C}C)}{\sigma(\psi)} <$ .010[7]. They have also considered the possibility of double ψ production, and present the result $\frac{\sigma(\psi\psi)}{\sigma(\psi)} <$ .021.

Preliminary results from the Goliath group have been presented from data in a 140 GeV π^- beam. The data have been searched for possible D meson decays in association with ψ production, and 4 $K^+\pi^-\pi^-$, 3 $K^-\pi^+\pi^+$, 1 $K_s^0\pi^+$, and 1 $K_s^0\pi^-$ events have been found with varying backgrounds. No acceptance corrected associated production probabilities have yet been presented[8].

The data regarding third muon production from this thesis experiment are still undergoing analysis. A preliminary result is that $\sim$ 10 of $\sim$ 5500 ψ events have a third muon of sufficient energy ($\gtrsim$ 7 GeV) to have momentum measured in the spectrometer. The contribution to this sample resulting from π and K decays has not been determined as yet,

but a preliminary estimate based on third muons accompanying lower mass pairs indicates that this contribution is of the same order of magnitude as the observed signal. The acceptance for a third muon has likewise not been determined, but a crude guess, based on D mesons produced at rest in the center of mass, with 50% of muons produced having an energy greater than 500 MeV in the D rest frame, and those muons in the forward hemisphere being accepted, indicates an acceptance in the vicinity of 25%. A 10% $D \rightarrow \mu$ branching ratio would then yield $\frac{\sigma(\psi D\bar{D})}{\sigma(\psi)} \approx .04$ if the π and K decay contribution to the observed third muons were zero. At this time, the 4% figure represents only a very crude limit on associated production.

REFERENCES

6-1 J. J. Aubert et al., Phys. Rev. Lett. 33, 1404 (1974); B. Knapp et al., Phys. Rev. Lett. 34, 1044, (1975); F. W. Büsser et al., Phys. Lett. 56B, 482, (1975); G. J. Blanar et al., Phys. Rev. Lett. 35, 346, (1975); E. Nagy et al., Phys. Lett. 60B, 96, (1975); K. J. Anderson et al., Phys. Rev. Lett. 36, 237, (1976); D. Eartly et al., Phys. Rev. Lett. 36, 1355, (1976); H. D. Snyder et al., Phys. Rev. Lett. 36, 1415, (1976); M. Binkley et al., Phys. Rev. Lett. 37, 574, (1976); K. J. Anderson et al., Phys. Rev. Lett. 37, 799, (1976); Yu. M. Antipov et al., Phys. Lett. 60B, 309, (1976); J. G. Branson et al., Phys. Rev. Lett. 38, 1331, (1977); M. J. Corden et al., Phys. Lett. 68B, 96, (1977); J. H. Cobb et al., Phys. Lett. 68B, 101, (1977); Yu. B. Busnin et al., Phys. Lett. 72B, 269, (1977); Yu M. Antipov et al., Phys. Lett. 72B, 278, (1977); E. Amaldi et al., Lett. al Nuovo Cimento 19, 152, (1977); B. C. Brown preprint FERMILAB-77/54-EXP; J. H. Cobb et al., Phys. Lett. 72B, 497, (1978); A. Bamberger et al., CERN preprint 78-0008; T. B. W. Kirk et al., preprint FERMILAB-78/76-EXP; M. A. Abolins et al., paper submitted to the XIX International High Energy Physics Conference, Tokyo, Japan, 23-31 August, 1978; K. J. Anderson et al., paper submitted to the XIX International High Energy Physics Conference, Tokyo, Japan, 23-31 August, 1978.

6-2 J. G. Branson, Ph.D. thesis, Princeton University COO-3072-81, (unpublished).

6-3 M. Glück, J. F. Owens, and E. Reya, Phys. Rev. D17, 2324, (1978); C. E. Carlson and R. Suaya, Phys. Rev. D18, 760, (1978).

6-4 M. Binkley et al., Phys. Rev. Lett. 37, 571, (1976).

6-5 J. G. Branson et al., Phys. Rev. Lett. 38, 1334, (1977).

6-6 M. Binkley et al., Phys. Rev. Lett. 37, 578, (1976).

6-7 J. G. Branson et al., Phys. Rev. Lett. 38, 580, (1977).

6-8 R. Barate et al., paper presented at the XIIIth Rencontre de Moriond, Les Arc, France, 12-24 March, 1978.

APPENDIX A

CALORIMETER INSTRUMENTATION

1. Upstream Calorimeter

A calorimetry counter constructed from plastic scintillator 1/4" thick and 30" square was clamped to the downstream face of each of the 45 steel plates of the upstream calorimeter. The counters were each viewed by a single 2" diameter 10 stage photomultiplier tube, typically of RCA type 6342A. A few counters with low light output were equipped with RCA type 4518 phototubes, which are variants of the 6342A with bi-alkali photocathodes. In order to allow for closer packing and to partially correct for attenuation of scintillation light in the counters, phototubes were positioned alternately on the top and bottom of consecutive counters, and were also displaced towards the left or right side of successive top and bottom counters.

Tube bases provided a direct coupled anode signal, and in addition, an AC coupled output from a 733 amplifier circuit (typical gain 30-50) located within the base. The amplified outputs were only used to look at low pulse height from a low intensity muon beam passed through the apparatus for calibration purposes. The larger pulse heights associated with hadron showers occurred in a high rate ($\sim$ 1 MHz) beam, and thus DC coupling was necessary to digitize them. In general, the entire electronic path for the high gain (low pulse height) signals was AC coupled, while that for the high rate low gain signals was DC coupled.

Each counter was provided with an LED, which was pulsed once per

accelerator cycle to provide a crude check of counter operation. In addition, the first 31 counters viewed, via a fiber optic system, a spark gap which was pulsed 30-60 microseconds after each event. The fiber optic system also distributed the spark light to three reference phototubes, one of which viewed only the spark gap, and the other two of which were additionally coupled to sodium iodide detectors provided with Americium reference sources. This system was necessary in order to monitor both long term tube calibration changes and short term rate dependent gain shifts due to the large rate of light detected during beam pulses ($\sim 10^{10}$ photoelectrons per second).

The phototube anode signals were first routed to passive .75/.25 signal splitters. The 25% outputs were then mixed by LRS type 127L linear fan-ins into 7 composite signals each of which represented the sum of every seventh counter (i.e. counters 1, 8, 15,...43 in the first unit; 2, 9, 16,...44 in the second; etc.). These "superlow" signals ("superlow" refers to the amount of gain employed--superlow signals were used to measure very large pulse heights) were then distributed to integrating ADC units (LRS 2249A), and to a single mixer which provided the sum of all 7 superlows, and thus of all 45 counters, in a single linear signal, E_{sum}, representing all the observed energy in this calorimeter. The E_{sum} signal was utilized in the trigger logic: when more than 600 GeV was observed, it was assumed that more than one beam particle had entered the apparatus in the same RF bucket, and the beam particles were rejected.

The remaining 75% of anode signal was routed to another LRS 2249A ADC; in the case of the first 31 tubes, passing first through an LRS

428 DC coupled linear fan-out. These 31 channels were each provided with yet another ADC to measure the pulse charge produced from the spark/gap fiber optic signal generated after each event. This additional ADC on the same signal channel was required because the previous unit was still busy digitizing the pulse charge from the actual event when the spark gap was fired. In addition, the signals from counters 3-10 were mixed and then discriminated. A pulse height of $\gtrsim 50$ minimum ionizing particles generated a logic signal, designated F3-10, indicating that a beam particle had interacted in the first 10 plates of the target-calorimeter. This signal was a necessary requirement for all good beam particles.

The amplified counter signals were cabled to AC coupled fan-outs built at Stanford, and thence to an additional "high" (i.e. high gain) ADC. These ADC signals suffered from base line shifts due to AC coupling during normal running, and were generally used only to measure single minimum ionizing particle pulse heights when a muon beam was brought into the apparatus. Once the energy deposited by single minimum ionizing particles had been determined, the energy deposition from hadron showers could be expressed in equivalent minimum ionizing particles.

2. Downstream Calorimeter

A set of four counters each 10" wide by 48" high was located behind each of the ten plates of the downstream calorimeter. Each of the 40 counters was viewed by a 2" diameter 14 stage Amperex 56AVP phototube. Tube bases were located on top and bottom of alternate sets of

four counters in order to correct for attenuation of scintillation light in the counters. For the relevant portion of the run, the tube anode signals were connected to LRS 2249A ADC's through Stanford AC coupled fan-outs. A second fan-out output was mixed with the signals from the other 3 counters in the same plane, and the resulting 10 plane signals were summed to provide an eighth superlow, which was then routed to an ADC.

3. Calorimetry Monitoring

A series of custom electronic modules and a number of special procedures were utilized to monitor the health of the calorimeter and provide information for corrections to the data for long term gain shifts in the phototubes and short term beam rate dependent effects. Equipment employed included LED and spark gap pulsing systems, "event history" modules, and a "flying scaler" to monitor beam history. Four types of special calibration events were collected during each accelerator cycle to aid in the above tasks.

The basic calorimetry ADC data group collected for each physics event consisted of the outputs of 182 10 bit plus overflow gated integrating pulse charge digitizers. The first 144 of these were gated on the actual events, and contained data from the 45 unamplified "low" (i.e. low gain) upstream calorimeter counters, 45 upstream highs, 7 upstream superlows, upstream E_{sum}, 40 downstream counters, and the downstream superlow. The next 36 channels were gated on the spark gap pulse after the event, and contained data from the first 31 upstream counters and the reference tube not connected to an NaI detector. The

last two ADC's were associated with the remaining fiber optic reference channels. These units were not standard LRS 2249A CAMAC circuits, but were UNIBIN modules employing essentially identical circuitry. They were additionally connected to a PHA module which kept histograms of the pulse height distributions from the NaI detectors. These spectra were read twice per accelerator cycle, once for NaI events accumulated during the beam off period, and once for the beam on period.

The primary reference for monitoring changes in phototube gain was the NaI system. The gain of the reference tubes was calibrated by observing the location of peaks in the PHA histograms. The calorimetry tubes were then cross-calibrated to the reference tubes via the fiber optic/light flasher system.

Approximately one second before the beginning of each beam pulse, base lines in all 182 ADC's were determined by gating the integrators without an actual event taking place. After this pedestal event had been acquired, an LED event was generated in which the first 144 ADC's contained data from LED's pulsed on each of the 85 calorimetry counters, and the remaining ADC's converted the pulses from a subsequent firing of the spark gap/fiber optic system.

A pair of 192 bit long shift registers were loaded with the logic signal BLOB, indicating a beam particle entering the apparatus. These registers were continually clocked by the 53 MHz accelerator RF signal, distributed to the experiment via the Neutrino Area CCTV system, and were stopped $\sim$ 150 nanoseconds after physics events and spark gap firings respectively. They were then read out broadside as 12 16 bit data words each, and thus presented the beam history for 192 RF buckets

preceding their stopping. The data from these registers were used primarily to search for events with additional beam particles a few hundred nanoseconds in advance of the trigger. An event by event correction could be made for effects of the tails of the phototube pulses from this additional beam being integrated along with the pulses from the triggering event. Since these tails might extend for as long as a microsecond, this correction became important when beam rates exceeded $\sim 10^5$ Hz.

The average beam intensity for up to 300 microseconds preceding each event was recorded by a flying scaler module--a collection of 3 banks of 4 8 bit scalers counting the BLOB signal. The members of the first bank were each reset every 256 RF buckets, with one of the four being reset every 64 buckets. The elements of the second bank were similarly reset every 4096 buckets, and those of the third set every 32768 buckets. A 16 bit RF scaler provided data on the most recently reset unit in each bank, and the time remaining until the next reset pulse. All 12 BLOB scalers and the RF counter were stopped upon triggering on an event. This intensity information was used to make a multiplicative correction to the calorimetry pulse heights for rate dependent gain shifts, typically substantial for rates exceeding 10^5 Hz, and in the cases of the single and zero muon analyses, to make cuts on the data.

A 24 bit scaler counting a 1 MHz clock from the beginning of the beam pulse was also read for each event. This provided for checks on possible correlations between phototube gain and the length of time the tubes had been exposed to high light levels.

The resolution results for various calibration schemes, as well as the effects of data corrections and cuts, and the dependence of resolution and calibration on beam rate, are dealt with in detail in the Stanford University thesis of J. P. Dishaw[1]. The resolution obtained by the hardware E_{sum} signal was 4.5-6.5%, while that obtained off-line with all necessary calibrations was 3.40% at low (10^4 Hz) beam rate. The resolution obtained at high (10^6 Hz) beam rate, after all possible corrections for rate dependent effects had been applied, was 3.50%. Calorimeter response was linear with beam energy to within .2% over a range of energies from 30 to 450 GeV[2].

REFERENCES

A-1 J. Patrick Dishaw, Ph.D. thesis, Stanford University.

A-2 J. P. Dishaw, private communication.

APPENDIX B

SPARK CHAMBER PROCESSING AND TRACK RECONSTRUCTION ROUTINES

1. CD Chamber Spark Preprocessing

Conversion of CD data from encoded spark clusters (see section F of chapter II) to spark coordinates was accomplished by two preprocessing routines: UPKPLN and PLANE. The first of these performed hardware operation checks and separated the raw data bank into portions associated with each of the 20 CD planes; the latter routine performed the actual coordinate calculations.

In detail, UPKPLN searched for the plane identifier words marking the boundaries between data from successive planes. The routine verified that all words which were in plane ID format identified valid planes, and that ID's from all 20 planes were present and appeared in the proper order. The sparks within each plane were then checked to ensure that they appeared in strictly increasing wire number order, and that all sparks appeared on wires that actually existed, e.g. not on wires 2.0 meters from the edge of a chamber only 1.2 meters wide. A small fraction of events, typically $\leqslant .025\%$ was rejected at this stage because the events failed to pass these status checks. In addition, $\sim 1.5\%$ of events had more sparks than could fit in the 384 word buffer allocated for CD data in each raw data record.

The routine PLANE then found the wire number corresponding to the center of each spark cluster, multiplied by the average inter-wire spacing, and added this result to the known location of the edge of the wire plane. Spark clusters extending over the boundary between succes-

sive 32 wire boards were merged from their components on each board. In addition, a single hit wire separated from a cluster of hits by a single missed wire was merged into the cluster. This operation was necessitated by a form of spark robbing, in which there was minimal ionization near the edge of a large cluster, and which occurred in only a few percent of the sparks.

2. CIT Chamber Spark Preprocessing

Conversion of CIT spark data from MTD clock counts (see section H of chapter II) to spark coordinates was performed by routines UPKWND and WAND. The first of these converted the status work constructed by the on-line data collection system for each wand into its component parts: the number of sparks on the wand, their location in the 200 word CIT spark buffer, and status bits indicating whether more sparks had occurred than could fit in the MTD memory, and whether the first spark on the wand had been less than 2500 counts, assumed by the data collection program to be the first fiducial marker, and therefore subtracted from all subsequent sparks on that wand for that event.

The sparks on each wand were then checked for monotonicity, and events with more than one spark out of order were rejected, as were events with insufficient buffer space to hold all CIT sparks. These cuts removed $\sim 1\%$ of the data sample. Events with only one spark out of order were not cut because they represented the result of a well understood and relatively common ($\sim 4\%$ of data) hardware failure in which a spark from the previous event was not overwritten in the MTD's memory.

The routine WAND then converted spark clock counts into coordinates using the known positions of the fiducial marks and the speed of sound in the wand. This speed was updated every 100 events using all events whose second fiducial locations had occurred within 20 clock counts of their expected positions.

Sparks before the first fiducial or after the second fiducial were rejected, as were edge sparks within 100 counts of either fiducial, sparks within 10 counts of the preceeding spark, and all sparks on wands missing first fiducials. Events in which a second fiducial was not found for a given wand had an error flag set for that wand, but the sparks were passed and the nominal location of the second fiducial was assumed. Sums of sparks processed, sparks rejected, and events with second fiducials missing were maintained for each wand and printed at the end of each run.

3. Straight Line Segment Finding

Line segments in both upstream spark chamber modules and the CIT cart downstream of the spectrometer magnet were found separately in both x and y projections by routine LINE. This program searched 4 x or y CD chambers in the first upstream module, 4 x or y CD chambers in the second module together with the first 10' by 10' x-y plane (two 5' by 10' chambers) of CIT chambers upstream of the magnet, or the last 4 10' by 10' planes (one 10' by 10' plus six 5' by 10' chambers) downstream of the magnet.

The segments were found by exhaustive search. A sufficient number of base chamber pairs were tried to ensure that any three spark track

would be found. Once a pair of base chambers had been chosen, straight lines were constructed between all possible combinations of sparks in the base chambers. For each line, all other chambers were searched for the best possible sparks which had a χ^2 less than 8 for belonging on the line. The normalization used in calculating the χ^2 assumed that the basic chamber resolution was .5 mm, and that an additional error resulted from extrapolating (or interpolating) from the base chambers to the chamber being searched. If at least 3 sparks were found and the total χ^2 did not exceed 6 plus 2.5 times the number of non-base sparks, the line was accepted and a least squares fit to all sparks was made.

The routine PRUNES then searched for pairs of segments which shared two or more common sparks. As each such pair of segments was located, the track with fewer sparks or the larger χ^2 (if both tracks contained equal numbers of sparks) was deleted and the search was resumed over the remaining tracks.

4. Matching of X and Y Projections

The x and y projections of tracks were matched ("u-v mated") by routine UVMATE by searching for matching sparks in the rotated u-v spark chambers. The routine utilized one u-v CD chamber pair in the first upstream module, one u-v CD pair plus two 5' by 10' CIT chambers in one 10' by 10' plane in the second upstream module, and two CIT chambers in one plane in the spark chamber cart downstream of the toroids.

The actual matching proceeded by an exhaustive search technique.

Each combination of an x and y segment provided a unique projection into any u or v chamber. In each chamber the best possible spark with a χ^2 less than 8 was found, with a match being made as soon as one such spark was located. For a given x projection, the mate was made to the best possible y segment, where best was defined by lowest χ^2 with a χ^2 allowance of 2.5 per spark for matches with differing numbers of u-v sparks; i.e. the "best" match was strongly biased towards maximum number of u-v sparks rather than lowest χ^2 per spark.

The routine RAISIN then searched for multiple x projections matched to the same y projection, and removed all but the best x line match. The same criterion as used in UVMATE for best mate was utilized.

5. Matching of First and Second Upstream Modules

The routine FRMATE performed the matching of u-v mated tracks in both modules of the upstream spark chambers. This routine was utilized twice per event: once with relatively tight windows immediately after completion of u-v matching, and a second time with looser windows after corrections for various inefficiencies (see section 6) had been made.

Matching was achieved by searching for the best possible u-v mated line in the first module for each line in the second module. A χ^2 was calculated for each combination with four degrees of freedom corresponding to the x and y projections of angular and spatial multiple scattering in the second calorimeter/muon identifier. The minimum mating requirement was a χ^2 less than 16 in each of the x and y projections, and less than 25 for the sum of x and y. The best mate was defined by con-

sideration only of the sum of x and y contributions. The χ^2 was calculated assuming an average muon momentum of 10 GeV for the first attempt at matching, and 3 GeV for the second attempt.

6. Inefficiency Compensations

Inefficiencies due to spark chamber misses were partially corrected by routine EXTRA. These corrections were made immediately following the first pass through FRMATE.

Initially, all u-v mated segments in the second module which remained unmated to a segment in the first module were used as input. For each segment a search was made first for x and y segments in the first module, with mating requirements similar to those used in FRMATE: χ^2 less than 13 (for two degrees of freedom) for 10 GeV particles. This procedure corrected for inefficiency in the u-v chambers in the first module, and also allowed the projections of two tracks in the first module to be degenerate in x or y or both.

Next a search was made for tracks in the second module which matched segments in the first module in either x or y but not both. A road was made in the remaining projection and the best sparks in this road were then fit to a line segment. Two or more sparks forming a good line which mated properly through the second calorimeter/muon identifier were required to retain the track. Thus even if two chambers in one projection did not fire, a track was still likely to be found. The search for two good sparks within the road was flexible, and was capable of rejecting both sparks farthest from the center of the road and sparks farthest from the fitted lines within the road, and

could additionally mask out sparks used on complete lines already found by FRMATE.

Finally, EXTRA repeated this entire procedure using u-v mated segments in the first module as input and searching the second module for x and y segments and x or y segments with two or more sparks in the remaining view. In addition to correcting for chambers not firing, this procedure found tracks of muons whose trajectories diverged sufficiently that they only passed through two chambers in one projection in the second module.

After completion of these efficiency corrections all remaining u-v mated lines in both modules which had χ^2 greater than 5 for u-v sparks or greater than 5 per degree of freedom for x or y sparks were discarded by routine WEEDS. The remaining lines were used as input to the second pass through FRMATE with 3 GeV multiple scattering windows (see section 5).

The final compensation, performed by routine WANGLE, searched for tracks which were at such large polar angles that they missed most or all of the second CD chamber module and only struck the first CIT chambers upstream of the first half toroid. The u-v matched tracks in the first module which remained unmatched to tracks in the second module were searched for trajectories which extrapolated outside a one meter square at the longitudinal position of the last CD chamber in the second module. Roads into the second module were then made from these trajectories, and if one x and one y spark or one u-v spark pair was found in the road, the track was retained. Because these wide angle tracks often resulted from low energy muons, the roads made were quite large, corre-

sponding to a χ^2 less than 8 for multiple scattering of 1 GeV particles.

7. Straight Line Search Downstream of Magnet

The search for lines in the spark chamber cart downstream of the magnet proceeded in a fashion similar to the upstream search. The 4 x-y planes consisting of six 5' by 10' chambers and one 10' by 10' chamber were searched for x and y projections by LINE (see section 3). The resultant segments were u-v mated using one 10' by 10' plane consisting of two chambers. However, there was a 6" by 10' dead region in this u-v plane where the two chambers were butted together, and thus a substantial number of tracks intercepted no u-v chamber.

The solution employed to compensate for this dead region, implemented in routine CRTMAT, was to require a correlation between x and y chambers. Any pair of x and y segments for which at least 6 of the 7 x-y chambers showed either a hit in both x and y projections or a miss in both was mated regardless of the u-v chambers.

8. Toroid Track Finding

The toroid track finding, performed by routine ANGY, utilized the fact that the toroid magnet field was approximately cylindrically symmetric, and that therefore angular momentum along the toroid axis was conserved. The actual search utilized the conservation of the z component of $\vec{L} = \vec{r} \times \frac{\Delta\vec{r}}{\Delta z} \simeq \vec{r}_{old} \times \frac{\vec{r}_{new} - \vec{r}_{old}}{\Delta z} = \frac{\vec{r}_{old} \times \vec{r}_{new}}{\Delta z}$ in a ray tracing search. Given two points on an initial line, one could define both $\vec{r}_{old}$ and L_z and then proceed with a search for additional sparks in the toroid chambers. The initial lines used were just the straight lines found in both the upstream spark chambers and the spark chamber

cart downstream of the magnet.

Because opposite sign muon pairs tended to enter the magnet close together and separate as they progressed through the spectrometer, often with only the positive (focusing) trajectory remaining within the apparatus by the downstream end, it was more reasonable to start the track finding using downstream (cart) lines as input first and ray tracing these upstream through the magnet. Once these tracks were found and matched to lines in the upstream chamber modules, their sparks could be flagged as used and the search could then be continued using the remaining upstream lines as input and ray tracing downstream neglecting the already used sparks.

The ray tracing consisted of searching each successive 10' by 10' plane of chambers for the combination of an x spark and y spark within the same chamber which had L_z closest to the nominal value derived from the input line. The search windows used corresponded to a χ^2 less than 9 for errors dominated by multiple scattering of a 7 GeV particle traversing the spectrometer at a mean radius of .5 meters. The sparks were checked for self-consistency by requiring that the radius of curvature of projections of the track into both the x-z and y-z planes be greater than 14 meters for any two consecutive combinations of three adjacent sparks. After every three new sparks were added to the track, the nominal values of L_z and $\vec{r}_{old}$ were recalculated using the new sparks. In the case that no spark could be found in a given plane, a second search was made for sparks whose azimuthal angle lay within .3 radians of the already existing portion of the track.

Tracks which were ray traced from downstream to upstream were

matched to upstream lines by routine MATCHR. The routine drew straight lines from the most upstream spark in the toroids to the next two sparks downstream and searched for a match consistent with multiple scattering errors of these lines to those in the upstream chamber modules. The match required a χ^2 less than 16 (for two degrees of freedom) in both x and y views and a total χ^2 (for four degrees of freedom) less than 25 for 3 GeV particles. If no such match could be found, the most upstream spark in the toroid track was deleted and a second, and possibly a third attempt at matching was made before discarding the toroid track.

Tracks whose first spark was upstream of the third half toroid and which contained at least three sparks if traced from downstream or one spark if traced from upstream were then momentum fitted (see section 9) in a procedure which could add and delete sparks. The final cuts made were a first spark upstream of the fourth half toroid, a minimum number of sparks, two if traced from upstream and three if from downstream, and a maximum χ^2 per degree of freedom for the momentum fit of 2 if traced from upstream and 3 if traced from downstream.

9. Momentum Fitting

Toroid track momenta were fit iteratively by routine FITTER using the assumption that the χ^2 for the fit was approximately quadratic in 1/p, where p is the particle's momentum. Thus after each iteration a new value for momentum was calculated via $\frac{1}{p_{new}} = \frac{1}{p_{old}} - \alpha \frac{d\chi^2/dl/p}{d^2\chi^2/dl/p^2}$ with a typical value for the damping coefficient α of .5 rather than 1.0.

The initial value of p_{old} was calculated by routine MOM1 by finding the radius of curvature of a circle passing through three points on the track and assuming a constant average magnetic field of 10 kilogauss. The three points used were the place where the straight line in the upstream chambers intersected the front face of the first half toroid, the most downstream spark in the toroids for which no track could reasonably have entered the toroid central hole, and the spark halfway between these two points.

The fitting procedure consisted of up to ten iterations, but could be terminated as early as the fifth iteration if such produced no new sparks and a change of less than .1 in the total χ^2 per degree of freedom. In the first iteration all sparks found by ANGY were used. The second attempt used only those ANGY sparks with χ^2 less than 14 in both x and y projections. The third iteration threw out all existing sparks and instead searched each plane for that spark with χ^2 less than 14 which was closest to the projection of a track with the latest calculated momentum into that plane. If fewer than two sparks were found, the χ^2 window was repeatedly increased by a factor of 2 until either two sparks were found or a search for sparks of χ^2 less than 56 failed.

If the third iteration was successful, subsequent attempts searched each plane, using an existing spark if it lay within a χ^2 window, and otherwise searching for the best new spark within the window. The basic window used was a χ^2 of 14, but if the previous iteration had a χ^2 per degree of freedom less than 3, the window was reduced to 10, and if the previous iteration had a χ^2 per degree of freedom less than 2 and five or fewer sparks, the window was further reduced to a χ^2 of 6.

The χ^2 was calculated assuming that the errors resulted from the sum of the multiple scattering in all the toroids upstream of a given chamber. Although the errors were calculated using the current momentum estimate to determine the probable magnitude of the multiple scattering, the derivatives of the χ^2 were calculated without including terms resulting from the momentum dependence of the windows. Thus occasionally the fit χ^2 per degree of freedom would slowly diverge through the later iterations, although typically not by more than .05 per degree of freedom per iteration.

The fitting procedure was tested using a variety of data sets generated via Monte Carlo (see chapter IV). The fitting typically terminated after five iterations with an average difference between fitted and Monte Carlo generated momentum of less than 1% and a resolution of 10%.